GPS BASED ALTITUDE CONTROL OF AN
UNMANNED AIR VEHICLE
USING DIGITAL TERRAIN ELEVATION DATA

A THESIS SUBMITTED TO
THE GRADUATE SCHOOL OF NATURAL AND APPLIED SCIENCES
OF
MIDDLE EAST TECHNICAL UNIVERSITY

BY

SELÇUK ATAÇ

IN PARTIAL FULFILLMENT OF THE REQUIREMENTS
FOR
THE DEGREE OF MASTER OF SCIENCE
IN
MECHANICAL ENGINEERING

JUNE 2006

Approval of the Graduate School of Natural and Applied Sciences

<div style="text-align:right">

_____
Prof. Dr. Canan ÖZGEN
Director

</div>

I certify that this thesis satisfies all the requirements as a thesis for the degree of Master of Science.

<div style="text-align:right">

_____
Prof. Dr. S. Kemal İDER
Head of Department

</div>

This is to certify that we have read this thesis and that in our opinion it is fully adequate, in scope and quality, as a thesis for the degree of Master of Science.

_____   _____
Prof. Dr. Tuna BALKAN   Prof. Dr. Bülent E. PLATİN
Co-Supervisor   Supervisor

Examining Committee Members

Prof. Dr. M. Kemal ÖZGÖREN   (METU,ME)   _____

Prof. Dr. Bülent E. PLATİN   (METU,ME)   _____

Prof. Dr. Tuna BALKAN   (METU,ME)   _____

Asst. Prof. Dr. A. Buğra KOKU   (METU,ME)   _____

Dr. Gökmen MAHMUTYAZICIOĞLU   (TÜBİTAK-SAGE)   _____

I hereby declare that all information in this document has been obtained and presented in accordance with academic rules and ethical conduct. I also declare that, as required by these rules and conduct, I have fully cited and referenced all material and results that are not original to this work.

Name, Last name : Selçuk ATAÇ

Signature :

ABSTRACT

GPS BASED ALTITUDE CONTROL OF AN
UNMANNED AIR VEHICLE
USING DIGITAL TERRAIN ELEVATION DATA

Ataç, Selçuk

M.S., Department of Mechanical Engineering

Supervisor   : Prof. Dr. Bülent E. Platin

Co-Supervisor: Prof. Dr. Tuna Balkan

June 2006, 160 pages

In this thesis, an unmanned air vehicle (UAV) is used to develop a prototype base test platform for flight testing of new control algorithms and avionics for advanced UAV system development applications. A control system that holds the UAV at a fixed altitude above the ground is designed and flight tested. Only the longitudinal motion of the UAV is considered during the controller design, hence its lateral motions are controlled manually by a remote control unit from the ground. UAV's altitude with respect to the mean sea level and position are obtained by an onboard global positioning system (GPS) and this information is transmitted to the ground computer via radio frequency (RF) communication modules. The altitude of the UAV above the ground is calculated by using the digital terrain elevation data (DTED). A controller is designed and its gains are tuned to maintain this flight altitude at a desired value by using the mathematical model developed to represent the longitudinal dynamics of the UAV. Input signals generated by the controller for elevator deflections are transmitted back to the UAV via RF communication modules to drive onboard servomotors to generate desired elevator deflections. All controller computations and RF communications are handled by a MATLAB®

based platform on a ground computer. UAV flight tests are carried out at two different autopilot modes; namely, mean sea level (MSL) altitude hold mode and above ground level (AGL) altitude hold mode. The developed platform worked properly during flight tests and proved to be reliable in almost every condition. Moreover, the designed controller system is demonstrated to be effective and it fulfills the requirements.

Keywords: Unmanned air vehicle, altitude control, equations of motion, PID controller design, digital terrain elevation data

ÖZ

SAYISAL ARAZİ YÜKSEKLİK VERİSİ KULLANILARAK
BİR İNSANSIZ HAVA ARACININ
KKS TABANLI YÜKSEKLİK KONTROLÜ

Ataç, Selçuk

Yüksek Lisans, Makina Mühendisliği Bölümü

Tez Yöneticisi   : Prof. Dr. Bülent E. Platin

Ortak Tez Yöneticisi: Prof. Dr. Tuna Balkan

Haziran 2006, 160 sayfa

Bu tez çalışmasında, ileri düzey insansız hava aracı (İHA) geliştirme çalışmalarında kullanılacak yeni kontrol algoritmaları ve aviyonik sistemlerinin uçuş testlerinde prototip test platformu geliştirmek üzere bir İHA kullanılmıştır. İHA'yı yere göre sabit yükseklikte tutan bir kontrol algoritması tasarlanmış ve uçuş testleri yapılmıştır. Kontrolcü tasarımında İHA'nın sadece boylamasına hareketi dikkate alınmış, bu nedenle aracın yanlamasına hareketleri uzaktan kumanda ünitesi tarafından yerden elle kontrol edilmiştir. İHA'nın ortalama deniz seviyesine göre yüksekliği ve konumu üstüne takılı küresel konumla sistemi (KKS) tarafından elde edilmiş, ve bu bilgi yer bilgisayarına radyo frekanslı (RF) haberleşme üniteleri aracılığıyla iletilmiştir. İHA'nın yerden yüksekliği sayısal arazi yükseklik verisi kullanılarak hesaplanmıştır. İHA'nın boylamasına hareket dinamiğini temsil etmek üzere geliştirilen matematiksel model kullanılarak, uçuş yüksekliğini istenen bir değerde tutmak üzere bir kontrolcü tasarlanmış ve kazanç ayarları yapılmıştır. Yatay kontrol yüzeyi hareketleri için kontrolcü tarafından üretilen girdi sinyalleri, aracın üstüne takılı servo motorları çalıştırarak istenilen yatay kontrol yüzeyi hareketini oluşturmak üzere RF haberleşme üniteleri

aracılığıyla İHA'ya iletilmektedir. Tüm kontrolcü hesaplamaları ve RF haberleşmeleri yer bilgisayarındaki MATLAB® tabanlı bir platformda yürütülmektedir. İHA uçuş testleri ortalama deniz seviyesine göre yükseklik ve yere göre yükseklik tutma olmak üzere iki farklı otopilot kipinde gerçekleştirilmiştir. Geliştirilen platform testler sırasında düzgün bir şekilde çalışmış ve hemen her koşulda güvenilir olduğu ispatlanmıştır. Ayrıca, tasarlanan kontrolcünün etkin olduğu ve gereksinimleri yerine getirdiği görülmüştür.

Anahtar Kelimeler: İnsansız hava aracı, yükseklik kontrolü, hareket denklemleri, PID kontrolcü tasarımı, sayısal arazi yükseklik verisi

To my parents and my wife for their endless love, patience and support

ACKNOWLEDGMENTS

TABLE OF CONTENTS

LIST OF TABLES

LIST OF FIGURES

FIGURES

LIST OF SYMBOLS

A	Aspect ratio
b	Wing span
$\overline{c}$	Mean geometric chord
$\hat{C}^{(a,b)}$	Orthonormal transformation matrix from coordinate system b to a
C_D	Airplane drag coefficient
$C_{D,\alpha}$	Variation of airplane drag coefficient with angle of attack
$C_{D,\dot{\alpha}}$	Variation of airplane drag coefficient with dimensionless rate of change of angle of attack
$C_{D,q}$	Variation of airplane drag coefficient with dimensionless pitch rate
$C_{D,u}$	Variation of airplane drag coefficient with dimensionless speed
C_{D,δ_e}	Variation of airplane drag coefficient with elevator deflection angle
C_L	Airplane lift coefficient
$C_{L,\alpha}$	Variation of airplane lift coefficient with angle of attack
$C_{L,\dot{\alpha}}$	Variation of airplane lift coefficient with dimensionless rate of change of angle of attack
$C_{L,q}$	Variation of airplane drag coefficient with dimensionless pitch rate
$C_{L,u}$	Variation of airplane lift coefficient with dimensionless speed
C_{L,δ_e}	Variation of airplane lift coefficient with elevator deflection angle
C_m	Pitching moment coefficient
$C_{m,\alpha}$	Variation of airplane pitching moment coefficient with angle of attack
$C_{m,\dot{\alpha}}$	Variation of airplane pitching moment coefficient with dimensionless rate of change of angle of attack
$C_{m,T}$	Pitching moment coefficient due to thrust
C_{m,T_α}	Variation of airplane pitching moment coefficient due to thrust with

	angle of attack
C_{m,T_u}	Variation of airplane pitching moment coefficient due to thrust with dimensionless speed
$C_{m,q}$	Variation of airplane pitching moment coefficient with dimensionless pitch rate
$C_{m,u}$	Variation of airplane pitching moment coefficient with dimensionless speed
C_{m,δ_e}	Variation of airplane pitching moment coefficient with elevator deflection angle
C_x , C_z	Aerodynamic force coefficient components along x- and z-axes
$C_{T,x} , C_{T,z}$	Thrust force coefficient components along x- and z-axes
$C_{T,x_\alpha} , C_{T,z_\alpha}$	Variation of airplane thrust coefficient along x- and z-axes with angle of attack
C_{T,x_u} , C_{T,z_u}	Variation of airplane thrust coefficient along x- and z-axes with dimensionless speed $\vec{f}$
e	Oswald's efficiency factor
D	Denominator of longitudinal transfer functions
$\vec{F}$	Sum of all external forces acting on an airplane
F_x , F_y , F_z	Components of all external forces along x-, y-, and z-axes
F_A	Aerodynamic force
$F_{A,x} , F_{A,y} , F_{A,z}$	Aerodynamic force components along x-, y-, and z-axes
$f_{A,x} , f_{A,y} , f_{A,z}$	Perturbed values of $F_{A,x} , F_{A,y} , F_{A,z}$
F_T	Thrust force
$F_{T,x} , F_{T,y} , F_{T,z}$	Thrust force components along x-, y-, and z-axes
$f_{T,x} , f_{T,y} , f_{T,z}$	Perturbed values of $F_{T,x} , F_{T,y} , F_{T,z}$
g	Gravitational acceleration
h	Airplane altitude
H	Angular momentum
I_{xx} , I_{yy} , I_{zz}	Airplane mass moments of inertia about x-, y-, and z-axes

I_{xy} , I_{yz} , I_{xz}	Airplane mass products of inertia about x-, y-, and z-axes
L_A , M_A , N_A	Aerodynamic moment components about x-, y-, and z-axes
L_T , M_T , N_T	Thrust moment components about x-, y-, and z-axes
m	Airplane mass
m_A , m_T	Perturbed values of M_A and M_T
M	Mach number
$\vec{M}$	Sum of all external moments acting on an airplane
M_α	Pitch angular acceleration per unit angle of attack
$M_{\dot{\alpha}}$	Pitch angular acceleration per unit rate of change of angle of attack
$M_{T,\alpha}$	Pitch angular acceleration per unit of angle of attack due to thrust
$M_{T,u}$	Pitch angular acceleration per unit change in speed due to thrust
M_u	Pitch angular acceleration per unit change in speed
M_q	Pitch angular acceleration per unit pitch rate
M_{δ_e}	Pitch angular acceleration per unit elevator deflection
N_α	Numerator of angle of attack to elevator transfer function
N_θ	Numerator of pitch attitude to elevator transfer function
P, Q, R	Components of angular velocity about x-, y-, and z-axes
p, q, r	Perturbed values of P, Q, R
$\bar{q}$	Dynamic pressure
$\vec{r}^{(i)}$	Column vector representation of vector $\vec{r}$ in coordinate system i
S	Wing area
U, V, W	Components of airplane velocity along x-, y-, and z-axes
u, v, w	Perturbed values of U, V, W
X, Y, Z	Axes of Earth-fixed coordinate system
x, y, z	Axes of body-fixed coordinate system
X_α	Forward acceleration per unit angle of attack
$X_{T,u}$	Forward acceleration per unit change in speed due to thrust

X_u	Forward acceleration per unit change in speed
X_{δ_e}	Forward acceleration per unit elevator deflection
V	Airplane velocity (true airspeed)
Z_α	Vertical acceleration per unit angle of attack
$Z_{\dot{\alpha}}$	Vertical acceleration per unit rate of change of angle of attack
Z_u	Vertical acceleration per unit change in speed
Z_q	Vertical acceleration per unit pitch rate
Z_{δ_e}	Vertical acceleration per unit elevator deflection

Greek Letters

α	Angle of attack
γ	Flight path angle
λ	Longitude
Ψ	Yaw angle
ψ	Perturbed value of Ψ
Θ	Pitch angle
θ	Perturbed value of Θ
Φ	Roll angle
φ	Perturbed value of Φ
ω	Angular velocity of the airplane in the body-fixed coordinate system
δ_e	Elevator deflection angle
ρ	Density
$\Im_i$	Coordinate system i

Subscripts

1	Steady state quantity
m	Measured

cal   Calculated

Acronyms

A/D   Analog to Digital

AGL   Above Ground Level

CEP   Circular Error Probability

C.M.   Center of Mass

DAC   Digital Analog Converter

DGPS   Differential Global Positioning System

DOF   Degree of Freedom

DOP   Dilution of Precision

DTED   Digital Terrain Elevation Data

GPS   Global Positioning System

HDOP   Horizontal Dilution of Precision

IMU   Inertial Measurement Unit

INS   Inertial Navigation System

LTI   Linear Time-Invariant

METU   Middle East Technical University

MSL   Mean Sea Level

NIMA   National Imagery and Mapping Agency

NMEA   National Marine Electronics Association

PDOP   Position Dilution of Precision

PID   Proportional-Integral-Derivative

RC   Radio Controlled

RF   Radio Frequency

SEP   Spherical Error Probability

UART   Universal Asynchronous Receiver/Transmitter

UAV   Unmanned Air Vehicle

UTC   Universal Time Coordinated

VDOP   Vertical Dilution of Precision

CHAPTER 1

INTRODUCTION

1.1 INTRODUCTION

Since early 1900's, unmanned air vehicles (UAV) have been part of the aeronautical applications. However, the level of interest expressed by the aeronautical community and the recent researches over the past decade indicates that we are on the verge of a revolution in aeronautics. The underlying reason of this revolution is the dramatic advances in electronics, microprocessors, sensors, and communication modules which improve flight safety and performance of UAVs.

The interest and research in UAV applications have increased dramatically in recent years. UAVs are used by both military and civil organizations in a wide range of applications and have many advantages over those aerial vehicles that are manned. UAVs have low operational costs and they are more versatile and efficient when compared with manned aerial vehicles. But the most important of all is the elimination of the risk to loose a human life. Hence by mid 2005, nearly half of the nations of the world have some type of UAV in their arsenals [1].

UAVs have demonstrated their potential and capabilities in both military and civil applications such as aerial reconnaissance, surveillance, border and coast patrol, fire scouting, 3D mapping, power line inspection, and combat. Since these vehicles are not manned, costs related to man-machine interfaces and redundant electronic systems are greatly reduced.

As it is the first successful unmanned aircraft surveillance program, Predator is given in Figure 1 [2]. It is configured with a satellite data link system and has an endurance of 40 hours [2]. In addition to its surveillance capabilities, it is configured with air to air or air to ground weapons. Predator has logged over 65,000 flight hours since 1995, and it has demonstrated the technical viability and operational utility of UAVs worldwide.

Figure 1. Unmanned air vehicle, Predator [2]

In recent years, with the availability of high performance and low cost compact navigation avionics, research centers and universities have begun to investigate the feasibility of small UAVs to test compact avionics and guidance, navigation, and control algorithms. Small UAVs are typically low cost, light mass (<25 kg), and low speed (<150 km/h) air vehicles which are used for information gathering. These air vehicles can operate unnoticed at very low altitudes. By implementing an appropriate gimbal camera system, they can also be used for creating aerial image maps and delivering live video information of desired areas.

1.2 LITERATURE SURVEY

At Pontifical Catholic University of Chile, a low cost altitude control system for a radio controlled (RC) model airplane was developed by Abusleme, Cipriano, and Guarini to apply automatic control theoretical knowledge in real examples [3].

Their system consisted of a RC airplane with speed and altitude sensors onboard, a communication module, and a ground control computer. By this hardware in the loop platform, some previously developed control algorithms were tested in a real system. A low cost RC airplane with inherent stability characteristics and high storage capacity was chosen for their study and it was equipped with an altitude sensor and a radio frequency (RF) communications module.

An altitude sensor was designed to measure the airplane's altitude from 0 to 70 m with high resolution. The airplane's altitude was determined by measuring the barometric pressure with a pressure sensor. The sensor data was sent to the ground computer using a standard RF transmitter. A ground computer, which works in MATLAB® Simulink® environment, processes the sensor data, generates the required control commands to control the airplane's longitudinal motion and this information was sent to the airplane using a standard RC transmitter. The lateral dynamics of the airplane were manually controlled using a standard joystick connected to the ground computer. The block diagram representation of the system is shown in Figure 2 [3].
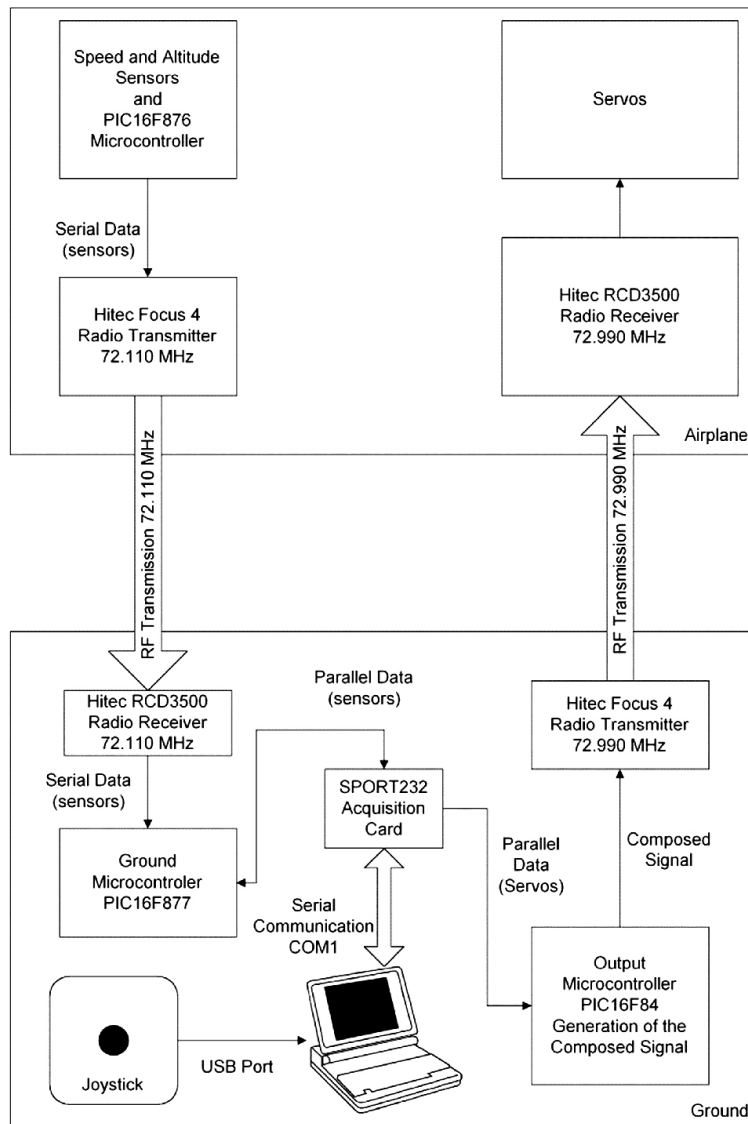
Figure 2. Platform developed in Pontifical Catholic University [3]

In their study, the airplane altitude was controlled by using proportional-integral-derivative (PID) controllers. The altitude control strategy had two PID controllers; altitude and climb rate controllers. The climb rate of the airplane was obtained by taking the derivative of the altitude measurements. The altitude controller accepts the altitude error as input and produces the estimated climb rate for the climb rate controller as output. The climb rate controller takes the difference between the

estimated and the actual climb rates, and generates the elevator deflection. During the simulations, the parameters of the PID controllers were calibrated by trial and error.

Flight tests showed that, this platform could be used as a base platform for teaching basic control systems. Altitude sensor, communication modules, and the controller worked well during the tests, but it was emphasized that using more sensors and improving the airplane mathematical model could increase the overall performance.

Another study was conducted in the Aeronautical and Astronautical Engineering Department of Naval Postgraduate School, USA. A rapid flight test prototyping system was developed for flight testing of guidance, navigation, and control algorithms for UAVs and parachutes [4]. The system enabled the testing the performance of theoretical prototypes in real mission scenarios.

Main system components, as shown in Figure 3 [4], were a UAV and a ground station. The UAV was equipped with an onboard computer that receives commands from the ground station sent over a serial modem and data from the onboard sensors. These sensors were an inertial measurement unit (IMU), a global positioning system (GPS), air data sensors, and control surface potentiometers. The ground station consisted of a computer, a serial modem, and a Futaba® remote control unit. Onboard computer commands can be overridden from ground by the remote control unit via the PWM switch.

The guidance, navigation, and control algorithms were developed in MATLAB® environment. The onboard computer executes the MATLAB® xPC target kernel that includes the control code to be flight tested. It was possible to send commands to the UAV and gather the data from the onboard sensors of the UAV via ground computer running in MATLAB® environment. A dynamic model of the UAV was developed using analytical methods and flight tested for validation purposes. The

control surface inputs and the corresponding airplane responses were measured by IMU sensors and used for parameter identification.
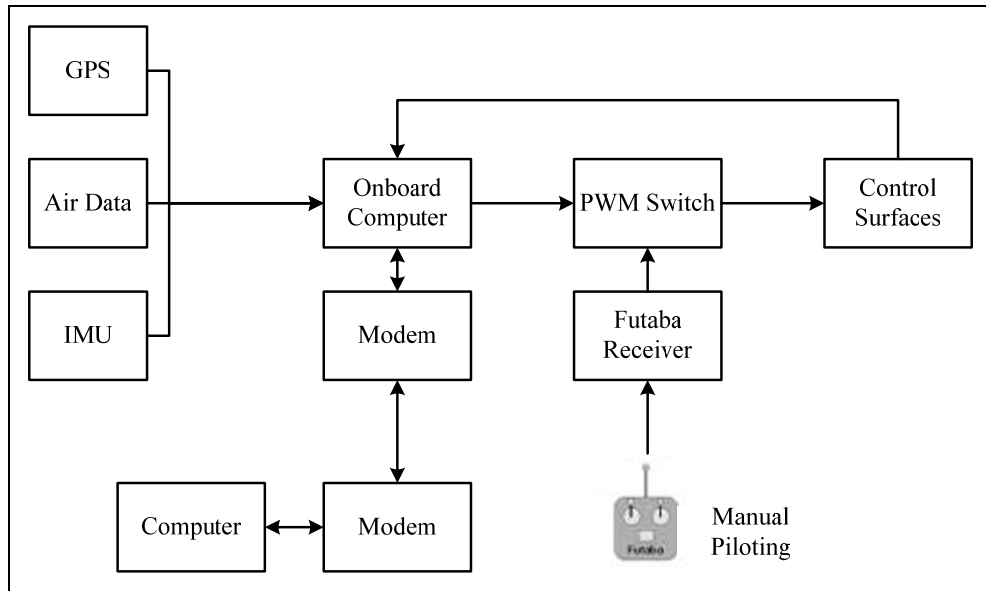
Figure 3. Setup developed at Naval Postgraduate School, USA [4]

Several algorithms such as trajectory tracking, voice control, and integrated infrared/inertial navigation were flight tested in the study. The results showed that the system was very effective, since it ensured safety and reliability in flight testing of the newly developed control algorithms for UAVs.

BAE Systems Controls developed an UAV autopilot system and used MATLAB® Simulink® widely in the modeling, design, analysis, code generation, and autopilot testing stages of the development [5]. The UAV was equipped with a vehicle management controller with a built-in IMU, RF data link receivers and transmitters, air data transducers, a GPS receiver, magnetometers, a power generator, and a battery. The speed, altitude, ground track control, and payload operation of the UAV could be controlled from the ground station. The UAV had

two operational flight modes; namely, remote control mode and autonomous control mode. In the autonomous control mode, the UAV could perform preprogrammed waypoint navigation, auto takeoff and landing, takeoff and landing abort, auto climbing and go-around. During the study, MATLAB® Simulink® was widely used to model the UAV system. The model included a six degrees of freedom (DOF) airplane nonlinear dynamic model, atmosphere model, turbulence model, control surface models, actuator models, sensor models, engine model, RF data link model, autopilot model, and it was stated that the cost and design cycle time had been reduced vastly by using MATLAB®.

In UAV systems, GPS and inertial navigation systems (INS) are mainly used as flight state sensors. Although INS is an independent navigation system with good dynamic characteristics and short term stability, it is expensive to obtain long term high accuracy and it is difficult to install and maintain. However, GPS is known with its simple usage and high accuracy with low cost. Therefore, to show that the automatic control of an UAV can be achieved using GPS only, a study was performed at Seoul National University in Korea [6]. Instead of using multiple antennas, a single antenna GPS receiver was used to lower the cost of the system which works as a sensor for guidance, navigation, and control purposes. To obtain the position more accurately, a real time differential GPS (DGPS) was also implemented to the system. The attitude (horizontal and vertical flight path angles and roll angle with respect to the airplane velocity vector axis) of the UAV was determined by an algorithm which processed the GPS position and velocity measurements using a simple point mass airplane model.

Flight tests showed that, by using only a single antenna GPS receiver, it was possible to control the UAV. However, due to the fact that GPS accuracy depends on the signal quality and number of the visible GPS satellites, this system could be considered as a backup control system for an UAV.

Another study on UAV navigation was conducted at North Carolina State University where a GPS auto navigation system was established [7]. An onboard computer system which was capable of real time control system implementation, data processing, and flight data storage was developed and implemented on the UAV. The system consisted of seven PC/104 computer cards one of which was a GPS receiver card. The angular rates of the UAV were measured by two angular rate transducers which were connected to the onboard computer system by analog to digital converters, whereas airspeed and altitude information were measured by a Pitot static probe mounted on the wing.

In that study, the UAV was flying by the waypoint navigation method where the waypoints were loaded to the onboard computer prior to flight. The position and heading of the UAV, which were measured by the GPS, were compared with the loaded waypoints and the necessary heading correction would be in the form of a coordinated level turn. The autopilot system included five PID controllers (for bank angle, pitch rate, yaw rate, velocity, and altitude hold) which are designed using MATLAB$^{®}$ and Simulink$^{®}$.

Up to the time they presented their paper [7], they had only flight tested the GPS system and the pitch rate autopilot. Test results showed that the system was reliable and the aircraft responses were similar to the simulation results.

1.3 MOTIVATION AND OBJECTIVE

All software and hardware developed for UAV applications need to be verified by flight tests. However, testing new algorithms, avionics, sensor packages, and air vehicles for small UAV applications requires a great effort from many branches of the engineering sciences which primarily include mechanical, aeronautical, electrical, and computer engineering. Since testing new ideas and systems provides

8

valuable information for development purposes as well as some insight on the systems, a need for a flying test platform arises.

Motivated by these considerations and as a contribution towards the development of a versatile setup for advanced UAV system designs and full autonomous control applications, developing a flying test platform resembling a small UAV is intended in this thesis study. Moreover, to test control algorithms on this UAV prototype, designing an altitude hold autopilot is also intended in this study.

The objective of the thesis is threefold. The first objective is to develop an experimental flying platform equipped with attitude sensors and data communication modules. For this purpose, an inherently stable RC airplane with a large storage capacity is selected and equipped with a GPS receiver and RF communication modules. An onboard GPS receiver is used to determine the position (longitude λ, latitude φ, and ellipsoidal height h as shown in Figure 4), speed, and heading of the airplane. RF communication modules are used for transmitting the GPS information to ground.
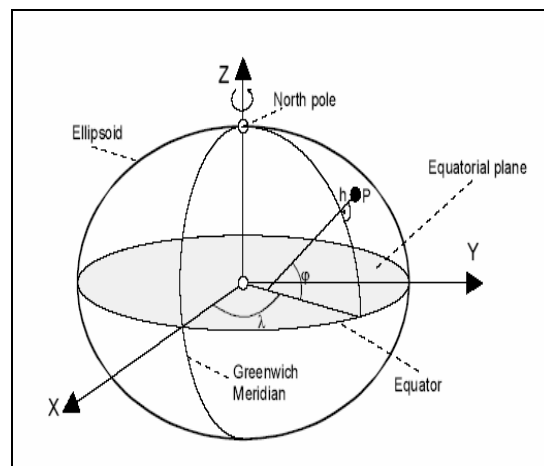
Figure 4. Position on Earth in ellipsoidal coordinates

The second objective is to obtain the dynamic model of the UAV prototype using analytical methods to represent the longitudinal dynamics of the UAV. Controller tuning during the initial flight tests can be skipped if the longitudinal dynamics are known accurately. Aerodynamic parameter estimation programs and mathematical relations are used to obtain the model.

The third and final objective is to develop and flight-test an autopilot for the UAV prototype. Among several autopilot modes, the altitude hold mode is selected for this purpose as new concepts can be introduced in this field. Other than its usage in UAVs, the altitude hold is an important pilot-relief mode and widely used in aviation. Generally, in altitude hold mode, air vehicle is held at a fixed altitude with respect to the mean sea level (MSL) during its flight.

However, in this thesis study, a new concept is introduced and air vehicle's flight at a fixed altitude with respect to the ground is desired using the digital terrain elevation data (DTED) of the underlying terrain. This concept is demonstrated in Figure 5. DTED is a uniform matrix of terrain elevation values which is developed by the United States National Imagery and Mapping Agency (NIMA) for military applications. In this study, DTED Level 2 is used to increase the terrain elevation accuracy. Detailed information about DTED is given in Appendix A.
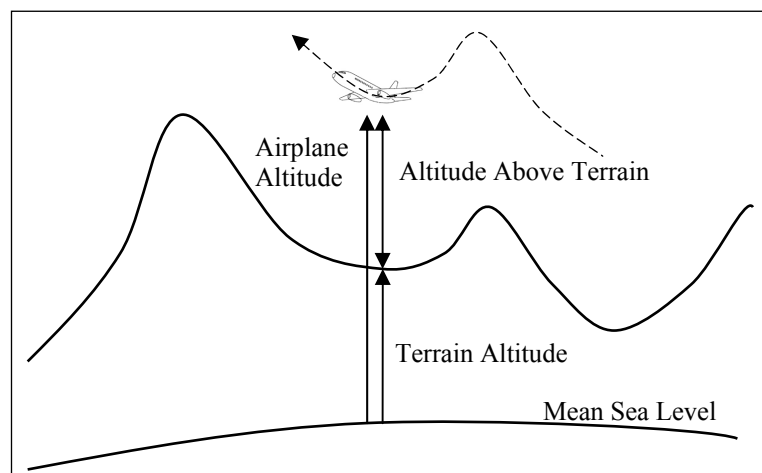
Figure 5. Graphical definitions of the altitudes

An autopilot is needed to provide the necessary control commands by which the UAV prototype will fly over the terrain at a constant height, which means that its above ground level (AGL) altitude remains unchanged. The control surface used to change the altitude of an air vehicle is the elevator whose position generates the necessary pitching moment acting on the vehicle. Hence, in order to stay within the desired AGL altitude limits, the controller is to generate the required elevator deflection angle for the UAV. A typical elevator of a conventional airplane is shown in Figure 6. Throughout this thesis study, only the longitudinal motion of the UAV is considered; the lateral motion of the airplane will be controlled manually by a remote control unit during test flights, hence the lateral dynamics of the airplane are ignored.
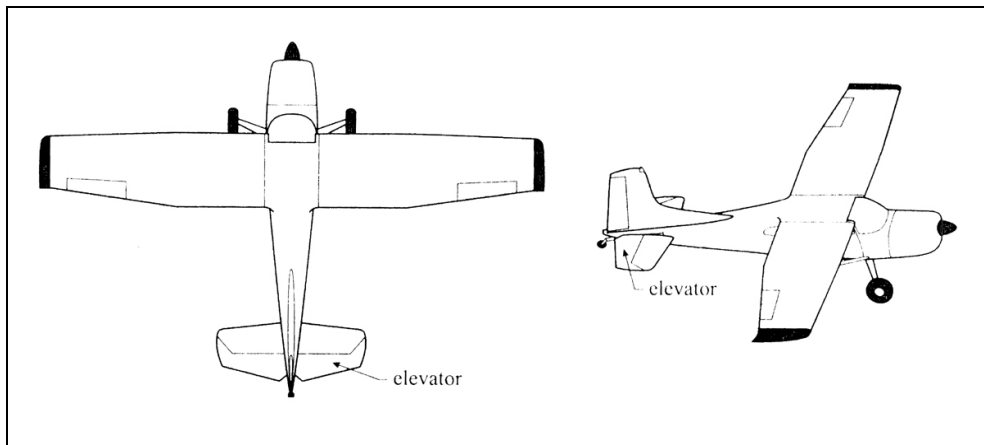
Figure 6. Elevator of a conventional airplane

1.4 OUTLINE OF THE THESIS

Chapter 1 gives an introduction and a brief objective of this thesis study. A literature survey on the subject matter is also presented.

In Chapter 2, the longitudinal equations of motion are given for the special case, perturbed state flight, and the longitudinal forces and moments in the longitudinal equations of motion for the perturbed state are obtained. The relation between altitude and elevator deflection of an airplane is also derived in the form of transfer function in this chapter.

In Chapter 3, the selection criteria and technical specifications of the RC model airplane used are given. An aerodynamic model of the airplane is also developed and presented in this chapter.

In Chapter 4, a PID controller for the altitude hold mode is designed in MATLAB$^{®}$ Simulink$^{®}$ environment using gain scheduling technique. Simulation results with the autopilot are also given.

In Chapter 5, the hardware used to develop the flying platform and ground station, their functions and features are presented.

In Chapter 6, the flight test results performed with the developed UAV and the designed autopilot are presented. The reliability of the received GPS data is investigated and some comments on the test results are given in this chapter.

In Chapter 7, a brief summary on the performed study is given. This chapter also contains some concluding remarks and recommendations for future works.

CHAPTER 2

MODELING

The motion of an airplane has six degrees of freedom if it is modeled as a rigid body. The mathematical model this motion can be expressed by kinematic and dynamic equations. The dynamic equations of motion can be established by applying the Newton's second law of motion to the airplane, whereas the kinematic equations of motion can be established from the trajectory of the motion. In this chapter, the general longitudinal equations of motion with the longitudinal (aerodynamic and thrust) forces and moments for a rigid airplane are derived. Using these equations of motion, a relationship between the airplane altitude and the elevator deflection is obtained as a transfer function. This transfer function is used in designing the controller in coming chapters.

2.1 EQUATIONS OF MOTION

The equations of motion of an airplane are a consequence of conservation laws in the three-dimensional space for linear and angular momentums, and are derived by applying Newton's second law of motion to that airplane. In this section, the general equations of motion for a rigid airplane are derived, and the coordinate systems used in the derivation of these equations are explained. From the complete set of equations of motion, the longitudinal equations of motion are separated and used throughout the study.

2.1.1 REFERENCE COORDINATE SYSTEMS

The two coordinate systems used in airframe dynamics are the Earth-fixed coordinate system and the body-fixed coordinate system, which are shown in Figure 7 [8].
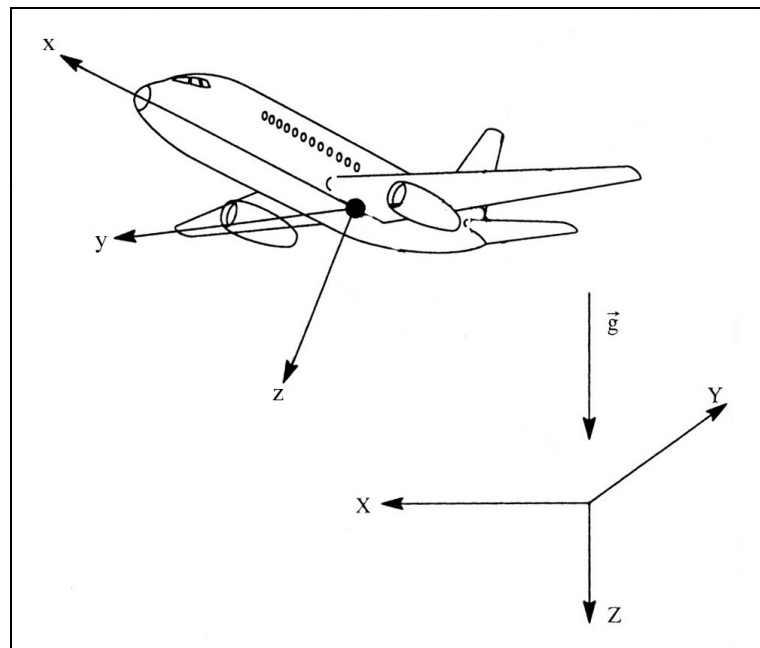
Figure 7. Earth-fixed and body-fixed coordinate systems [8]

The body-fixed coordinate system (x, y, z) has the origin located at the center of mass (c.m.) of the airplane. The coordinate system is fixed to the airplane and moves (that is translates and rotates) with it in a 3D space. The x-axis points forward along the fuselage, the y-axis points in the direction of the right wing and the z-axis points the bottom of the plane.

In the Earth-fixed coordinate system (X, Y, Z), the X-Y plane is normal to the local gravitational vector with the X-axis pointing north, the Y-axis pointing east,

and the Z-axis pointing down [9]. In this thesis study, the airplane is assumed to fly short ranges, so the Earth is assumed to be flat and the effect of its rotational velocity is neglected. By these assumptions, the Earth-fixed coordinate system is regarded as an inertial coordinate system.

Deriving the equations of motion of an airplane, there is a need for representing angular velocity and gravitational force terms in the body-fixed coordinate system. A vector $\vec{r}$ can be transformed from one coordinate system $\Im_b$ to another $\Im_a$ by using transformation matrices. This transformation can be expressed as follows [10], [11], [12].

$$\bar{r}^{(a)} = \hat{C}^{(a,b)} \bar{r}^{(b)} \tag{2.1}$$

where $\hat{C}^{(a,b)}$ is the transformation matrix from the coordinate system $\Im_b$ to the coordinate system $\Im_a$; $\bar{r}^{(a)}$, and $\bar{r}^{(b)}$ are the column vector representations of $\vec{r}$ in respective coordinate systems.

Consider a rectilinear coordinate system with unit vectors $\vec{i}, \vec{j},$ and $\vec{k}$, and let $\vec{r} = x\vec{i} + y\vec{j} + z\vec{k}$ be an arbitrary vector in this coordinate system. Then, the column vector representation of vector $\vec{r}$ will be $\bar{r} = \begin{bmatrix} x & y & z \end{bmatrix}^T$.

The elements of the transformation matrix $\hat{C}^{(a,b)}$ can be found by the following equation [10], [11], [12].

$$C_{i,j}^{(a,b)} = \cos\theta_{i,j}^{(a,b)} \tag{2.2}$$

where $\cos\theta_{i,j}^{(a,b)}$ is the cosine of the angle between the i-axis of the coordinate system $\Im_a$, and the j-axis of the coordinate system $\Im_b$.

15

Using this definition; for the vector transformations from the Earth-fixed coordinate system $\Im_E$ to the body-fixed coordinate system $\Im_B$, the transformation matrix $\hat{C}^{(B,E)}$ should be constructed. This can be achieved by using Euler angles.

2.1.1.1 EULER ANGLES

Several Euler angle sequences could be used for rotational transformations from the inertial to body-fixed axes. In flight mechanics, the so-called 3-2-1 angle sequence is commonly used [13]. The 3-2-1 Euler angle transformation consists of the following three sequential rotations.

1) Starting with the Earth-fixed coordinate system rotate about the Z axis by an angle Ψ to define a second coordinate system (X_2, Y_2, Z_2).

2) Rotate about the Y_2 axis by an angle Θ to define a third coordinate system (X_3, Y_3, Z_3).

3) Finally, rotate about the X_3 axis by an angle Φ to define the body-fixed coordinate system (x, y, z)

$$\Im_E \xrightarrow{\Psi} \Im_2 \xrightarrow{\Theta} \Im_3 \xrightarrow{\Phi} \Im_B$$

where Ψ is called as the yaw angle, Θ as the pitch angle, and Φ as the roll angle. These three rotations are shown in Figure 8 [13].

16
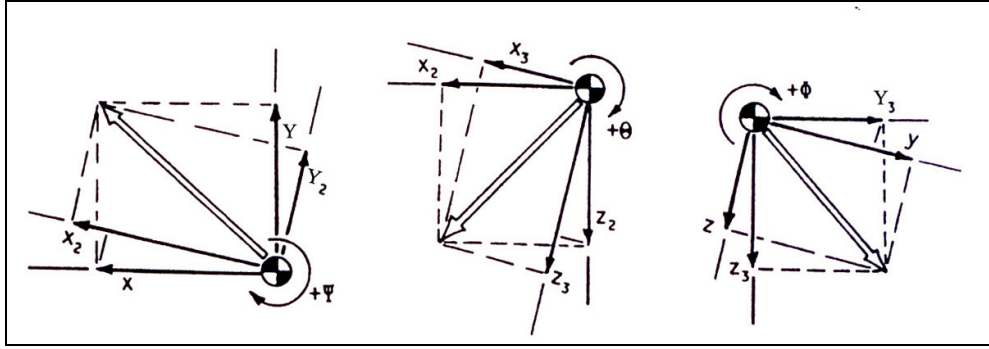
Figure 8. Euler angle transformations [13]

The corresponding transformation matrices become

$$\hat{C}^{(2,E)} = \begin{bmatrix} C_\Psi & S_\Psi & 0 \\ -S_\Psi & C_\Psi & 0 \\ 0 & 0 & 1 \end{bmatrix} \tag{2.3}$$

$$\hat{C}^{(3,2)} = \begin{bmatrix} C_\Theta & 0 & -S_\Theta \\ 0 & 1 & 0 \\ S_\Theta & 0 & C_\Theta \end{bmatrix} \tag{2.4}$$

$$\hat{C}^{(B,3)} = \begin{bmatrix} 1 & 0 & 0 \\ 0 & C_\Phi & S_\Phi \\ 0 & -S_\Phi & C_\Phi \end{bmatrix} \tag{2.5}$$

where C and S represent the cosine and sine of angles respectively.

The combined transformation matrix $\hat{C}^{(B,E)}$ is calculated by the multiplication of these three transformation matrices [10], [11], [12].

$$\hat{C}^{(B,E)} = \hat{C}^{(B,3)}\hat{C}^{(3,2)}\hat{C}^{(2,E)} \tag{2.6}$$

17

Performing the matrix multiplications, the transformation matrix from the Earth-fixed coordinate system to the body-fixed coordinate system is obtained as follows.

$$\hat{C}^{(B,E)} = \begin{bmatrix} C_\Psi C_\Theta & S_\Psi C_\Theta & -S_\Theta \\ C_\Psi S_\Theta S_\Phi - S_\Psi C_\Phi & S_\Psi S_\Theta S_\Phi + C_\Psi C_\Phi & C_\Theta S_\Phi \\ C_\Psi S_\Theta C_\Phi + S_\Psi S_\Phi & S_\Psi S_\Theta C_\Phi - C_\Psi S_\Phi & C_\Theta C_\Phi \end{bmatrix} \tag{2.7}$$

2.1.2 TRANSLATIONAL EQUATIONS OF MOTION

According to the Newton's second law of motion, the summation of all external forces $\vec{F}$ acting on a body must be equal to the time rate of change (taken with respect to inertial space) of its linear momentum $m\vec{V}$ [14].

$$\vec{F} = \frac{d}{dt}(m\vec{V}) \bigg]_E \tag{2.8}$$

In Equation (2.8), $\vec{V}$ is the velocity of the center of mass of the airplane and $\big]_E$ indicates that the differentiation of the vector is performed in the Earth-fixed coordinate system.

Assuming that the mass of the airplane remains constant, Equation (2.8) becomes

$$\vec{F} = m\frac{d}{dt}(\vec{V}) \bigg]_E \tag{2.9}$$

Equation (2.9) can be expressed in the body frame as

18

$$\vec{F} = m\left\{ \frac{d}{dt}\left(\vec{V}\right)\Big]_B + \vec{\omega} \times \vec{V} \right\} \tag{2.10}$$

where the angular velocity $\vec{\omega}$, and linear velocity $\vec{V}$ are expressed in the body-fixed coordinate system as

$$\vec{\omega} = P\vec{i} + Q\vec{j} + R\vec{k} \tag{2.11}$$

$$\vec{V} = U\vec{i} + V\vec{j} + W\vec{k} \tag{2.12}$$

where P = roll rate

Q = pitch rate

R = yaw rate

U = forward velocity

V = side velocity

W = downward velocity

and $\vec{i}$, $\vec{j}$, $\vec{k}$ are the unit vectors along the x, y, z axes of the body-fixed coordinate system of the airplane.

Substituting Equations (2.11) and (2.12) into Equation (2.10) we get

$$\vec{F} = m\left[\left(\dot{U} - VR + WQ\right)\vec{i} + \left(\dot{V} + UR - WP\right)\vec{j} + \left(\dot{W} - UQ + VP\right)\vec{k}\right] \tag{2.13}$$

An airplane is subjected to four basic forces during its flight; namely, weight, thrust, and aerodynamic (lift and drag) forces. Thus, $\vec{F}$ is the sum of aerodynamic, thrust, and gravitational forces in the body-fixed coordinate system. Hence, the left hand side of Equation (2.13) can also be expressed as follows.

$$\vec{F} = \vec{F}_A + \vec{F}_T + m\vec{g} \tag{2.14}$$

19

To represent the gravitational acceleration in the body-fixed coordinate system, Equations (2.1) and (2.7) are used.

$$\overline{g}^{(B)} = \hat{C}^{(B,E)} \overline{g}^{(E)} = \hat{C}^{(B,E)} \begin{bmatrix} 0 \\ 0 \\ g \end{bmatrix} = \begin{bmatrix} -g\sin\Theta \\ g\sin\Phi\cos\Theta \\ g\cos\Phi\cos\Theta \end{bmatrix} \tag{2.15}$$

Substituting the gravitational acceleration term into Equation (2.14), we get

$$\vec{F} = \left(F_{A,x} + F_{T,x} - mg\sin\Theta\right)\vec{i} + \left(F_{A,y} + F_{T,y} + mg\sin\Phi\cos\Theta\right)\vec{j} +$$
$$\left(F_{A,z} + F_{T,z} + mg\cos\Phi\cos\Theta\right)\vec{k} \tag{2.16}$$

Hence, combining Equations (2.13) and (2.16), the translational equations of motion are expressed as follows.

$$m\left(\dot{U} - VR + WQ\right) = F_{A,x} + F_{T,x} - mg\sin\Theta \tag{2.17}$$

$$m\left(\dot{V} + UR - WP\right) = F_{A,y} + F_{T,y} + mg\sin\Phi\cos\Theta \tag{2.18}$$

$$m\left(\dot{W} - UQ + VP\right) = F_{A,z} + F_{T,z} + mg\cos\Phi\cos\Theta \tag{2.19}$$

2.1.3 ROTATIONAL EQUATIONS OF MOTION

According to the Newton's second law of motion, summation of all external moments $\vec{M}$ acting on a body must be equal to the time rate of change (taken with respect to inertial space) of it's angular momentum $\vec{H}$, or moment of momentum [14].

$$\vec{M} = \frac{d\vec{H}}{dt}\bigg]_E \qquad (2.20)$$

The definition of the angular momentum is

$$\vec{H} = \int \vec{r} \times (\vec{\omega} \times \vec{r}) dm \qquad (2.21)$$

Substituting Equation (2.11) and $\vec{r} = x\vec{i} + y\vec{j} + z\vec{k}$ into Equation (2.21) we get

$$\vec{H} = \int \left[(y^2 + z^2)P - xyQ - xzR \right] dm\vec{i} + \int \left[(z^2 + x^2)Q - yzR - xyP \right] dm\vec{j} +$$
$$\int \left[(x^2 + y^2)R - xzP - yzQ \right] dm\vec{k} \qquad (2.22)$$

Defining

$$I_{xx} = \int (y^2 + z^2) dm \qquad I_{yy} = \int (z^2 + x^2) dm$$
$$I_{zz} = \int (x^2 + y^2) dm \qquad I_{xy} = \int xy dm \qquad (2.23)$$
$$I_{xz} = \int xz dm \qquad I_{yz} = \int yz dm$$

as respective mass moments and mass products of inertia and using the fact that most airplanes are symmetrical about the xz plane ($I_{xy} = I_{yz} = 0$), Equation (2.22) becomes

$$\vec{H} = (PI_{xx} - RI_{xz})\vec{i} + QI_{yy}\vec{j} + (RI_{zz} - PI_{xz})\vec{k} \qquad (2.24)$$

Equation (2.20) can be expressed in the body frame as

$$\vec{M} = \frac{d\vec{H}}{dt}\bigg]_B + \vec{\omega} \times \vec{H} \tag{2.25}$$

Substituting Equations (2.11) and (2.24) into Equation (2.25) we get

$$\vec{M} = \left(\dot{P}I_{xx} - \dot{R}I_{xz}\right)\vec{i} + \dot{Q}I_{yy}\vec{j} + \left(\dot{R}I_{zz} - \dot{P}I_{xz}\right)\vec{k} +$$
$$\left(P\vec{i} + Q\vec{j} + R\vec{k}\right) \times \left(PI_{xx} - RI_{xz}\right)\vec{i} + QI_{yy}\vec{j} + \left(RI_{zz} - PI_{xz}\right)\vec{k} \tag{2.26}$$

Expressing the moment $\vec{M}$ in terms of its components

$$\vec{M} = \left(L_A + L_T\right)\vec{i} + \left(M_A + M_T\right)\vec{j} + \left(N_A + N_T\right)\vec{k} \tag{2.27}$$

where L, M, and N are the components of $\vec{M}$ along the unit vectors $\vec{i}$, $\vec{j}$, $\vec{k}$ of the body-fixed coordinate system due to aerodynamic and thrust forces. Hence, combining Equations (2.26) and (2.27), the rotational equations of motion are expressed as follows.

$$I_{xx}\dot{P} - I_{xz}\dot{R} - I_{xz}PQ + \left(I_{zz} - I_{yy}\right)RQ = L_A + L_T \tag{2.28}$$

$$I_{yy}\dot{Q} + \left(I_{xx} - I_{zz}\right)PR + I_{xz}\left(P^2 - R^2\right) = M_A + M_T \tag{2.29}$$

$$I_{zz}\dot{R} - I_{xz}\dot{P} + \left(I_{yy} - I_{xx}\right)PQ + I_{xz}QR = N_A + N_T \tag{2.30}$$

2.1.4 KINEMATIC RELATIONSHIPS

Relations between the time rates of change of Euler angles with the angular rotation rates in the body frame can be obtained by the following procedure [13].

The column matrix representation $\overline{\omega}$ of angular velocity $\vec{\omega}$ is

$$\overline{\omega} = \begin{bmatrix} P \\ Q \\ R \end{bmatrix} \tag{2.31}$$

The angular velocity can also be described by components aligned with the Euler angle rates; $\dot{\Phi}, \dot{\Theta}$ and $\dot{\Psi}$ defined by $\vec{\omega}_\Phi, \vec{\omega}_\Theta$ and $\vec{\omega}_\Psi$ respectively.

$$\overline{\omega} = \overline{\omega}_\Phi + \overline{\omega}_\Theta + \overline{\omega}_\Psi \tag{2.32}$$

$\overline{\omega}_\Phi$ expressed in the body-fixed coordinate system is

$$\overline{\omega}_\Phi = \hat{C}{}^{(B,3)} \begin{bmatrix} \dot{\Phi} \\ 0 \\ 0 \end{bmatrix} \tag{2.33}$$

$\overline{\omega}_\Theta$ expressed in the body-fixed coordinate system is

$$\overline{\omega}_\Theta = \hat{C}{}^{(B,3)} \hat{C}{}^{(3,2)} \begin{bmatrix} 0 \\ \dot{\Theta} \\ 0 \end{bmatrix} \tag{2.34}$$

$\overline{\omega}_\Psi$ expressed in the body-fixed coordinate system is

$$\overline{\omega}_\Psi = \hat{C}{}^{(B,3)} \hat{C}{}^{(3,2)} \hat{C}{}^{(2,E)} \begin{bmatrix} 0 \\ 0 \\ \dot{\Psi} \end{bmatrix} \tag{2.35}$$

Combining these three matrix transformations yields a single matrix transformation relating the body-axis angular rates to the Euler angle rates.

$$
\begin{bmatrix} P \\ Q \\ R \end{bmatrix} = \begin{bmatrix} 1 & 0 & -S_{\Theta} \\ 0 & C_{\Phi} & C_{\Theta}S_{\Phi} \\ 0 & -S_{\Phi} & C_{\Theta}C_{\Phi} \end{bmatrix} \begin{bmatrix} \dot{\Phi} \\ \dot{\Theta} \\ \dot{\Psi} \end{bmatrix} \tag{2.36}
$$

Hence, the kinematic relationships are expressed as follows.

$$
P = \dot{\Phi} - \dot{\Psi} \sin \Theta \tag{2.37}
$$

$$
Q = \dot{\Theta} \cos \Phi + \dot{\Psi} \cos \Theta \sin \Phi \tag{2.38}
$$

$$
R = \dot{\Psi} \cos \Theta \cos \Phi - \dot{\Theta} \sin \Phi \tag{2.39}
$$

2.1.5 LONGITUDINAL EQUATIONS OF MOTION

Assuming small coupling between the longitudinal variables and the lateral directional variables, the six equations of motion, Equations (2.17) through (2.19) and Equations (2.28) through (2.30), can be broken up into two sets of three simultaneous equations.

In longitudinal motion, the airplane is considered to be in wings level, straight line, and unaccelerated flight [14]. The deflection of the elevator is the only disturbance, which causes a pitching moment and a change in both F_x and F_y. However, this deflection does not cause any rolling moment, any yawing moment, or any change in F_y. Thus, P=R=V=0 and Equations (2.18), (2.28), and (2.30) can be neglected. As a result, the longitudinal equations of motion become;

$$m(\dot{U} + WQ) = F_{A,x} + F_{T,x} - mg\sin\Theta \qquad\qquad (2.40)$$

$$m(\dot{W} - UQ) = F_{A,z} + F_{T,z} + mg\cos\Theta \qquad\qquad (2.41)$$

$$I_{yy}\dot{Q} = M_A + M_T \qquad\qquad (2.42)$$

$$\text{with } Q = \dot{\Theta} \qquad\qquad (2.43)$$

2.1.6 PERTURBED STATE LONGITUDINAL EQUATIONS OF MOTION

There are two special flight conditions in designing an airplane and building the equations. One is the steady state flight condition, and the other is the perturbed state flight condition [8].

In a steady state flight, all motion variables are constant with time in the body-fixed coordinate system (x, y, z), which means that the angular velocity $\vec{\omega}$, and linear velocity $\vec{V}$ of the airplane are constant in time.

In a perturbed state flight, all motion variables are defined relative to a known steady state flight condition. Any non-steady state flight condition can be considered as being perturbed from a steady state. Both flight conditions are shown in Figure 9 [8].
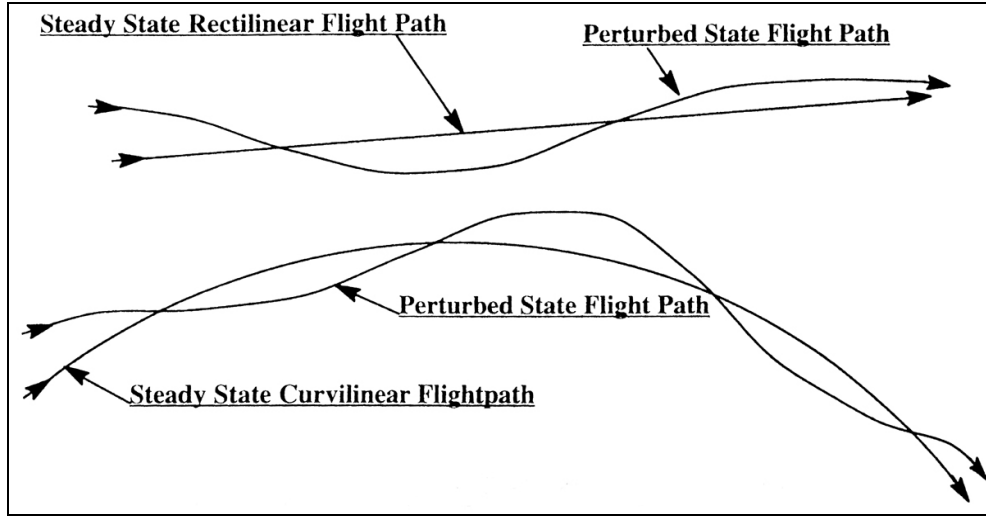
Figure 9. Steady state and perturbed state flight paths [8]

In a perturbed state flight; longitudinal motion variables, forces, and moments are expressed as follows.

$$U = U_1 + u \qquad W = W_1 + w \qquad Q = Q_1 + q$$

$$\Theta = \Theta_1 + \theta \qquad F_{A,x} = F_{A,x_1} + f_{A,x} \qquad F_{A,z} = F_{A,z_1} + f_{A,z} \qquad (2.44)$$

$$M_A = M_{A_1} + m_A \qquad M_T = M_{T_1} + m_T$$

where the subscript 1 indicates that it is the steady state value of the variable. This notation is widely used throughout the thesis.

Substituting these perturbed values into the longitudinal equations of motion in Equations (2.40) through (2.43), we get

$$m\left(\dot{u} + \left(W_1 + w\right)\left(Q_1 + q\right)\right) = F_{A,x_1} + f_{A,x} + F_{T,x_1} + f_{T,x} - mg\sin\left(\Theta_1 + \theta\right) \qquad (2.45)$$

$$m\left(\dot{w} - \left(U_1 + u\right)\left(Q_1 + q\right)\right) = F_{A,z_1} + f_{A,z} + F_{T,z_1} + f_{T,z} + mg\cos\left(\Theta_1 + \theta\right) \qquad (2.46)$$

26

$$I_{yy}\dot{q} = M_{A_1} + m_A + M_{T_1} + m_T \tag{2.47}$$

$$\text{with } Q_1 + q = \dot{\Theta}_1 + \dot{\theta} \tag{2.48}$$

By assuming small perturbances about the steady state condition, considering the steady state properties, and neglecting higher order terms, Equations (2.45) through (2.48) become

$$m(\dot{u} + W_1 q) = f_{A,x} + f_{T,x} - mg\theta\cos\Theta_1 \tag{2.49}$$

$$m(\dot{w} - U_1 q) = f_{A,z} + f_{T,z} - mg\theta\sin\Theta_1 \tag{2.50}$$

$$I_{yy}\dot{q} = m_A + m_T \tag{2.51}$$

$$\text{with } q = \dot{\theta} \tag{2.52}$$

Expressions given by the Equations (2.49) through (2.52) are the perturbed state longitudinal equations of motion of an airplane. Note that these equations are linear coupled ordinary differential equations in terms of four variables; namely, u, w, q, and θ.

2.2 PERTURBED STATE FORCES AND MOMENTS

The air that goes over an airplane's external surface generates friction, but moreover it creates multiple zones with pressure differences. These pressure differences produce force vectors on the solid body. These force vectors are considered as the aerodynamic forces. The moments of these forces with respect to a specific point, especially center of mass of the airplane, are called as the aerodynamic moments. Other force acting on a flying airplane is the thrust force

which also creates a moment on the airplane if its line of application does not pass through the center of mass of the airplane. In this Section, the longitudinal aerodynamic and thrust forces, and moments in the equations of motion for the perturbed state flight are obtained using Taylor series expansions of the forces and moments with respect to the perturbation variables.

2.2.1 PERTURBED STATE AERODYNAMIC FORCES AND MOMENTS

In the longitudinal dynamics, the perturbation variables used in expressing aerodynamic forces and moments are the axial velocity u, the angle of attack α, the damping terms $\dot{\alpha}$ and $q\,(=\dot{\theta})$, and the longitudinal control deflection δ_e.

Hence, the first order Taylor series expansions of the perturbed state longitudinal aerodynamic forces and moments are expressed as [8];

$$f_{A,x} = \frac{\partial F_{A,x}}{\partial u}u + \frac{\partial F_{A,x}}{\partial \alpha}\alpha + \frac{\partial F_{A,x}}{\partial \dot{\alpha}}\dot{\alpha} + \frac{\partial F_{A,x}}{\partial q}q + \frac{\partial F_{A,x}}{\partial \delta_e}\delta_e \qquad (2.53)$$

$$f_{A,z} = \frac{\partial F_{A,z}}{\partial u}u + \frac{\partial F_{A,z}}{\partial \alpha}\alpha + \frac{\partial F_{A,z}}{\partial \dot{\alpha}}\dot{\alpha} + \frac{\partial F_{A,z}}{\partial q}q + \frac{\partial F_{A,z}}{\partial \delta_e}\delta_e \qquad (2.54)$$

$$m_A = \frac{\partial M_A}{\partial u}u + \frac{\partial M_A}{\partial \alpha}\alpha + \frac{\partial M_A}{\partial \dot{\alpha}}\dot{\alpha} + \frac{\partial M_A}{\partial q}q + \frac{\partial M_A}{\partial \delta_e}\delta_e \qquad (2.55)$$

To express Equations (2.53) through (2.55) in dimensionless form, u is divided by U_1 (steady state velocity of the airplane in the x-axis of the body-fixed coordinate system), and the damping terms are multiplied by $\bar{c}/2U_1$, where $\bar{c}$ is the mean geometric chord of the wing. The resulting equations are;

$$f_{A,x} = \frac{\partial F_{A,x}}{\partial \left(\dfrac{u}{U_1}\right)} \frac{u}{U_1} + \frac{\partial F_{A,x}}{\partial \alpha} \alpha + \frac{\partial F_{A,x}}{\partial \left(\dfrac{\dot{\alpha}\bar{c}}{2U_1}\right)} \frac{\dot{\alpha}\bar{c}}{2U_1} + \frac{\partial F_{A,x}}{\partial \left(\dfrac{q\bar{c}}{2U_1}\right)} \frac{q\bar{c}}{2U_1} + \frac{\partial F_{A,x}}{\partial \delta_e} \delta_e \qquad (2.56)$$

$$f_{A,z} = \frac{\partial F_{A,z}}{\partial \left(\dfrac{u}{U_1}\right)} \frac{u}{U_1} + \frac{\partial F_{A,z}}{\partial \alpha} \alpha + \frac{\partial F_{A,z}}{\partial \left(\dfrac{\dot{\alpha}\bar{c}}{2U_1}\right)} \frac{\dot{\alpha}\bar{c}}{2U_1} + \frac{\partial F_{A,z}}{\partial \left(\dfrac{q\bar{c}}{2U_1}\right)} \frac{q\bar{c}}{2U_1} + \frac{\partial F_{A,z}}{\partial \delta_e} \delta_e \qquad (2.57)$$

$$m_A = \frac{\partial M_A}{\partial \left(\dfrac{u}{U_1}\right)} \frac{u}{U_1} + \frac{\partial M_A}{\partial \alpha} \alpha + \frac{\partial M_A}{\partial \left(\dfrac{\dot{\alpha}\bar{c}}{2U_1}\right)} \frac{\dot{\alpha}\bar{c}}{2U_1} + \frac{\partial M_A}{\partial \left(\dfrac{q\bar{c}}{2U_1}\right)} \frac{q\bar{c}}{2U_1} + \frac{\partial M_A}{\partial \delta_e} \delta_e \qquad (2.58)$$

Aerodynamic forces and moments defined in the stability axis system are expressed as

$$F_{A,x} = C_x \bar{q} S \qquad (2.59)$$

$$F_{A,z} = C_z \bar{q} S \qquad (2.60)$$

$$M_A = C_m \bar{q} S \bar{c} \qquad (2.61)$$

where C_m is the aerodynamic pitching moment coefficient of the airplane, C_x and C_z are the aerodynamic force coefficient components along the x and z axis of the stability axis system. The stability axis system is still a body-fixed coordinate system and the equations of motion derived in Section 2.1 are also valid for the stability axis system [8]. In addition to these aerodynamic coefficients, $\bar{q}$ is the dynamic pressure defined by Equation (3.12) and S is the wing area of the airplane.

The partial derivatives of the aerodynamic forces and moments in Equations (2.56) through (2.58) are derived in the following sections.

2.2.1.1 PARTIAL DIFFERENTIATION WITH RESPECT TO u/U₁

First, the partial differentiation of the aerodynamic force component $F_{A,x}$, expressed by Equation (2.59) is derived. Note that all partial differentiations and variables must be evaluated at the steady state conditions for which all perturbation variables are zero.

$$\frac{\partial F_{A,x}}{\partial\left(\dfrac{u}{U_1}\right)} = \frac{\partial C_x}{\partial\left(\dfrac{u}{U_1}\right)}\overline{q}S + C_x S \frac{\partial\overline{q}}{\partial\left(\dfrac{u}{U_1}\right)} \tag{2.62}$$
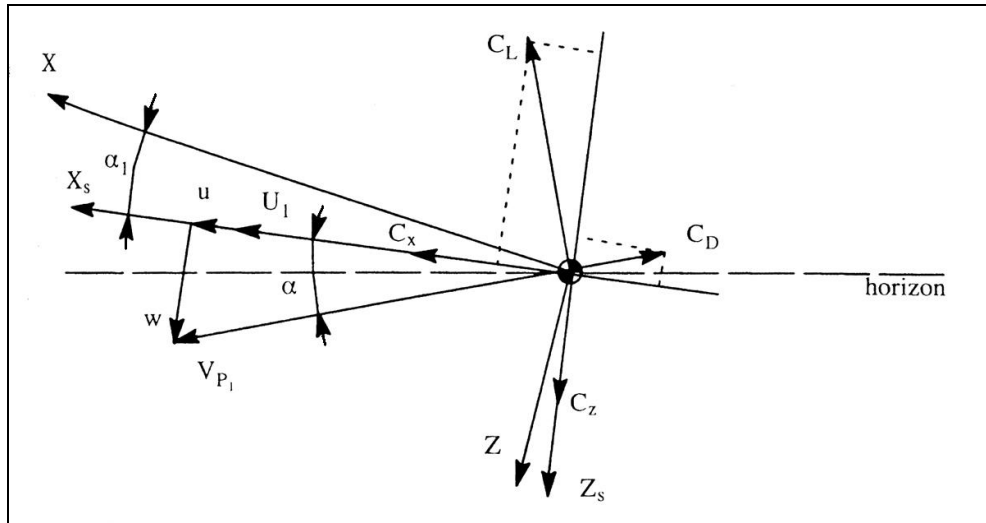
Figure 10. Relations between C_x, C_y and C_L, C_D [8]

Referring to Figure 10 and using the small angle assumption (small α), C_x can be expressed in terms of airplane drag coefficient C_D and lift coefficient C_L as

30

$$C_x = -C_D + C_L \alpha \tag{2.63}$$

Partial differentiation of Equation (2.63) with respect to u/U_1 yields

$$\frac{\partial C_x}{\partial \left(\dfrac{u}{U_1} \right)} = -\frac{\partial C_D}{\partial \left(\dfrac{u}{U_1} \right)} + \frac{\partial C_L}{\partial \left(\dfrac{u}{U_1} \right)} \alpha = -\frac{\partial C_D}{\partial \left(\dfrac{u}{U_1} \right)} = -C_{D,u} \tag{2.64}$$

where $C_{D,u}$ is the variation of airplane drag coefficient with dimensionless speed (or the speed damping derivative).

From Equation (2.63), the steady state value of C_x is found as

$$C_{x,1} = -C_{D,1} \tag{2.65}$$

The partial differentiation of $\bar{q}$ gives

$$\frac{\partial \bar{q}}{\partial \left(\dfrac{u}{U_1} \right)} = U_1 \frac{\partial \bar{q}}{\partial u} = U_1 \frac{\partial \dfrac{1}{2} \rho (U_1 + u)^2}{\partial u} = U_1 \rho (U_1 + u) = \rho U_1^2 \tag{2.66}$$

Substituting Equations (2.64) through (2.66) into Equation (2.62), we get

$$\frac{\partial F_{A,x}}{\partial \left(\dfrac{u}{U_1} \right)} = -\left(C_{D,u} + 2C_{D,1} \right) \bar{q}_1 S \tag{2.67}$$

Next is the partial differentiation of the aerodynamic force component $F_{A,z}$, expressed by Equation (2.60), with respect to u/U_1.

$$\frac{\partial F_{A,z}}{\partial\left(\dfrac{u}{U_1}\right)} = \frac{\partial C_z}{\partial\left(\dfrac{u}{U_1}\right)}\overline{q}S + C_z S\frac{\partial\overline{q}}{\partial\left(\dfrac{u}{U_1}\right)} \qquad\qquad (2.68)$$

Referring to Figure 10 and using the small angle assumption (small α), C_z can be expressed in terms of C_D and C_L as

$$C_z = -C_L - C_D\alpha \qquad\qquad (2.69)$$

The partial differentiation of Equation (2.69) yields

$$\frac{\partial C_z}{\partial\left(\dfrac{u}{U_1}\right)} = -\frac{\partial C_L}{\partial\left(\dfrac{u}{U_1}\right)} - \frac{\partial C_D}{\partial\left(\dfrac{u}{U_1}\right)}\alpha = -\frac{\partial C_L}{\partial\left(\dfrac{u}{U_1}\right)} = -C_{L,u} \qquad\qquad (2.70)$$

where $C_{L,u}$ is the variation of airplane lift coefficient with dimensionless speed. From Equation (2.69) the steady state value of C_z is found as

$$C_{z,1} = -C_{L,1} \qquad\qquad (2.71)$$

Substituting Equations (2.66), (2.70), and (2.71) into the Equation (2.68), we get

$$\frac{\partial F_{A,z}}{\partial\left(\dfrac{u}{U_1}\right)} = -\left(C_{L,u} + 2C_{L,1}\right)\overline{q}_1 S \qquad\qquad (2.72)$$

Finally, the aerodynamic moment M_A, expressed by Equation (2.61), is partially differentiated with respect to u/U_1 to give

$$\frac{\partial M_A}{\partial\left(\dfrac{u}{U_1}\right)} = \frac{\partial C_m}{\partial\left(\dfrac{u}{U_1}\right)}\overline{q}S\overline{c} + C_m\frac{\partial\overline{q}}{\partial\left(\dfrac{u}{U_1}\right)}S\overline{c} \qquad (2.73)$$

Substituting Equation (2.66) into Equation (2.73), we get

$$\frac{\partial M_A}{\partial\left(\dfrac{u}{U_1}\right)} = \left(C_{m,u} + 2C_{m,1}\right)\overline{q}_1 S\overline{c} \qquad (2.74)$$

where $C_{m,u}$ is the variation of airplane pitching moment coefficient with dimensionless speed and it can be obtained from the following relation.

$$C_{m,u} = M_1\frac{\partial C_m}{\partial M} \qquad (2.75)$$

2.2.1.2 PARTIAL DIFFERENTIATION WITH RESPECT TO ANGLE OF ATTACK

The partial differentiation of the aerodynamic force component $F_{A,x}$, expressed by Equation (2.59), with respect to angle of attack is

$$\frac{\partial F_{A,x}}{\partial\alpha} = \frac{\partial C_x}{\partial\alpha}\overline{q}S \qquad (2.76)$$

Partial differentiating Equation (2.63) with respect to α, we get

$$\frac{\partial C_x}{\partial\alpha} = -\frac{\partial C_D}{\partial\alpha} + \frac{\partial C_L}{\partial\alpha}\alpha + C_L \qquad (2.77)$$

At steady state conditions, Equation (2.77) becomes

$$C_{x,\alpha} = -C_{D,\alpha} + C_{L,1} \tag{2.78}$$

Substituting Equation (2.78) into Equation (2.76), we get

$$\frac{\partial F_{A,x}}{\partial \alpha} = \left(-C_{D,\alpha} + C_{L,1}\right)\overline{q}_1 S \tag{2.79}$$

where $C_{D,\alpha}$ is the variation of airplane drag coefficient with angle of attack, and it can be obtained from the following relation.

$$C_{D,\alpha} = \frac{2C_{L,1}C_{L,\alpha}}{\pi A e} \tag{2.80}$$

where A is the aspect ratio of the wing (whose formal definition is given later in Chapter 3), e is the Oswald's efficiency factor, and $C_{L,\alpha}$ is the variation of airplane lift coefficient with angle of attack.

Next is the partial differentiation of the aerodynamic force component $F_{A,z}$, expressed by Equation (2.60), with respect to angle of attack.

$$\frac{\partial F_{A,z}}{\partial \alpha} = \frac{\partial C_z}{\partial \alpha}\overline{q}S \tag{2.81}$$

Partial differentiating Equation (2.69) with respect to α, we get

$$\frac{\partial C_z}{\partial \alpha} = -\frac{\partial C_L}{\partial \alpha} - \frac{\partial C_D}{\partial \alpha}\alpha - C_D \tag{2.82}$$

At steady state conditions, Equation (2.82) becomes

$$C_{z,\alpha} = -C_{L,\alpha} - C_{D,1} \tag{2.83}$$

Substituting Equation (2.83) into Equation (2.81), we get

$$\frac{\partial F_{A,z}}{\partial \alpha} = -\left(C_{L,\alpha} + C_{D,1}\right)\overline{q}_1 S \tag{2.84}$$

Finally, the aerodynamic moment M_A, expressed by Equation (2.61), is partially differentiated with respect to angle of attack.

$$\frac{\partial M_A}{\partial \alpha} = \frac{\partial C_m}{\partial \alpha}\overline{q}S\overline{c} \tag{2.85}$$

At steady state conditions, Equation (2.85) becomes

$$\frac{\partial M_A}{\partial \alpha} = C_{m,\alpha}\overline{q}_1 S\overline{c} \tag{2.86}$$

where $C_{m,\alpha}$ is the variation of airplane pitching moment coefficient with angle of attack.

2.2.1.3   PARTIAL DIFFERENTIATION WITH RESPECT TO ANGLE OF ATTACK RATE

The partial differentiation of the aerodynamic force component $F_{A,x}$, expressed by Equation (2.59), with respect to angle of attack rate gives

$$\frac{\partial F_{A,x}}{\partial\left(\dfrac{\dot{\alpha}\overline{c}}{2U_1}\right)} = \frac{\partial C_x}{\partial\left(\dfrac{\dot{\alpha}\overline{c}}{2U_1}\right)}\overline{q}S = C_{x,\dot{\alpha}}\overline{q}S \tag{2.87}$$

From Equation (2.63), the following relation can be shown.

$$C_{x,\dot{\alpha}} = -C_{D,\dot{\alpha}} \qquad (2.88)$$

where $C_{D,\dot{\alpha}}$ is the variation of airplane drag coefficient with dimensionless rate of change of angle of attack. Hence, Equation (2.87) becomes

$$\frac{\partial F_{A,x}}{\partial \left(\dfrac{\dot{\alpha}\bar{c}}{2U_1} \right)} = -C_{D,\dot{\alpha}} \bar{q}_1 S = 0 \qquad (2.89)$$

where it is assumed that the effect of downwash lag on drag can be neglected [8], $C_{D,\dot{\alpha}} \approx 0$.

Next is the partial differentiation of the aerodynamic force component $F_{A,z}$, expressed by Equation (2.60), with respect to angle of attack rate.

$$\frac{\partial F_{A,z}}{\partial \left(\dfrac{\dot{\alpha}\bar{c}}{2U_1} \right)} = \frac{\partial C_z}{\partial \left(\dfrac{\dot{\alpha}\bar{c}}{2U_1} \right)} \bar{q}S = C_{z,\dot{\alpha}} \bar{q}S \qquad (2.90)$$

From Equation (2.69), the following relation can be shown.

$$C_{z,\dot{\alpha}} = -C_{L,\dot{\alpha}} \qquad (2.91)$$

where $C_{L,\dot{\alpha}}$ is the variation of airplane lift coefficient with dimensionless rate of change of angle of attack. Hence, Equation (2.90) becomes

$$\frac{\partial F_{A,x}}{\partial \left(\dfrac{\dot{\alpha}\bar{c}}{2U_1} \right)} = -C_{L,\dot{\alpha}} \bar{q}_1 S \qquad (2.92)$$

Finally, the aerodynamic moment M_A, expressed by Equation (2.61), is partially differentiated with respect to angle of attack rate.

$$\frac{\partial M_A}{\partial\left(\dfrac{\dot{\alpha}\overline{c}}{2U_1}\right)} = \frac{\partial C_m}{\partial\left(\dfrac{\dot{\alpha}\overline{c}}{2U_1}\right)}\overline{q}S\overline{c} = C_{m,\dot{\alpha}}\overline{q}_1 S\overline{c} \tag{2.93}$$

where $C_{m,\dot{\alpha}}$ is the variation of airplane pitching moment coefficient with dimensionless rate of change of angle of attack.

2.2.1.4 PARTIAL DIFFERENTIATION WITH RESPECT TO PITCH RATE

The partial differentiation of the aerodynamic force component $F_{A,x}$, expressed by Equation (2.59), with respect to pitch rate is

$$\frac{\partial F_{A,x}}{\partial\left(\dfrac{q\overline{c}}{2U_1}\right)} = \frac{\partial C_x}{\partial\left(\dfrac{\dot{\alpha}\overline{c}}{2U_1}\right)}\overline{q}S = C_{x,q}\overline{q}S \tag{2.94}$$

From Equation (2.63), the following relation can be shown.

$$C_{x,q} = -C_{D,q} \tag{2.95}$$

where $C_{D,q}$ is the variation of airplane drag coefficient with dimensionless pitch rate. Hence, Equation (2.94) becomes

$$\frac{\partial F_{A,x}}{\partial\left(\dfrac{\dot{\alpha}\overline{c}}{2U_1}\right)} = -C_{D,q}\overline{q}_1 S = 0 \tag{2.96}$$

where it is assumed that the effect of pitch rate on drag can be neglected [8], $C_{D,q} \approx 0$.

Next is the partial differentiation of the aerodynamic force component $F_{A,z}$, expressed by Equation (2.60), with respect to pitch rate.

$$\frac{\partial F_{A,z}}{\partial \left(\dfrac{q\overline{c}}{2U_1} \right)} = \frac{\partial C_z}{\partial \left(\dfrac{q\overline{c}}{2U_1} \right)} \overline{q}S = C_{z,q}\overline{q}S \tag{2.97}$$

From Equation (2.69), the following relation can be shown.

$$C_{z,q} = -C_{L,q} \tag{2.98}$$

where $C_{L,q}$ is the variation of airplane lift coefficient with dimensionless pitch rate. Hence, Equation (2.97) becomes

$$\frac{\partial F_{A,x}}{\partial \left(\dfrac{\dot{\alpha}\overline{c}}{2U_1} \right)} = -C_{L,q}\overline{q}_1 S \tag{2.99}$$

Finally, the aerodynamic moment M_A, expressed by Equation (2.61), is partially differentiated with respect to pitch rate.

$$\frac{\partial M_A}{\partial \left(\dfrac{q\overline{c}}{2U_1} \right)} = \frac{\partial C_m}{\partial \left(\dfrac{q\overline{c}}{2U_1} \right)} \overline{q}S = C_{m,q}\overline{q}_1 S \tag{2.100}$$

where $C_{m,q}$ is the variation of airplane pitching moment coefficient with dimensionless pitch rate.

2.2.1.5 PARTIAL DIFFERENTIATION WITH RESPECT TO ELEVATOR DEFLECTION

The partial differentiation of the aerodynamic force component $F_{A,x}$, expressed by Equation (2.59), with respect to elevator deflection is

$$\frac{\partial F_{A,x}}{\partial \delta_e} = \frac{\partial C_x}{\partial \delta_e} \overline{q} S = C_{x,\delta_e} \overline{q} S \tag{2.101}$$

From Equation (2.63), the following relation can be shown.

$$C_{x,\delta_e} = -C_{D,\delta_e} \tag{2.102}$$

where C_{D,δ_e} is the variation of airplane drag coefficient with elevator deflection angle. Hence, Equation (2.101) becomes

$$\frac{\partial F_{A,x}}{\partial \delta_e} = -C_{D,\delta_e} \overline{q}_1 S \tag{2.103}$$

Next is the partial differentiation of the aerodynamic force component $F_{A,z}$, expressed by Equation (2.60), with respect to elevator deflection.

$$\frac{\partial F_{A,z}}{\partial \delta_e} = \frac{\partial C_z}{\partial \delta_e} \overline{q} S = C_{z,\delta_e} \overline{q} S \tag{2.104}$$

From Equation (2.69), the following relation can be shown.

$$C_{z,\delta_e} = -C_{L,\delta_e} \tag{2.105}$$

where C_{L,δ_e} is the variation of airplane lift coefficient with elevator deflection angle. Hence, Equation (2.104) becomes

$$\frac{\partial F_{A,z}}{\partial \delta_e} = -C_{L,\delta_e} \overline{q}_1 S \tag{2.106}$$

Finally, the aerodynamic moment M_A, expressed by Equation (2.61), is partially differentiated with respect to elevator deflection.

$$\frac{\partial M_A}{\partial \delta_e} = \frac{\partial C_m}{\partial \delta_e} \overline{q} S \overline{c} = C_{m,\delta_e} \overline{q}_1 S \overline{c} \tag{2.107}$$

where C_{m,δ_e} is the variation of airplane pitching moment coefficient with elevator deflection angle.

2.2.1.6   ASSEMBLING AERODYNAMIC FORCES AND MOMENTS

The perturbed state longitudinal aerodynamic forces and moments are expressed by Equations (2.56) through (2.58) in terms of the partial derivatives with respect to the perturbation variables. Substituting the partial derivative terms obtained in Sections 2.2.1.1 through 2.2.1.5 to these equations, a general form of the perturbed state longitudinal aerodynamic forces and moments can be obtained.

Substituting Equations (2.67), (2.79), (2.89), (2.96), and (2.103) into the Equation (2.56) we get

$$\frac{f_{A,x}}{\overline{q}_1 S} = -\left(C_{D,u} + 2C_{D,1}\right)\frac{u}{U_1} - \left(C_{D,\alpha} - C_{L,1}\right)\alpha - C_{D,\delta_e}\delta_e \tag{2.108}$$

Substituting Equations (2.72), (2.84), (2.92), (2.99), and (2.106) into the Equation (2.57) we get

$$\frac{f_{A,z}}{\bar{q}_1 S} = -\left(C_{L,u} + 2C_{L,1}\right)\frac{u}{U_1} - \left(C_{L,\alpha} + C_{D,1}\right)\alpha - C_{L,\dot{\alpha}}\frac{\dot{\alpha}\bar{c}}{2U_1} - C_{L,q}\frac{q\bar{c}}{2U_1} - C_{L,\delta_e}\delta_e \qquad (2.109)$$

Substituting Equations (2.74), (2.86), (2.93), (2.100), and (2.107) into the Equation (2.58) we get

$$\frac{m_A}{\bar{q}_1 S\bar{c}} = \left(C_{m,u} + 2C_{m,1}\right)\frac{u}{U_1} + C_{m,\alpha}\alpha + C_{m,\dot{\alpha}}\frac{\dot{\alpha}\bar{c}}{2U_1} + C_{m,q}\frac{q\bar{c}}{2U_1} + C_{m,\delta_e}\delta_e \qquad (2.110)$$

2.2.2 PERTURBED STATE THRUST FORCES AND MOMENTS

Dealing with the longitudinal dynamics, only the perturbation variables u and w (=$U_1\alpha$) have significant effects on the perturbed thrust forces and moments [8]. Hence, the first order Taylor series expansions of perturbed state longitudinal thrust forces and moments are expressed as;

$$f_{T,x} = \frac{\partial F_{T,x}}{\partial\left(\frac{u}{U_1}\right)}\frac{u}{U_1} + \frac{\partial F_{T,x}}{\partial\alpha}\alpha \qquad (2.111)$$

$$f_{T,z} = \frac{\partial F_{T,z}}{\partial\left(\frac{u}{U_1}\right)}\frac{u}{U_1} + \frac{\partial F_{T,z}}{\partial\alpha}\alpha \qquad (2.112)$$

$$m_T = \frac{\partial M_T}{\partial\left(\frac{u}{U_1}\right)}\frac{u}{U_1} + \frac{\partial M_T}{\partial\alpha}\alpha \qquad (2.113)$$

Thrust forces and moments are defined in the stability axis system as

$$F_{T,x} = C_{T,x} \overline{q} S \tag{2.114}$$

$$F_{T,z} = C_{T,z} \overline{q} S \tag{2.115}$$

$$M_T = C_{m,T} \overline{q} S \overline{c} \tag{2.116}$$

where $C_{m,T}$ is the pitching moment coefficient of the airplane due to thrust, $C_{T,x}$ and $C_{T,z}$ are the thrust force coefficient components along x and z axis of the body-fixed coordinate system.

The partial derivatives of the thrust forces and moments in Equations (2.111) through (2.113) are derived in the following sections.

2.2.2.1 PARTIAL DIFFERENTIATION WITH RESPECT TO u/U$_1$

The partial differentiation of the thrust force component $F_{T,x}$, expressed by Equation (2.114), with respect to u/U_1 is

$$\frac{\partial F_{T,x}}{\partial \left(\dfrac{u}{U_1} \right)} = \frac{\partial C_{T,x}}{\partial \left(\dfrac{u}{U_1} \right)} \overline{q} S + C_{T,x} S \frac{\partial \overline{q}}{\partial \left(\dfrac{u}{U_1} \right)} \tag{2.117}$$

Using Equation (2.66), Equation (2.117) at steady state becomes

$$\frac{\partial F_{T,x}}{\partial \left(\dfrac{u}{U_1} \right)} = C_{T,x_u} \overline{q}_1 S + 2 C_{T,x_1} \overline{q}_1 S \tag{2.118}$$

The steady state thrust coefficient C_{T,x_1} is normally equal to the steady state drag coefficient $C_{D,1}$ because the thrust is equal to the drag in a level steady state flight [8]. Hence;

$$C_{T,x_1} = C_{D,1} \tag{2.119}$$

Here, C_{T,x_u} (the variation of the airplane thrust coefficient along x with dimensionless speed) depends on the propulsion system, which in our case is a variable pitch propeller. To drive a relation for C_{T,x_u}, it is assumed that the thrust axis is aligned with the x axis of the body-fixed coordinate system and the thrust output is nearly constant with small changes in forward speed [8]. Hence;

$$T(U_1 + u) \approx F_{T,x}(U_1 + u) \approx \text{constant} \tag{2.120}$$

Partial differentiating with respect to u/U_1 at the steady state flight condition (u=0) yields

$$\frac{\partial F_{T,x}}{\partial \left(\dfrac{u}{U_1}\right)} = -F_{T,x_1} = -C_{T,x_1} \overline{q}_1 S \tag{2.121}$$

From Equations (2.118) and (2.121) it can easily be shown that

$$C_{T,x_u} = -3C_{T,x_1} \tag{2.122}$$

Next is the partial differentiation of the thrust force component $F_{T,z}$, expressed by Equation (2.115), with respect to u/U_1.

$$\frac{\partial F_{T,z}}{\partial\left(\dfrac{u}{U_1}\right)} = \frac{\partial C_{T,z}}{\partial\left(\dfrac{u}{U_1}\right)}\overline{q}S + C_{T,z}S\frac{\partial\overline{q}}{\partial\left(\dfrac{u}{U_1}\right)} \tag{2.123}$$

Using Equation (2.66), Equation (2.123) at steady state becomes

$$\frac{\partial F_{T,z}}{\partial\left(\dfrac{u}{U_1}\right)} = C_{T,z_u}\overline{q}_1 S + 2C_{T,z_1}\overline{q}_1 S \tag{2.124}$$

Here, C_{T,z_u} (the variation of the airplane thrust coefficient along z with dimensionless speed) and C_{T,z_1} (the steady state thrust force coefficient component along z) are negligible for most airplanes [8]. Thus;

$$\frac{\partial F_{T,z}}{\partial\left(\dfrac{u}{U_1}\right)} = 0 \tag{2.125}$$

Finally, the thrust moment M_T, expressed by Equation (2.116), is partially differentiated with respect to u/U_1.

$$\frac{\partial M_T}{\partial\left(\dfrac{u}{U_1}\right)} = \frac{\partial C_{m,T}}{\partial\left(\dfrac{u}{U_1}\right)}\overline{q}S\overline{c} + C_{m,T}\frac{\partial\overline{q}}{\partial\left(\dfrac{u}{U_1}\right)}S\overline{c} \tag{2.126}$$

Using Equation (2.66), Equation (2.126) at steady state becomes

$$\frac{\partial M_T}{\partial\left(\dfrac{u}{U_1}\right)} = C_{m,T_u}\overline{q}_1 S\overline{c} + 2C_{m,T_1}\overline{q}_1 S\overline{c} \tag{2.127}$$

For airplanes whose thrust lines are close to their centers of mass, the value of C_{m,T_u} (the variation of airplane pitching moment coefficient due to thrust with dimensionless speed) can be neglected and considering the equilibrium of pitching moment in a steady state flight, the value of C_{m,T_1} can be found from the following relation [8].

$$C_{m,1} + C_{m,T_1} = 0 \tag{2.128}$$

2.2.2.2   PARTIAL DIFFERENTIATION WITH RESPECT TO ANGLE OF ATTACK

The partial differentiation of the thrust force component $F_{T,x}$, expressed by Equation (2.114), with respect to angle of attack is

$$\frac{\partial F_{T,x}}{\partial \alpha} = \frac{\partial C_{T,x}}{\partial \alpha} \overline{q} S \tag{2.129}$$

Using the notation $C_{T,x_\alpha} = \dfrac{\partial C_{T,x}}{\partial \alpha}$, Equation (2.129) at steady state becomes

$$\frac{\partial F_{T,x}}{\partial \alpha} = C_{T,x_\alpha} \overline{q}_1 S \tag{2.130}$$

For most airplanes with small angles of attack, the value of C_{T,x_α} (the variation of airplane thrust coefficient along x with angle of attack) can be neglected [8], which yields

$$\frac{\partial F_{T,x}}{\partial \alpha} \approx 0 \tag{2.131}$$

Next is the partial differentiation of the thrust force component $F_{T,z}$, expressed by Equation (2.115), with respect to angle of attack.

$$\frac{\partial F_{T,z}}{\partial \alpha} = \frac{\partial C_{T,z}}{\partial \alpha} \overline{q} S \qquad (2.132)$$

Using the notation $C_{T,z_\alpha} = \frac{\partial C_{T,z}}{\partial \alpha}$, Equation (2.132) at steady state becomes

$$\frac{\partial F_{T,z}}{\partial \alpha} = C_{T,z_\alpha} \overline{q}_1 S \qquad (2.133)$$

The physical cause of C_{T,z_α} (the variation of airplane thrust coefficient along z with angle of attack) is the propeller force due to perturbations in angle of attack. However, the magnitude of this force is relatively small, so that its value can be neglected [8]. Hence, Equation (2.133) becomes

$$\frac{\partial F_{T,z}}{\partial \alpha} \approx 0 \qquad (2.134)$$

Finally, the thrust moment M_T, expressed by Equation (2.116), is partially differentiated with respect to angle of attack to give

$$\frac{\partial M_T}{\partial \alpha} = \frac{\partial C_{m,T}}{\partial \alpha} \overline{q} S \overline{c} \qquad (2.135)$$

Using the notation $\frac{\partial C_{m,T}}{\partial \alpha} = C_{m,T_\alpha}$, Equation (2.135) at steady state becomes

$$\frac{\partial M_T}{\partial \alpha} = C_{m,T_\alpha} \overline{q}_1 S \overline{c} \qquad (2.136)$$

where C_{m,T_α} is the variation of airplane pitching moment coefficient due to thrust with angle of attack.

2.2.2.3 ASSEMBLING THRUST FORCES AND MOMENTS

The perturbed state longitudinal thrust forces and moments are expressed by Equations (2.111) through (2.113) in terms of the partial derivatives with respect to the perturbation variables. Substituting the partial derivative terms obtained in Sections 2.2.2.1 and 2.2.2.2 to these equations, the general form of the perturbed state longitudinal thrust forces and moments can be obtained.

Substituting Equations (2.118) and (2.131) into Equation (2.111), we get

$$\frac{f_{T,x}}{\overline{q}_1 S} = \left(C_{T,x_u} + 2C_{T,x_1}\right)\frac{u}{U_1} \tag{2.137}$$

Substituting Equations (2.125) and (2.134) into Equation (2.112), we get

$$\frac{f_{T,z}}{\overline{q}_1 S} = 0 \tag{2.138}$$

Substituting Equations (2.127) and (2.136) into Equation (2.113), we get

$$\frac{m_T}{\overline{q}_1 S \overline{c}} = \left(C_{m,T_u} + 2C_{m,T_1}\right)\frac{u}{U_1} + C_{m,T_\alpha}\alpha \tag{2.139}$$

2.3 TRANSFER FUNCTIONS

In this section, transfer functions of an airplane in a perturbed state flight are derived. Then, a relation between the airplane altitude and its elevator deflection is established and the corresponding transfer function for altitude to elevator deflection is derived by using the longitudinal transfer functions.

2.3.1 TRANSFER FUNCTIONS OF LONGITUDINAL DYNAMICS

Using the expressions obtained in Section 2.2 for the aerodynamic and thrust forces and moments, the longitudinal equations of motion in perturbed state flight can be expressed as follows.

$$
m\dot{u} = -mg\theta\cos\theta_1 + \overline{q}_1 S \left\{ -(C_{D,u} + 2C_{D,1})\frac{u}{U_1} + (C_{T,x_u} + 2C_{T,x_1})\frac{u}{U_1} + \right.
$$
$$
\left. -(C_{D,\alpha} - C_{L,1})\alpha - C_{D,\delta_e}\delta_e \right\} \tag{2.140}
$$

$$
m(\dot{w} - U_1 q) = -mg\theta\sin\theta_1 + \overline{q}_1 S \left\{ -(C_{L,u} + 2C_{L,1})\frac{u}{U_1} - (C_{L,\alpha} + C_{D,1})\alpha + \right.
$$
$$
\left. -C_{L,\dot{\alpha}}\frac{\dot{\alpha}\overline{c}}{2U_1} - C_{L,q}\frac{q\overline{c}}{2U_1} - C_{L,\delta_e}\delta_e \right\} \tag{2.141}
$$

$$
I_{yy}\dot{q} = \overline{q}_1 S\overline{c} \left\{ (C_{m,u} + 2C_{m,1})\frac{u}{U_1} + (C_{m,T_u} + 2C_{m,T_1})\frac{u}{U_1} + C_{m,\alpha}\alpha + C_{m,T_\alpha}\alpha + \right.
$$
$$
\left. C_{m,\dot{\alpha}}\frac{\dot{\alpha}\overline{c}}{2U_1} + C_{m,q}\frac{q\overline{c}}{2U_1} - C_{m,\delta_e}\delta_e \right\} \tag{2.142}
$$

with $q = \dot{\theta}$ and $w = U_1\alpha$

Notice that, since the steady state velocity in the z axis of the body-fixed coordinate system (W_1) is zero, it is neglected in the equations of motion.

In order to ease the work with Equations (2.140) through (2.142), the force equations are divided by the mass (m), and the pitching moment equation is divided by the pitching moment of inertia (I_{yy}). Then, the resulting equations are rewritten by using the so-called dimensional stability derivatives [8] given by Equations (2.143) through (2.158).

$$X_u = \frac{-\overline{q}_1 S(C_{D,u} + 2C_{D,1})}{mU_1} \tag{2.143}$$

$$X_{T,u} = \frac{\overline{q}_1 S(C_{T,x_u} + 2C_{T,x_1})}{mU_1} \tag{2.144}$$

$$X_\alpha = \frac{-\overline{q}_1 S(C_{D,\alpha} - C_{L,1})}{m} \tag{2.145}$$

$$X_{\delta_e} = \frac{-\overline{q}_1 S C_{D,\delta_e}}{m} \tag{2.146}$$

$$Z_u = \frac{-\overline{q}_1 S(C_{L,u} + 2C_{L,1})}{mU_1} \tag{2.147}$$

$$Z_\alpha = \frac{-\overline{q}_1 S(C_{L,\alpha} + C_{D,1})}{m} \tag{2.148}$$

$$Z_{\dot{\alpha}} = \frac{-\overline{q}_1 S \overline{c} C_{L,\dot{\alpha}}}{2mU_1} \tag{2.149}$$

$$Z_q = \frac{-\overline{q}_1 S \overline{c} C_{L,q}}{2mU_1} \tag{2.150}$$

$$Z_{\delta_e} = \frac{-\overline{q}_1 S C_{L,\delta_e}}{m} \tag{2.151}$$

$$M_u = \frac{\overline{q}_1 S \overline{c}(C_{m,u} + 2C_{m,1})}{I_{yy} U_1} \tag{2.152}$$

$$M_{T,u} = \frac{\overline{q}_1 S \overline{c}(C_{m,T_u} + 2C_{m,T_1})}{I_{yy} U_1} \tag{2.153}$$

$$M_\alpha = \frac{\overline{q}_1 S \overline{c} C_{m,\alpha}}{I_{yy}} \tag{2.154}$$

$$M_{T,\alpha} = \frac{\overline{q}_1 S \overline{c} C_{m,T_\alpha}}{I_{yy}} \tag{2.155}$$

$$M_{\dot{\alpha}} = \frac{\overline{q}_1 S \overline{c}^2 C_{m,\dot{\alpha}}}{2I_{yy} U_1} \tag{2.156}$$

$$M_q = \frac{\overline{q}_1 S \overline{c}^2 C_{m,q}}{2I_{yy} U_1} \tag{2.157}$$

$$M_{\delta_e} = \frac{\overline{q}_1 S \overline{c} C_{m,\delta_e}}{I_{yy}} \tag{2.158}$$

As a result, the newly formed longitudinal equations of motion in terms of dimensional stability derivatives become

$$\dot{u} = -g\theta\cos\theta_1 + X_u u + X_{T,u} u + X_\alpha \alpha + X_{\delta_e}\delta_e \qquad (2.159)$$

$$U_1\dot{\alpha} - U_1\dot{\theta} = -g\theta\sin\theta_1 + Z_u u + Z_\alpha \alpha + Z_{\dot{\alpha}}\dot{\alpha} + Z_q\dot{\theta} + Z_{\delta_e}\delta_e \qquad (2.160)$$

$$\ddot{\theta} = M_u u + M_{T,u} u + M_\alpha \alpha + M_{T,\alpha}\alpha + M_{\dot{\alpha}}\dot{\alpha} + M_q\dot{\theta} + M_{\delta_e}\delta_e \qquad (2.161)$$

The Laplace transformation of Equations (2.159)-(2.161) with zero initial conditions gives the following equations expressed in matrix format.

$$\begin{bmatrix} (s-X_u-X_{T,u}) & -X_\alpha & g\cos\theta_1 \\ -Z_u & s(U_1-Z_{\dot{\alpha}})-Z_\alpha & -(Z_q+U_1)s+g\sin\theta_1 \\ -(M_u+M_{T,u}) & -(M_{\dot{\alpha}}s+M_\alpha+M_{T,\alpha}) & s^2-M_qs \end{bmatrix} \begin{bmatrix} \dfrac{u(s)}{\delta_e(s)} \\ \dfrac{\alpha(s)}{\delta_e(s)} \\ \dfrac{\theta(s)}{\delta_e(s)} \end{bmatrix} = \begin{bmatrix} X_{\delta_e} \\ Z_{\delta_e} \\ M_{\delta_e} \end{bmatrix}$$

Since our goal is to obtain the transfer function between the elevator deflection and altitude, matrix operations are carried only for the transfer function $\dfrac{\alpha(s)}{\delta_e(s)}$ between the elevator deflection and angle of attack and for the transfer function $\dfrac{\theta(s)}{\delta_e(s)}$ between the elevator deflection and pitch attitude. The idea behind this is explained in Section 2.3.2.

First, the transfer function $\dfrac{\alpha(s)}{\delta_e(s)}$ between the elevator deflection and angle of attack is obtained.

$$\frac{\alpha(s)}{\delta_e(s)} = \frac{\begin{vmatrix} (s - X_u - X_{T,u}) & -X_{\delta_e} & g\cos\theta_1 \\ -Z_u & Z_{\delta_e} & -(Z_q + U_1)s + g\sin\theta_1 \\ -(M_u + M_{T,u}) & M_{\delta_e} & s^2 - M_q s \end{vmatrix}}{\begin{vmatrix} (s - X_u - X_{T,u}) & -X_\alpha & g\cos\theta_1 \\ -Z_u & s(U_1 - Z_{\dot\alpha}) - Z_\alpha & -(Z_q + U_1)s + g\sin\theta_1 \\ -(M_u + M_{T,u}) & -(M_{\dot\alpha}s + M_\alpha + M_{T,\alpha}) & s^2 - M_q s \end{vmatrix}} \qquad (2.162)$$

Introducing the notation N_α for the numerator, and D for the denominator of Equation (2.162), we can express $\dfrac{\alpha(s)}{\delta_e(s)}$ as follows.

$$\frac{\alpha(s)}{\delta_e(s)} = \frac{N_\alpha}{D} \qquad (2.163)$$

Working out the determinant for N_α, we get

$$N_\alpha = A_\alpha s^3 + B_\alpha s^2 + C_\alpha s + D_\alpha \qquad (2.164)$$

where the constants A_α, B_α, C_α and D_α are

$$A_\alpha = Z_{\delta_e} \qquad (2.165)$$

$$B_\alpha = X_{\delta_e} Z_u + Z_{\delta_e}\left(-M_q - (X_u + X_{T,u})\right) + M_{\delta_e}\left(U_1 + Z_q\right) \qquad (2.166)$$

$$C_\alpha = X_{\delta_e}\left((U_1 + Z_q)(M_u + M_{T,u}) - M_q Z_u\right) + Z_{\delta_e} M_q(X_u + X_{T,u}) + \\ M_{\delta_e}\left(-g\sin\theta_1 - (U_1 + Z_q)(X_u + X_{T,u})\right) \qquad (2.167)$$

$$D_\alpha = -X_{\delta_e}\left(M_u + M_{T,u}\right)g\sin\theta_1 + Z_{\delta_e}\left(M_u + M_{T,u}\right)g\cos\theta_1 + \\ M_{\delta_e}\left((X_u + X_{T,u})g\sin\theta_1 - Z_u g\cos\theta_1\right) \qquad (2.168)$$

Working out the determinant for D, we get

$$D = As^4 + Bs^3 + Cs^2 + Ds + E \tag{2.169}$$

where the constants A, B, C, D and E are

$$A = U_1 - Z_{\dot{\alpha}} \tag{2.170}$$

$$B = -(U_1 - Z_{\dot{\alpha}})(X_u + X_{T,u} + M_q) - Z_\alpha - M_{\dot{\alpha}}(U_1 + Z_q) \tag{2.171}$$

$$C = (X_u + X_{T,u})(M_q(U_1 - Z_{\dot{\alpha}}) + Z_\alpha + M_{\dot{\alpha}}(U_1 + Z_q)) + M_q Z_\alpha - \\ Z_u X_\alpha + M_{\dot{\alpha}} g \sin\theta_1 - (M_\alpha + M_{T,\alpha})(U_1 + Z_q) \tag{2.172}$$

$$D = g\sin\theta_1(M_\alpha + M_{T,\alpha} - M_{\dot{\alpha}}(X_u + X_{T,u})) + \\ g\cos\theta_1(Z_u M_{\dot{\alpha}} + (M_u + M_{T,u})(U_1 - Z_{\dot{\alpha}})) + (M_u + M_{T,u})(-X_\alpha(U_1 + Z_q)) + \\ Z_u X_\alpha M_q + (X_u + X_{T,u})((M_\alpha + M_{T,\alpha})(U_1 + Z_q) - M_q Z_\alpha) \tag{2.173}$$

$$E = g\cos\theta_1((M_\alpha + M_{T,\alpha})Z_u - Z_\alpha(M_u + M_{T,u})) + \\ g\sin\theta_1((M_u + M_{T,u})X_\alpha - (X_u + X_{T,u})(M_\alpha + M_{T,\alpha})) \tag{2.174}$$

Next, the transfer function $\dfrac{\theta(s)}{\delta_e(s)}$ between the elevator deflection and pitch attitude to is obtained.

$$\frac{\theta(s)}{\delta_e(s)} = \frac{\begin{vmatrix} (s - X_u - X_{T,u}) & -X_\alpha & X_{\delta_e} \\ -Z_u & s(U_1 - Z_{\dot\alpha}) - Z_\alpha & Z_{\delta_e} \\ -(M_u + M_{T,u}) & -(M_{\dot\alpha}s + M_\alpha + M_{T,\alpha}) & M_{\delta_e} \end{vmatrix}}{\begin{vmatrix} (s - X_u - X_{T,u}) & -X_\alpha & g\cos\theta_1 \\ -Z_u & s(U_1 - Z_{\dot\alpha}) - Z_\alpha & -(Z_q + U_1)s + g\sin\theta_1 \\ -(M_u + M_{T,u}) & -(M_{\dot\alpha}s + M_\alpha + M_{T,\alpha}) & s^2 - M_q s \end{vmatrix}} \qquad (2.175)$$

Notice that the denominators of Equation (2.162) and (2.175) are the same. Hence, by introducing the notation N_θ for the numerator of Equation (2.175), we can express $\dfrac{\theta(s)}{\delta_e(s)}$ as follows.

$$\frac{\theta(s)}{\delta_e(s)} = \frac{N_\theta}{D} \qquad (2.176)$$

Working out the determinant for N_θ, we get

$$N_\theta = A_\theta s^2 + B_\theta s + C_\theta \qquad (2.177)$$

where the constants A_θ, B_θ and C_θ are

$$A_\theta = Z_{\delta_e} M_{\dot\alpha} + M_{\delta_e}\left(U_1 - Z_{\dot\alpha}\right) \qquad (2.178)$$

$$B_\theta = X_{\delta_e}\left(Z_u M_{\dot\alpha} + \left(U_1 - Z_{\dot\alpha}\right)\left(M_u + M_{T,u}\right)\right) + Z_{\delta_e}\left(\left(M_\alpha + M_{T,\alpha}\right) - M_{\dot\alpha}\left(X_u + X_{T,u}\right)\right) +$$
$$M_{\delta_e}\left(-Z_\alpha - \left(U_1 - Z_{\dot\alpha}\right)\left(X_u + X_{T,u}\right)\right) \qquad (2.179)$$

$$C_\theta = X_{\delta_e}\left(\left(M_\alpha + M_{T,\alpha}\right)Z_u - Z_\alpha\left(M_u + M_{T,u}\right)\right) +$$
$$Z_{\delta_e}\left(-\left(M_\alpha + M_{T,\alpha}\right)\left(X_u + X_{T,u}\right) + X_\alpha\left(M_u + M_{T,u}\right)\right) +$$
$$M_{\delta_e}\left(Z_\alpha\left(X_u + X_{T,u}\right) - X_\alpha Z_u\right) \qquad (2.180)$$

2.3.2 TRANSFER FUNCTION BETWEEN ALTITUDE AND ELEVATOR DEFLECTION

In Section 2.3.1 the general airplane transfer functions are derived in terms of dimensional stability derivatives. Since this thesis study deals with keeping the altitude at a constant value which can only be achieved by controlling the elevator, a relation for the altitude to elevator deflection is needed. To drive the transfer function between the elevator deflection and altitude, consider Figure 11 [15].
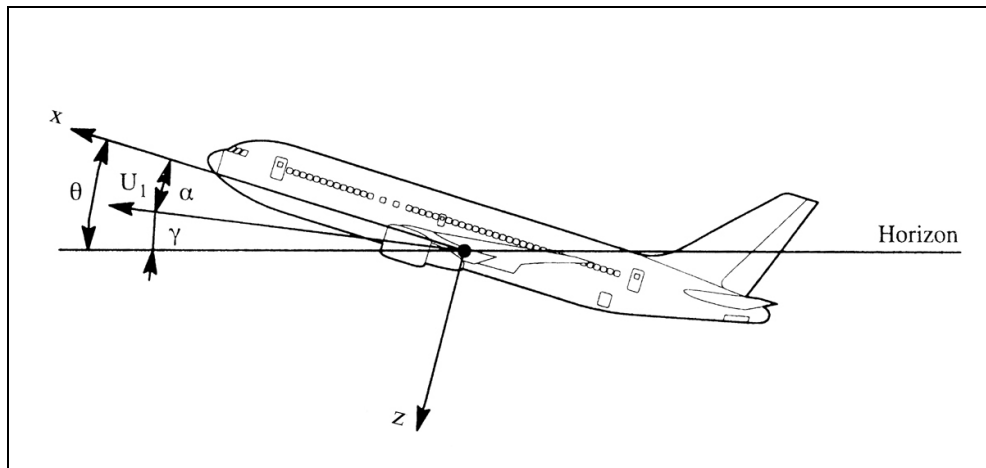
Figure 11. Flight path geometry [15]

Referring to Figure 11, the rate of climb ($\dot{h}$) of the airplane which is the velocity in the Z-axis of the Earth-fixed coordinate system (X, Y, Z) can be expressed as

$$\dot{h} = U_1 \sin \gamma \qquad\qquad (2.181)$$

Assuming that the flight path angle γ is small, this expression can be approximated as

$$\dot{h} = U_1\gamma \qquad (2.182)$$

The Laplace transformation of Equation (2.182) with zero initial conditions yields

$$sh(s) = U_1\gamma(s) \qquad (2.183)$$

Since the altitude, as the output variable, is controlled by the elevator deflection, as the input variable, dividing Equation (2.183) by $\delta_e(s)$ gives the transfer function between them as

$$\frac{h(s)}{\delta_e(s)} = \frac{U_1}{s}\left(\frac{\gamma(s)}{\delta_e(s)}\right) \qquad (2.184)$$

It can be seen from Figure 11 that, γ can be expressed in terms of θ and α as

$$\gamma = \theta - \alpha \qquad (2.185)$$

Substituting Equation (2.185) into Equation (2.184), we obtain the transfer function between the elevator deflection and altitude as

$$\frac{h(s)}{\delta_e(s)} = \frac{U_1}{s}\left(\frac{\theta(s) - \alpha(s)}{\delta_e(s)}\right) \qquad (2.186)$$

Since $\dfrac{\theta(s)}{\delta_e(s)}$ and $\dfrac{\alpha(s)}{\delta_e(s)}$ are already derived in Section 2.3.1, using Equations (2.163) and (2.176), Equation (2.186) can be expressed as

$$\frac{h(s)}{\delta_e(s)} = \frac{U_1}{s}\left(\frac{N_\theta - N_\alpha}{D}\right) \qquad (2.187)$$

56

2.4 CONCLUDING REMARKS

In this chapter, the general longitudinal equations of motion with the longitudinal (aerodynamic and thrust) forces and moments for a rigid airplane are derived. Using these equations of motion, the longitudinal transfer functions of an airplane in perturbed state flight are generated. A relationship between the airplane altitude and the elevator deflection is defined and the corresponding transfer function is derived.

At this stage, all we need is the aerodynamic derivatives of the airplane that is used as the flying platform in this study. As the aerodynamic derivatives are obtained, the dimensional derivatives can be easily calculated and by substitution of these derivates into the related equations, a full expression for the transfer function of between the elevator deflection and altitude can be established for this airplane. Thus, in the next chapter, the airplane used in this study is discussed and its aerodynamic and dimensional derivatives are established.

CHAPTER 3

RC AIRPLANE CHARACTERISTICS

The most important criteria used in choosing an airplane to be used in this study are its size and its controllability. In addition to its storage capacity which is crucial for the installation of electrical and electronic equipment, the airplane should be large enough for permitting some modifications and providing a better sight to ground observers during its flight. Since, only its longitudinal motion is to be controlled in this study, the airplane should be radio controlled in order to regulate other motions manually. Especially, any lateral motion during the flight tests should be avoided as much as possible by applying a continuous manual control via a remote control unit. However, an inherently stable RC airplane can prevent this undesirable situation and relieve the manual control on the airplane. Another criterion arises as a consequence of the line of sight problem. Since the flight path is restricted by the line of sight, the time required to fly a pattern can be increased by flying at low speeds. This is desirable because, as the time in automatic control mode increases, comments on the behavior and response of the airplane can be more accurate and richer.

3.1 TECHNICAL SPECIFICATIONS OF THE RC AIRPLANE

After a preliminary study and according to requirements defined, an RC airplane model 'Super Frontier Senior' shown in Figure 12 is selected for this thesis study.

Figure 12. RC model airplane

Specifications of this Super Frontier Senior RC airplane are given in Table 1.

Table 1. Super Frontier Senior RC airplane specifications

Airplane mass	3.8 kg
Payload mass	0.6 kg
Total mass	4.4 kg
Wing span (b)	2.05 m
Wing area (S)	0.79 m^2
Wing mean geometric chord ($\bar{c}$)	0.39 m
Fuselage length	1.52 m
Longitudinal location of c.m.	0.4 m
Pitching moment of inertia, I_{yy}	0.8 kg.m^2
Engine (O.S. Engine, type: .65 LA)	1.7 hp @ 16,000 rpm
Maximum cruise speed	30 m/s

This RC airplane is inherently stable and it can fly at low speeds. It also has a large storage capacity suitable for installing the GPS and RF transmitter equipment. A detailed geometric data of the airplane is available in Appendix B.

3.2 AERODYNAMIC DERIVATIVES OF THE RC AIRPLANE

As expressed in Section 2.3, in order to obtain the transfer function between elevator deflection and altitude, the dimensional stability derivatives of the airplane are required. It can be seen from Equations (2.143) through (2.158) that only certain stability and control derivatives of the RC airplane are needed. These derivatives are listed below.

$$C_{m,1} \quad C_{m,u} \quad C_{m,\alpha} \quad C_{m,\dot\alpha} \quad C_{m,q} \quad C_{m,T_1} \quad C_{m,T_u}$$

$$C_{m,T_\alpha} \quad C_{L,1} \quad C_{L,u} \quad C_{L,\alpha} \quad C_{L,\dot\alpha} \quad C_{L,q} \quad C_{D,1}$$

$$C_{D,u} \quad C_{D,\alpha} \quad C_{T,x_1} \quad C_{T,x_u} \quad C_{L,\delta_e} \quad C_{D,\delta_e} \quad C_{m,\delta_e}$$

The USAF DIGITAL DATCOM [16] package program (briefly referred to as DATCOM) is used to obtain some of the aerodynamic derivatives of the RC airplane. Flight conditions (speed, angle of attack values, and altitude), airplane geometry (body, wing, elevator, horizontal and vertical tail), and propeller characteristics (thrust coefficient, blade geometry) of the RC airplane are used as the input data while running this computer program.

These aerodynamic derivatives are evaluated at three different Mach numbers using the DATCOM program whose outputs that are used throughout this study are given in Table 2. These three Mach numbers are selected to represent the airplane flying speed envelope which was determined by the speed data of the UAV recorded during the flight testing of the data acquisition and communication systems. The main reason behind this multiple point evaluation of aerodynamic parameters is explained in detail in Chapter 4.

A detailed modeling of the airplane and its input file generated for the DATCOM program are presented in Appendix B. A careful consideration should be given

when working with the DATCOM outputs since it is an aerodynamic parameter estimation program after all and its outputs are only approximate.

Table 2. Aerodynamic derivatives obtained by USAF DATCOM

Symbol	Value			Unit
	@ 0.06 Mach	@ 0.07 Mach	@ 0.08 Mach	
$C_{m,1}$	0.0	0.0	0.0	-
$C_{m,\alpha}$	-0.516	-0.516	-0.516	1/rad
$C_{m,\dot{\alpha}}$	-4.067	-4.069	-4.069	1/rad
$C_{m,q}$	-8.136	-8.142	-8.142	1/rad
$C_{L,1}$	0.57	0.571	0.571	-
$C_{L,\alpha}$	5.307	5.308	5.31	1/rad
$C_{L,\dot{\alpha}}$	1.567	1.568	1.568	1/rad
$C_{L,q}$	6.068	6.073	6.073	1/rad
$C_{D,1}$	0.053	0.052	0.051	-
C_{L,δ_e}	0.47	0.474	0.474	1/rad
C_{m,δ_e}	-1.637	-1.626	-1.612	1/rad

In addition to the parameters presented in Table 2, the variation of some important aerodynamic parameters of the RC airplane with angle of attack and elevator deflection are given in the figures below. The variation of the lift coefficient C_L, drag coefficient C_D and moment coefficient C_m with angle of attack are given in Figure 13 through Figure 15, and the effect of elevator deflection in C_L and C_m is shown in Figure 16 and Figure 17. All these variations are evaluated at 0.06 Mach.
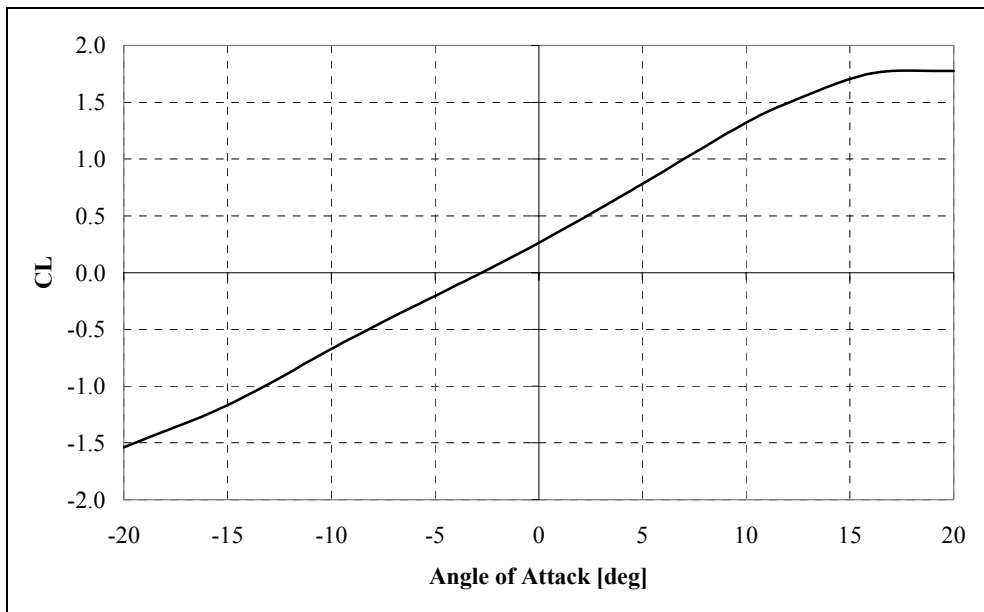
Figure 13. Variation of C$_L$ with angle of attack [deg]
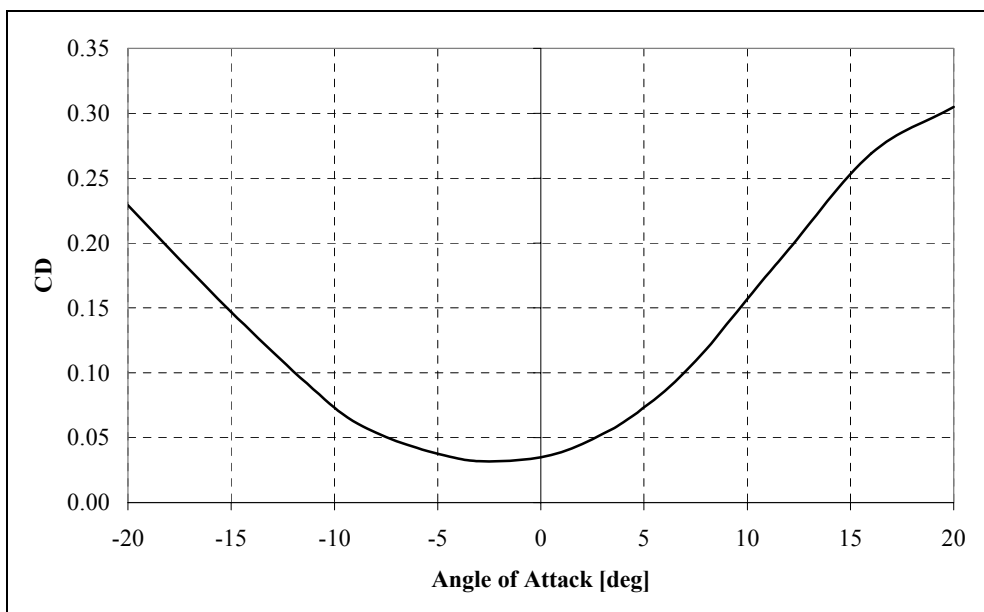
Figure 14. Variation of C$_D$ with angle of attack [deg]

Figure 15. Variation of C_m with angle of attack [deg]

Figure 16. Increment in C_L due to elevator deflection [deg]

Figure 17. Increment in C_m due to elevator deflection [deg]

However, the DATCOM program does not provide all of the required aerodynamic derivatives. Thus, the missing derivatives need to be obtained by using mathematical relations or by making some assumptions.

From the DATCOM outputs, it can be seen that the variations of pitching moment coefficient, lift coefficient, and drag coefficient with Mach number are very small and can be neglected. Hence, using Equation (2.75) as a reference yields

$$C_{m,u} = 0 \tag{3.1}$$

$$C_{L,u} = 0 \tag{3.2}$$

$$C_{D,u} = 0 \tag{3.3}$$

From Equation (2.128) and knowing that $C_{m,l} = 0$ one gets

64

$$C_{m,T_l} = 0 \tag{3.4}$$

As it is stated in Section 2.2.2.1, since the thrust line of the RC airplane is close to its center of mass, the value of C_{m,T_u} can be neglected yielding

$$C_{m,T_u} = 0 \tag{3.5}$$

For most stability and control applications, the drag change due to elevator deflection is neglected [8], which yields

$$C_{D,\delta_e} = 0 \tag{3.6}$$

For small, single piston engine general aviation airplanes (e.g. Cessna 182) the value of C_{m,T_α} is taken as zero [8]. Using this as a reference, we get

$$C_{m,T_\alpha} = 0 \tag{3.7}$$

The assumptions and aerodynamic parameters given above are valid for all three Mach number values until this point. However, from now on the mathematical relations are used and they should be evaluated separately at each Mach number value. Some sample calculations are shown only for 0.06 Mach while the results of the rest are presented as a table.

Equation (2.80) is used to obtain $C_{D,\alpha}$. Oswald's efficiency factor e is taken as 0.8 [17], and the wing aspect ratio A is calculated using its definition as

$$A = \frac{b^2}{S} = \frac{(\text{wing span})^2}{\text{wing area}} = \frac{2.05^2}{0.79} = 5.31 \tag{3.8}$$

65

Hence, $C_{D,\alpha}$ is calculated as

$$C_{D,\alpha} = \frac{2C_{L,1}C_{L,\alpha}}{\pi A e} = \frac{2 \cdot 0.57 \cdot 5.307}{\pi \cdot 5.31 \cdot 0.8} = 0.453 \qquad (3.9)$$

Using Equation (2.119), C_{T,x_1} is calculated as

$$C_{T,x_1} = C_{D,1} = 0.053 \qquad (3.10)$$

Finally, using Equation (2.122), C_{T,x_u} is calculated as

$$C_{T,x_u} = -3C_{T,x_1} = -3 \cdot 0.053 = -0.159 \qquad (3.11)$$

As a result, all stability and control derivatives of the RC airplane at three different Mach numbers are assembled and given in Table 3.

Table 3. Aerodynamic derivatives of the RC airplane

Symbol	Value			Unit
	@ 0.06 Mach	@ 0.07 Mach	@ 0.08 Mach	
$C_{m,1}$	0.0	0.0	0.0	-
$C_{m,u}$	0.0	0.0	0.0	-
$C_{m,\alpha}$	-0.516	-0.516	-0.516	1/rad
$C_{m,\dot{\alpha}}$	-4.067	-4.069	-4.069	1/rad
$C_{m,q}$	-8.136	-8.142	-8.142	1/rad
C_{m,T_1}	0.0	0.0	0.0	-
C_{m,T_u}	0.0	0.0	0.0	-
C_{m,T_α}	0.0	0.0	0.0	1/rad
$C_{L,1}$	0.570	0.571	0.571	-
$C_{L,u}$	0.0	0.0	0.0	-

Table 3. Aerodynamic derivatives of the RC airplane (continued)

Symbol	Value			Unit
	@ 0.06 Mach	@ 0.07 Mach	@ 0.08 Mach	
$C_{L,\alpha}$	5.307	5.308	5.310	1/rad
$C_{L,\dot{\alpha}}$	1.567	1.568	1.568	1/rad
$C_{L,q}$	6.068	6.073	6.073	1/rad
$C_{D,1}$	0.053	0.052	0.051	-
$C_{D,u}$	0.0	0.0	0.0	-
$C_{D,\alpha}$	0.453	0.454	0.454	1/rad
C_{T,x_1}	0.053	0.052	0.051	-
C_{T,x_u}	-0.159	-0.156	-0.153	-
C_{L,δ_e}	0.470	0.474	0.474	1/rad
C_{D,δ_e}	0.0	0.0	0.0	1/rad
C_{m,δ_e}	-1.637	-1.626	-1.612	1/rad

Examining the aerodynamic derivatives given in Table 3, it can be seen that there are small variations in most of the derivatives. However, even these small variations can have considerable effects on the dimensional stability derivatives, since they are to be multiplied with the dynamic pressure term which generally has a large value.

As we have the stability and control derivatives, the dimensional stability derivatives of the RC airplane can be obtained using Equations (2.141) through (2.156). The parameters other than the stability and control derivatives in these equations are the steady state dynamic pressure $\bar{q}_1$, the wing area S, the mean geometric chord of the wing $\bar{c}$, the mass of the airplane m, the pitching moment inertia of the airplane I_{yy}, and the steady state forward speed of the airplane U_1. The parameters S, $\bar{c}$, m, and I_{yy} of the airplane are given in Section 3.1. The steady state forward speeds of the airplane at 1,200 m above the mean sea level (the altitude of the test facility) at the given Mach numbers are calculated by the

DATCOM program, and the corresponding velocities are 20 m/s at 0.06 Mach, 23.5 m/s at 0.07 Mach, and 27 m/s at 0.08 Mach.

The steady state dynamic pressure $\bar{q}_1$ at 20 m/s flying speed can be calculated as

$$\bar{q}_1 = \frac{1}{2}\rho U_1^2 = \frac{1}{2}\cdot 1.09\cdot (20)^2 = 221\,\text{N}/\text{m}^2 \tag{3.12}$$

where the density (1.09 kg/m^3) is evaluated at the altitude of 1,200 m.

Using the stability and control derivatives given in Table 3 and the parameters $\bar{q}_1$, S, $\bar{c}$, m, I_{yy}, and U_1 of the airplane, the dimensional stability derivatives are calculated and given in Table 4.

Table 4. Dimensional stability derivatives of the RC airplane

Symbol	Value			Unit
	@ 0.06 Mach	@ 0.07 Mach	@ 0.08 Mach	
X_u	-0.21	-0.24	-0.27	1/s
$X_{T,u}$	-0.10	-0.12	-0.13	1/s
X_α	4.62	6.30	8.22	m/rad.s^2
X_{δ_e}	0.0	0.0	0.0	m/rad.s^2
Z_u	-2.24	-2.61	-2.99	1/s
Z_α	-212	-288	-376	m/rad.s^2
$Z_{\dot{\alpha}}$	-0.59	-0.69	-0.79	m/rad.s
Z_q	-2.29	-2.67	-3.06	m/rad.s
Z_{δ_e}	-18.6	-25.5	-33.3	m/rad.s^2
M_u	0.0	0.0	0.0	rad/m.s
$M_{T,u}$	0.0	0.0	0.0	rad/m.s
M_α	-42.9	-58.4	-76.2	1/s^2
$M_{T,\alpha}$	0.0	0.0	0.0	1/s^2

Table 4. Dimensional stability derivatives of the RC airplane (continued)

Symbol	Value			Unit
	@ 0.06 Mach	@ 0.07 Mach	@ 0.08 Mach	
$M_{\dot{\alpha}}$	-3.23	-3.77	-4.31	1/s
M_q	-6.46	-7.54	-8.62	1/s
M_{δ_e}	-136	-184	-238	$1/s^2$

It can easily be seen that, there are considerable variations in the dimensional stability derivatives of the airplane even though the variations of the aerodynamic derivative parameters are small.

3.3 CONCLUDING REMARKS

In this chapter, the requirements of the airplane are defined and the selected RC model airplane fulfilling these requirements is presented. As stated in the previous chapter, to obtain the altitude to elevator deflection transfer function, some stability and control derivatives of the RC airplane are needed. Most of these aerodynamic derivatives are obtained by using the aerodynamic parameter estimation program USAF DIGITAL DATCOM. Flight conditions, airplane geometry, and propeller characteristics of the RC airplane are determined and used as the input data while running this computer program. The missing aerodynamic parameters are obtained by using mathematical relationships or by making some assumptions.

Hence, the dimensional stability derivatives of the airplane are obtained in this chapter in accordance with Chapter 2. Henceforth, the transfer function between elevator deflection and altitude of the airplane is established which is to be used to design the controller system for altitude hold mode in the following chapter.

CHAPTER 4

CONTROLLER SYSTEM DESIGN AND SIMULATION

The altitude hold is an important pilot relief mode in the flight of an aircraft and it is widely used in aviation. This mode is generally used during cruise operations. In this autopilot mode, the air vehicle is held at a fixed MSL or AGL altitude during its flight. In this study, it is intended to fly the UAV at a desired flight altitude within ± 10 m limits. Hence, the controller is designed to provide the necessary control commands for the elevator position to hold the UAV within this altitude limits with small deviations. Moreover, the controller is desired to generate no corrective action when the UAV is within the altitude limits.

A simplified block diagram of the AGL altitude hold mode autopilot is shown in Figure 18 at a conceptual level. For this type of autopilot, the UAV is initially trimmed to straight and level flight. The autopilot hold mode of the flight control system is then activated. When the UAV altitude deviates from the reference input, a control signal (elevator deflection) is generated by the controller. This signal is then fed to the actuator (elevator servo) which in turn deflects the control surface (elevator), causing the air vehicle to pitch about its y-axis, and hence provides a change in its flight altitude h.

In Figure 18, h_{ref} is the reference input signal (desired flight altitude), $G_c(s)$ is the controller, δ_e is the control signal (elevator deflection angle), h is the output signal (actual flight altitude), $h_{ter,cal}$ is the calculated value of the terrain altitude, and d is the cumulative noise (due to GPS and DTED errors) in the computation of the altitude $h_{AGL.cal}$ above the ground.
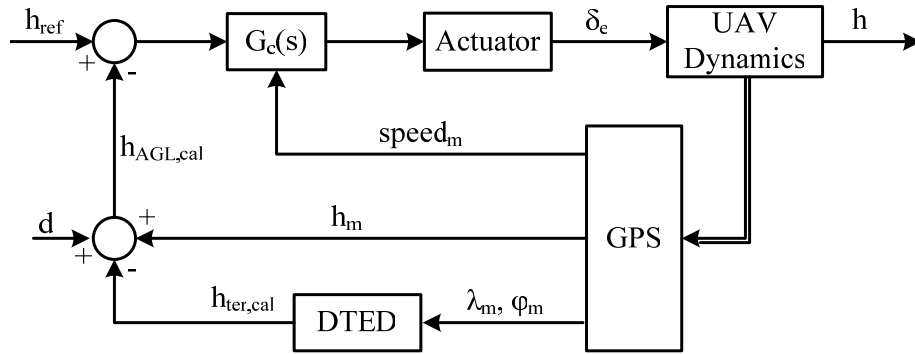
Figure 18. Altitude hold mode autopilot

Note that, the actual flight altitude h is the measured signal and its measurement h_m is provided by a GPS receiver in meters in this application. So, the system is supposed to have unity feedback, that is $H(s)=1$. The horizontal speed and the position (longitude λ and latitude φ) of the UAV are also measured by the GPS receiver. The measured position (λ_m and φ_m) of the UAV is then used to calculate the altitude $h_{ter,cal}$ of the terrain.

Also, the actuator dynamics is assumed to be much faster than the UAV dynamics, therefore it is neglected in this study for simplicity. However, in flight controls, the plant inputs are limited by some maximum and minimum allowable values. Thus, to represent these actual limitations in the flight control system, it is necessary to include some saturation and rate limiting functions in the system. The maximum and minimum allowable values for elevator deflection and its rate of change are defined in the system via an actuator model. This actuator model outputs the actual actuator position using the demanded actuator position generated by the controller.

The physical elevator deflection angle limits of the UAV are measured to be ± 25 degrees. However, this deflection angle is unrealistic and never reached during operational flights. Hence, the allowable actuator limits are set to ± 10 degrees based on the observations during the flight tests. Furthermore, the fastest speed allowable for the actuator motion is set to 0.1 rad/s (5.7 deg/s) for safety reasons.

71

4.1 GAIN SCHEDULING

The flight dynamics of the UAV in its longitudinal motion, in which the airplane is considered to be in wings level, straight line, and unaccelerated flight, can be represented by a fifth order longitudinal transfer function between the elevator deflection and altitude as derived in Chapter 2.

As the terms of this transfer function are examined, it is observed that the forward speed of the airplane appears to be a major factor affecting this relation due to its influence on the aerodynamic parameters. Due to this effect, the dynamics of the UAV changes with the speed of the vehicle.

In order to design a controller that maintains its performance over the entire speed envelope, a gain scheduling is proposed for the autopilot design problem. In the gain scheduling technique, the parameters of a linear autopilot are found at some predetermined discrete operating points using classical control techniques instead of designing a single, fixed parameter, linear autopilot using one operating point only. The gain scheduling was proven to be a successful design methodology in many applications on linear and nonlinear plants [18], [19], [20]. It was considered as a practical and intuitively acceptable methodology, since it applies linear control design methods to the linearized model of a nonlinear plant at each operating point. In gain scheduling, the first step is to linearize the plant about one or more operating points [21]. Then, linear design methods are applied to the linearized plant at each operating point to have a controller with a satisfactory performance near each operating point. The final step is the gain scheduling itself. With gain scheduling, the gains obtained by linear control designs are interpolated or scheduled between the operating points, resulting in a global controller. The controller can then response quickly to the changes in operational parameters because no estimation of system parameters is necessary. The changing rate of the controller parameters depends on how quickly the operating condition can be

measured. In general, a better performance can be achieved with this strategy than with a single controller designed for the entire operating region.

In gain scheduling, the first step is the selection of the scheduling variable and linearization of the plant about one or more operating points [21]. The scheduling variable should vary slowly to maintain a smooth transition when the air vehicle moves from one equilibrium point to another while capturing the effects of system nonlinearities. Hence, in accordance with the observed dynamics of the UAV and the fact that the angle of attack of the vehicle is relatively small (almost zero), its horizontal speed is selected as the scheduling variable in our application.

As the scheduling variable is determined, the next step is to set the operating points. In this study, several initial flight tests are performed with the UAV to determine its speed envelope. These tests are performed under relatively low wind conditions to eliminate the disturbances on the speed of the vehicle. The horizontal speed of the vehicle is found vary between 20 m/s and 27 m/s during these tests one of which is given in Figure 19.
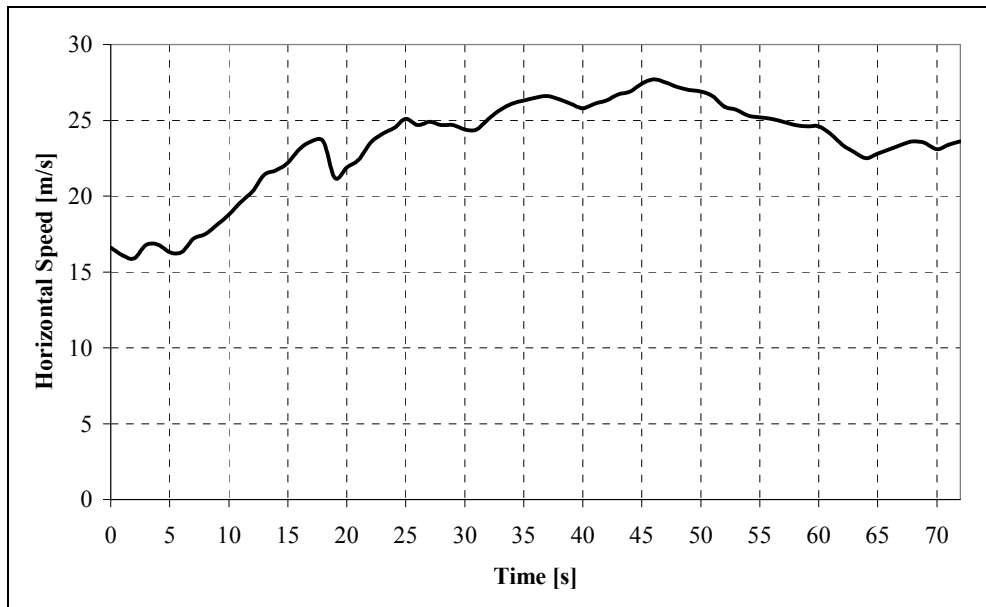

Figure 19. Horizontal speed of the UAV

73

In accordance with the flight test results, the following three distinct operating points are set for gain scheduling to represent the operating region.

- 20 m/s (0.06 Mach) – low speed operating point
- 23.5 m/s (0.07 Mach) – mid speed operating point
- 27 m/s (0.08 Mach) – high speed operating point

As the operating points are set, the linearized plants at these points can be established by referring to the preceding chapters. With the dimensional stability derivatives of the airplane obtained in Section 3.2 and presented in Table 4, the altitude to elevator deflection transfer function of the UAV can be obtained by the relations presented in Section 2.3.

From Equations (2.161) through (2.165) and using the corresponding variables in Table 4, the numerator of angle of attack to elevator transfer function N_α is found as;

@ 20 m/s (0.06 Mach)

$$N_\alpha = -61s^3 - 8379s^2 - 2607s - 9787 \tag{4.1}$$

@ 23.5 m/s (0.07 Mach)

$$N_\alpha = -84s^3 - 13215s^2 - 4706s - 15453 \tag{4.2}$$

@ 27 m/s (0.08 Mach)

$$N_\alpha = -109s^3 - 19577s^2 - 7815s - 22883 \tag{4.3}$$

From Equations (2.174) through (2.177) and using the corresponding variables in Table 4, the numerator of pitch attitude to elevator transfer function N_θ is found as;

@ 20 m/s (0.06 Mach)

$$N_\theta = -9056s^2 - 94709s - 33270 \tag{4.4}$$

@ 23.5 m/s (0.07 Mach)

$$N_\theta = -14270s^2 - 173948s - 70182 \tag{4.5}$$

@ 27 m/s (0.08 Mach)

$$N_\theta = -21127s^2 - 294229s - 133504 \tag{4.6}$$

From Equations (2.166) through (2.171) and using the corresponding variables in Table 4, the denominator of longitudinal transfer functions D is found as;

@ 20 m/s (0.06 Mach)

$$D = 68s^4 + 1344s^3 + 7449s^2 + 2635s + 3087 \tag{4.7}$$

@ 23.5 m/s (0.07 Mach)

$$D = 79s^4 + 1829s^3 + 11811s^2 + 4690s + 4906 \tag{4.8}$$

@ 27 m/s (0.08 Mach)

$$D = 90s^4 + 2389s^3 + 17621s^2 + 7749s + 7326 \tag{4.9}$$

Substituting the obtained values of N_α, N_θ, D, and the forward speed into Equation (2.187), the altitude to elevator deflection transfer functions of the UAV at the selected operating points are obtained as;

@ 20 m/s (0.06 Mach)

$$\frac{h(s)}{\delta_e(s)} = \frac{4023s^3 - 44752s^2 - 6085737s - 1551691}{s(68s^4 + 1344s^3 + 7449s^2 + 2635s + 3087)} \tag{4.10}$$

or in normalized forms

$$\frac{h(s)}{\delta_e(s)} = \frac{59.15(s^3 - 11.1s^2 - 1513s - 386)}{s(s^4 + 19.8s^3 + 109s^2 + 38.8s + 45.4)}$$

$$= \frac{-503(-0.0026s^3 + 0.029s^2 + 3.92s + 1)}{s(0.022s^4 + 0.44s^3 + 2.4s^2 + 0.85s + 1)} \tag{4.11}$$

@ 23.5 m/s (0.07 Mach)

$$\frac{h(s)}{\delta_e(s)} = \frac{6438s^3 - 81281s^2 - 13042971s - 4217727}{s(79s^4 + 1829s^3 + 11811s^2 + 4690s + 4906)} \tag{4.12}$$

or in normalized forms

$$\frac{h(s)}{\delta_e(s)} = \frac{81.15(s^3 - 12.6s^2 - 2026s - 655)}{s(s^4 + 23.1s^3 + 149s^2 + 59.1s + 61.8)}$$

$$= \frac{-860(-0.0015s^3 + 0.019s^2 + 3.09s + 1)}{s(0.016s^4 + 0.37s^3 + 2.41s^2 + 0.96s + 1)} \tag{4.13}$$

@ 27 m/s (0.08 Mach)

$$\frac{h(s)}{\delta_e(s)} = \frac{9614s^3 - 136564s^2 - 25230425s - 9744643}{s(90s^4 + 2389s^3 + 17621s^2 + 7749s + 7326)} \tag{4.14}$$

or in normalized forms

$$\frac{h(s)}{\delta_e(s)} = \frac{106.03(s^3 - 14.2s^2 - 2624s - 1013)}{s(s^4 + 26.4s^3 + 194s^2 + 85.5s + 80.8)}$$

$$= \frac{-1329(-0.001s^3 + 0.014s^2 + 2.59s + 1)}{s(0.012s^4 + 0.33s^3 + 2.4s^2 + 1.06s + 1)} \tag{4.15}$$

Note that, the system is fifth order with five open-loop poles and three open-loop zeros considering a proportional control with unity feedback. The open-loop poles, zeros, and gains of the linearized plants as well as the damping ratios and undamped natural frequencies of underdamped open-loop poles at the preset operating points are given in Table 5.

Table 5. Plant properties

	Operating points		
	20 m/s	23.5 m/s	27 m/s
Gain	59.15	81.15	106.03
Velocity Error Coefficient, K_v(m/rad.s)	-503	-860	-1329
Poles	0 $-9.74 \pm 2.92j$ $-0.15 \pm 0.65j$	0 $-11.35 \pm 3.41j$ $-0.17 \pm 0.64j$	0 $-12.97 \pm 3.89j$ $-0.20 \pm 0.63j$
Damping Ratios	0.958 0.220	0.958 0.264	0.958 0.304
Undamped Natural Frequencies (rad/s)	10.2 0.663	11.9 0.663	13.5 0.664
Zeros	44.96 -33.58 -0.26	51.90 -38.95 -0.32	58.98 -44.39 -0.39

77

Since one of the open loop poles is at the origin of the complex s-plane, the type number of the system is 1, therefore one should expect no steady state error (offset) for a step change in the reference input and a finite steady state error (dynamic error) for a ramp change in the reference input.

The remaining four open loop poles are clustered as two pairs of complex conjugate pairs. One pair is located about 65 times farther away from the imaginary axis of the complex s-plane than the other one, indicating that the uncontrolled system has actually a third order dominant dynamics dictated by the pole at the origin and a pair of poles close to the imaginary axis.

Note that as the airspeed increases,
- the velocity error coefficient increases, indicating a better steady state tracking (i.e., smaller dynamic error),
- the open-loop poles far from the origin of the complex s-plane move away from the origin while keeping the damping ratio constant at 0.958, and
- the open-loop poles close to the origin of the complex s-plane move around the origin towards left and towards the real axis (get more damped) while keeping their distance to the origin constant at about 0.663 rad/s.

Before proceeding with a controller design process, it should be mentioned that the negative values for the velocity error coefficient is caused by the sign convention used for the elevator deflection δ_e, as shown in Figure 20. This is a common sign convention used in flight mechanics, which takes the elevator deflection δ_e as positive when the trailing edge is down [22]. However, such a positive elevator deflection causes an increase in tail lift coefficient which creates a loss in total pitching moment. This negative pitching moment tends to pitch the nose downward and air vehicle starts to descend [17]. Therefore, a positive elevator deflection is required when a decrease in the air vehicle's flight altitude is desired. A sign reversal in the transfer functions is needed to make a positive altitude change correspond to a positive elevator deflection; hence, all transfer functions

given earlier are used with a reversed sign from hereafter in order to comply with the standard convention used in negative feedback systems.
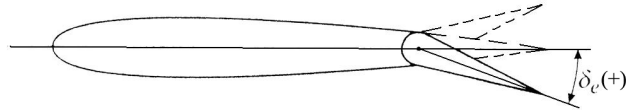

Figure 20. Sign convention for elevator deflection

4.2 CONTROLLER DESIGN

In a classical controller design for linear systems, the major design goals can be listed as follows.

- A stable operation (all closed-loop poles lying at the left hand s-plane)
- A satisfactory steady-state performance (an appropriate type number with a large enough error coefficient)
- Satisfactory transient properties (fast response - small rise and settling times; small overshoot for a step input; no or acceptably small oscillations)

Since the controller design process is essentially the same for all three linearized plants, it is presented here for only one of them; namely, the plant at the horizontal speed of 23.5 m/s. The software program MATLAB$^®$ is used to simulate the step responses of the controlled system.

In order to explore the behavior of the closed loop altitude hold mode autopilot system with a Proportional Controller (P-Controller) of gain K, its root locus plot drawn in MATLAB$^®$ is given in Figure 21 and its magnified version is given in Figure 22.
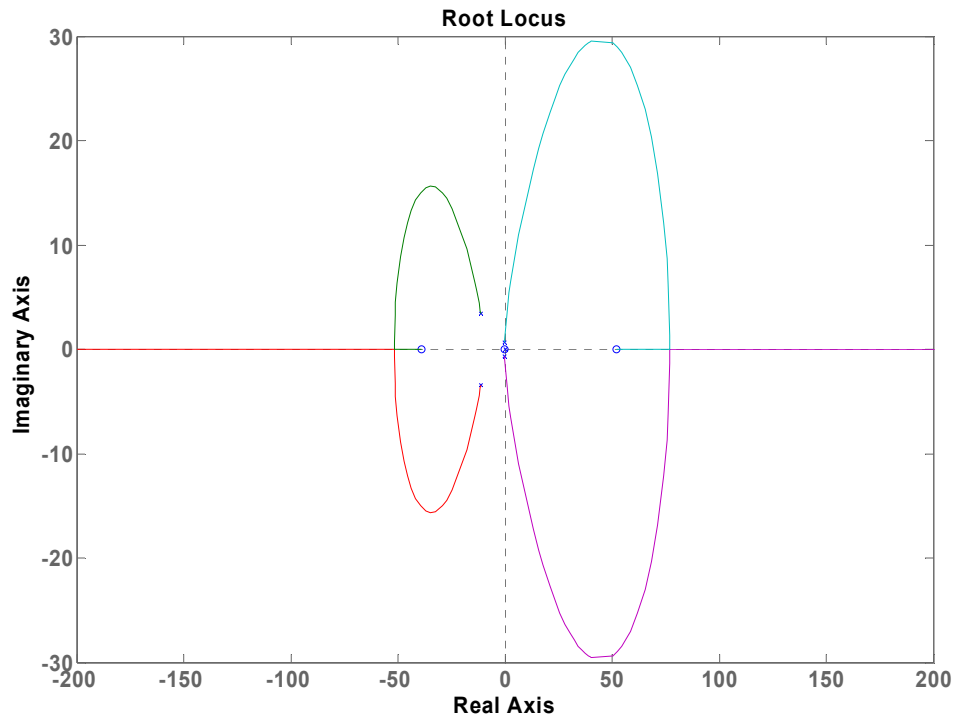
79

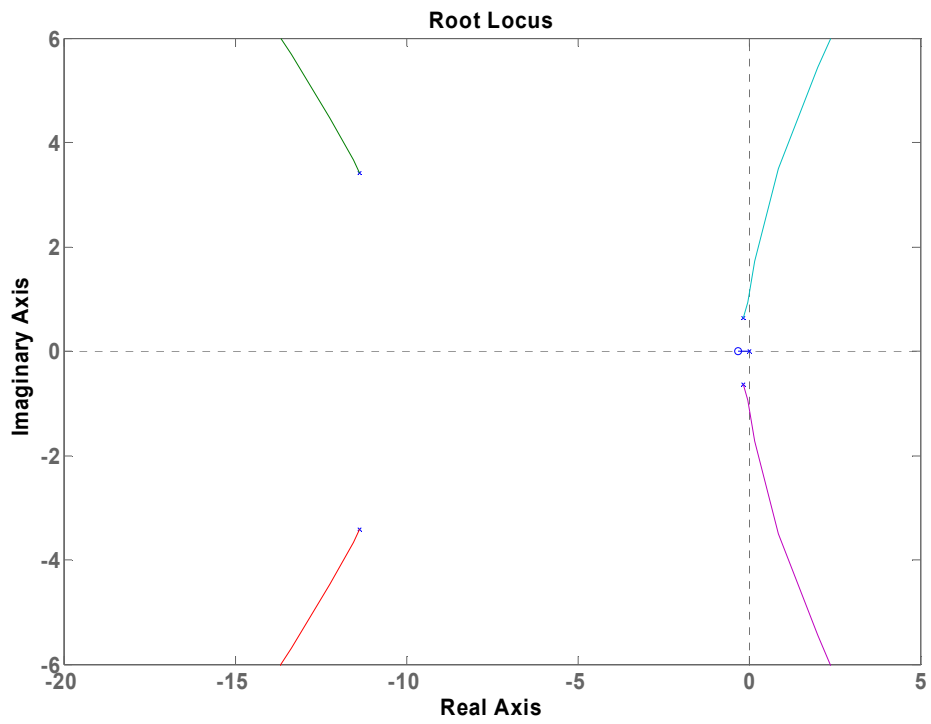**Figure 21. Root locus of the system**

Figure 22. Root locus of the system (magnified)

80

These root loci reveal that the system is stable for low K values and it becomes unstable after a certain K value. The comparisons of plant properties, root loci, and this stability characteristic of the air vehicle used in the study with those for a similar full scale Cessna 182 airplane presented in Appendix C show a good degree of similarity as it could be predicted intuitively.

There exist five branches of the root loci, each starts from one of the open-loop poles located at $p_{1,2}$=-11.35 ± 3.41j, $p_{3,4}$=-0.17 ± 0.64j, and p_5=0; three of which terminate at three finite open-loop zeros located at z_1=51.90, z_2=-38.95, z_3=-0.32, and the rest two at infinity. Note that the terminations of two branches at infinity are not along vertical directions as expected from a regular root locus for a fifth order open-loop system with three finite zeros, but rather along positive and negative directions of the real axis. This behavior resembling a complementary root locus drawn for negative K values is due to the sign reversals of transfer functions for assuring the compatibility between positive aircraft's altitude changes and positive elevator deflections.

The SISO Design Tool of MATLAB® Simulink® is used to determine the conditions on K for the system to be stable. The analysis results showed that, K should be in the range 0<K<0.0024 for stability.

In order to obtain a stable step response of the system with a minimum settling time while keeping the overshoot smallest, the Simulink Response Optimization blockset [23] is used. This blockset is explained in detail later in this chapter. Simulation results show that K=0.00089 rad/m (0.05 deg/m) provides the minimum settling time (5 %) in the response. The corresponding closed-loop poles of the system are located at $p_{1,2}$=-11.4 ± 3.44j, $p_{3,4}$=-0.08 ± 0.84j, and p_5=-0.143. The damping ratio and undamped natural frequencies of these poles are given in Table 6. Furthermore, the response of the system to a unit step input for K=0.00089 rad/m is plotted in Figure 23.

Table 6. Closed-loop pole characteristics of the system for K=0.00089

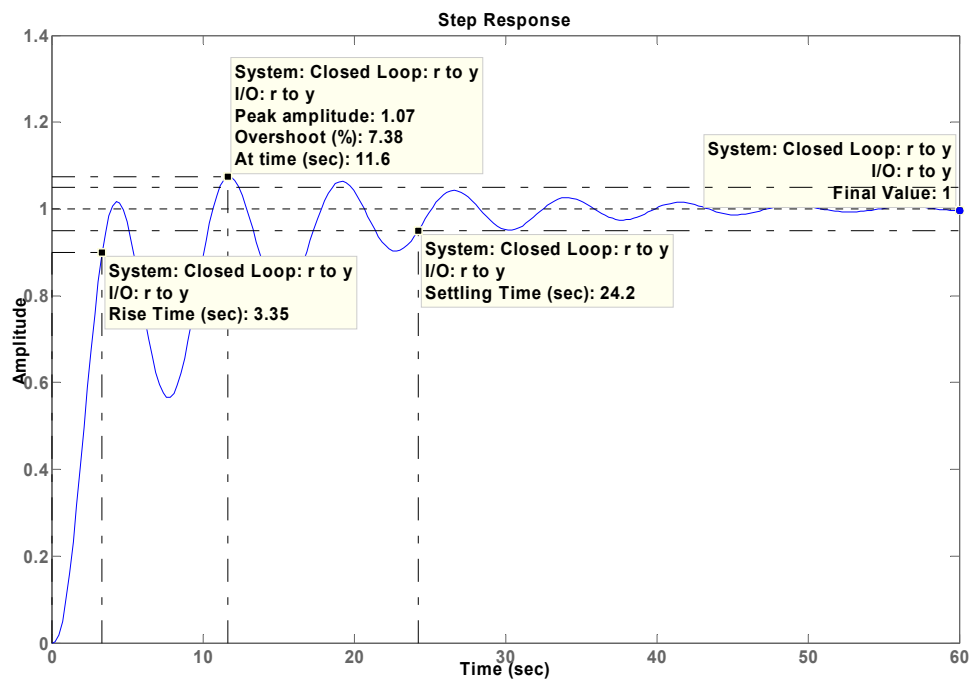| Closed-Loop Pole	Damping Ratio	Undamped Natural Frequency (rad/s)
-0.143	1	0.143
$-11.4 \pm 3.44j$	0.957	11.9
$-0.08 \pm 0.84j$	0.094	0.844

Figure 23. Unit step response of the system for K=0.00089

Even though the overshoot and rise time of the response for a step input is small (7.4 % and 3.4 s respectively), it is observed from Figure 23 that the settling time (5 %) of the response is 24.2 seconds, hence, the speed of the response is relatively slow.

Therefore, it is observed that the adjustment of the controller gain alone (P controller) is not sufficient for the alteration of the system behavior. It is now necessary to redesign the system to alter the overall behavior so that the speed of

the system response is as fast as desired. This can simply be achieved by adding an Integral Control action to the Proportional Control action. However, this addition will affect the stability feature of the system in an adverse manner; hence, one needs to add some Derivative action, too, to further stabilize the system. Therefore, in order to speed up the response and to increase the stability of the system at the same time, the use of a PID controller is decided. It is known that PID controllers are widely used in UAV control processes because of their simple structure and robust performance in a wide range of operating conditions [3], [7].

Furthermore, due to the facts explained before, a gain scheduling is applied in the controller design procedure. Therefore, an overall design procedure followed in this study for a system controller can be given as follows.

- Selection of the scheduling variable and setting the operating points
- Designing a PID controller at each operating point to meet the described design goals
- Design of the scheduler

The scheduling variable and the operating points are already covered in Section 4.1 for the linearization of the plant.

Prior to the controller design, the transient response characteristics of the altitude hold autopilot system with a PID controller should be defined clearly. Due to the actuator nonlinearities, the controller is desired to be designed at a high input signal. This approach is applicable since the same controller will make the system response even better for inputs of smaller size. Considering the fact that the altitude hold autopilot is engaged somewhere near the desired flight altitude, the parameters of the PID controller are tuned for a step input of 15 m. To avoid any sudden and/or fast altitude corrections, the rise time of the response is set as large as 5 seconds. The settling time (5 %) is set to 8 seconds in accordance. In addition to these, the position/altitude update rate (1 Hz) of the system may cause some

83

oscillations in the system response due to lack of continuous altitude input. This undesired response can be prevented by designing the system with a small overshoot value. Hence, the maximum percent overshoot is set as 5 %.

For the design purposes of the PID controller at each operating point, the Simulink Response Optimization blockset is used. This blockset provides a graphical user interface to assist controller design in the time domain. With this blockset, controller parameters can be tuned within a nonlinear Simulink model to meet the time domain performance requirements. These performance requirements are defined either by graphically placing constraints within a time domain window or by defining a reference signal to be tracked.

To use the Simulink Response Optimization, the Signal Constraint block is connected to the plant in order to place constraints to its output signal in the Simulink model. The usage of the Signal Constraint block is shown in Figure 24. Simulink Response Optimization converts the time domain constraints into a constrained optimization problem and solves the problem using the optimization routines taken from the Optimization Toolbox [23]. Parameters are iteratively changed and the simulation results are compared with each other to better meet the constraint objectives.
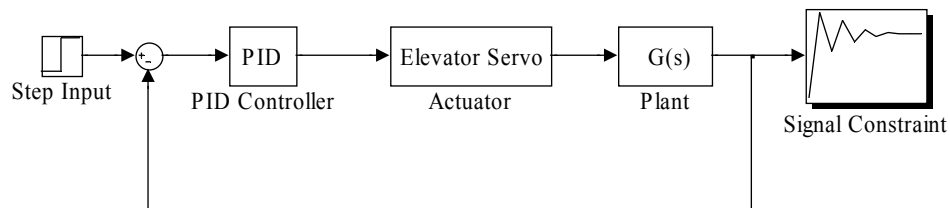

Figure 24. Controller design using Simulink Response Optimization

The gain parameters of the PID controller are defined as the tunable parameters and initialized in the MATLAB® workspace. The initial values for the gain parameters are all taken as zero.

To adjust the constraints on the signal, the response characteristics to a step input are defined in the Signal Constraint block. Step input parameters (step time, final time, initial output, and final output) and transient response characteristics (settling time, rise time, percent settling, percent rise, percent overshoot, and percent undershoot) are the required variables to place the constraints.

As defined earlier, the desired transient response characteristics of the control system for a step input of 15 m are given below. This step input value is equivalent to engaging the altitude hold mode with an error of 15 m between the reference and actual altitudes.

Input initial value = 0   Input final value = 15   Step time = 0

Rise time = 5 s   Percent rise = 90 %   Settling time = 8 s

Percent settling = 5 %   Percent overshoot = 5 %   Percent undershoot=1%

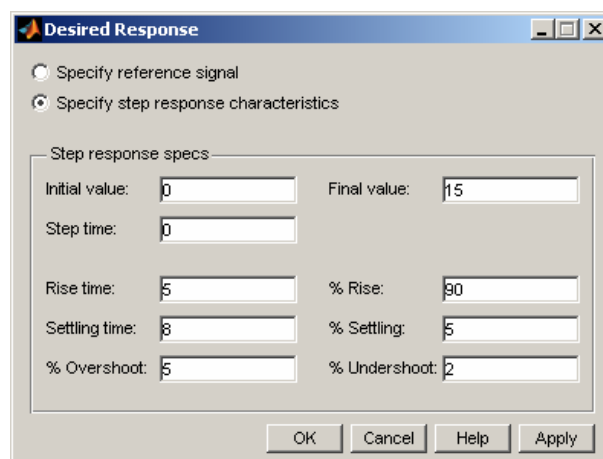The Signal Constraint block window showing these constraint parameters is shown in Figure 25.

Figure 25. Transient response constraints

By setting the constraints on the signal, the response is forced to lay within the constraint bound segments. However, this does not exactly define the response behavior within the constraints. To better shape the signal response, the desired response of the signal is plotted in the signal constraint window and the actual response is forced to track this reference signal. Both the signal constraints and the reference signal are shown in Figure 26.
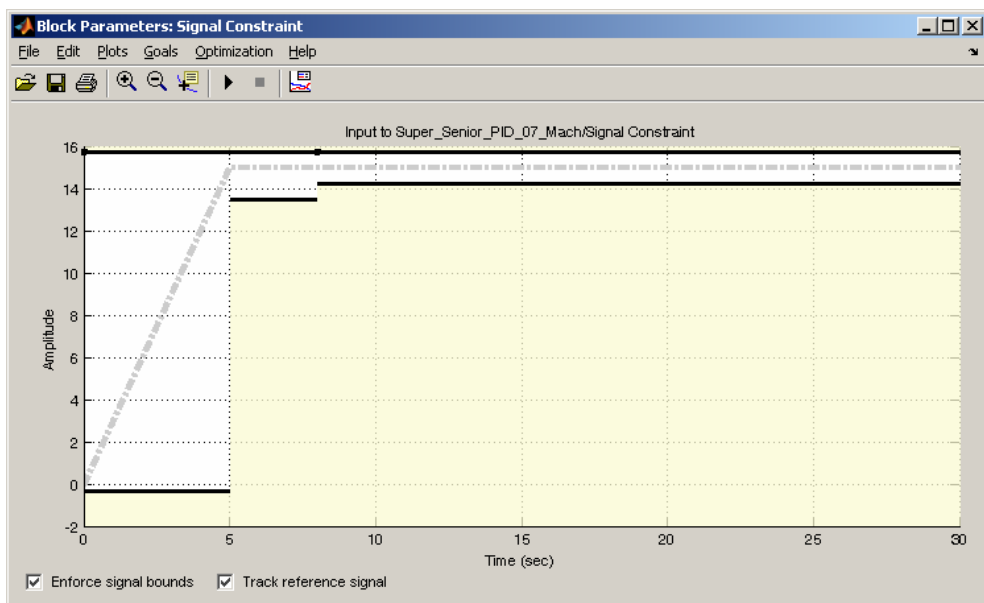

Figure 26. Graphical constraints and the reference signal

After setting the signal characteristics and running the optimization, Simulink Response Optimization blockset performs consecutive iterations and tunes the gain parameters to meet the performance requirements. Signal response at each iteration can be seen in Figure 27.
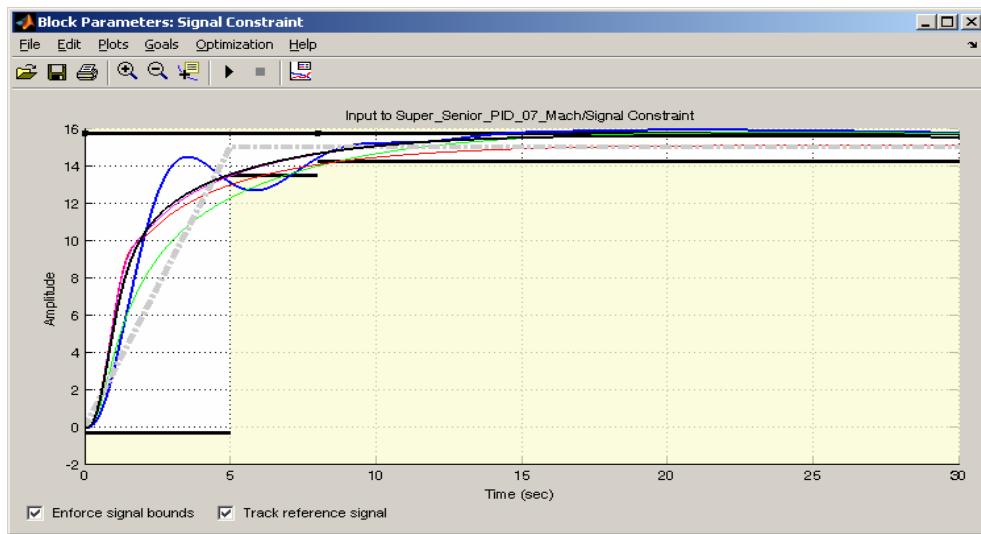
Figure 27. Signal responses at each iteration

Final response of the signal is given in Figure 28 for the PID controlled linearized plant at 23.5 m/s.
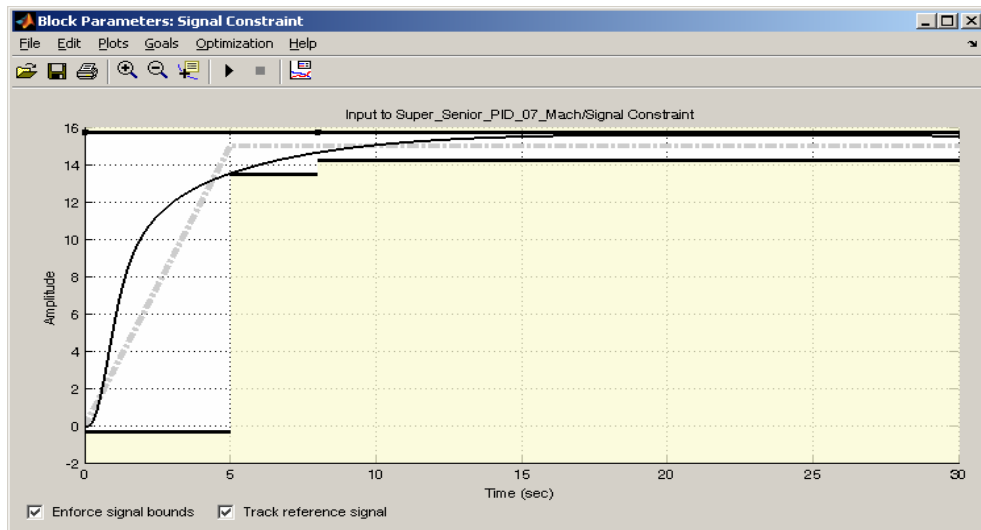

Figure 28. Output signal response

The gain parameters of the PID controllers for three linearized plants are obtained after running the optimization under the same constraints. These gains are given in Table 7 and plotted in Figure 29.

Table 7. PID controller gains

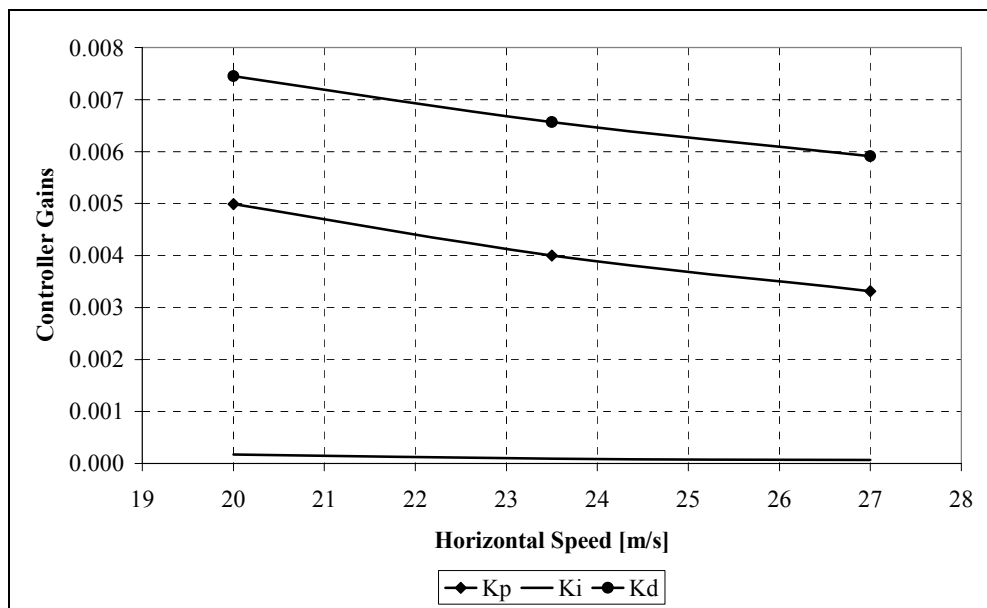| Controller gain	Operating point		
	20 m/s	23,5 m/s	27 m/s
K_p (rad/m)	5×10^{-3}	4×10^{-3}	3.3×10^{-3}
K_i (rad/m.s)	1.75×10^{-4}	9.5×10^{-5}	6.7×10^{-5}
K_d (rad.s/m)	7.4×10^{-3}	6.6×10^{-3}	5.9×10^{-3}

Figure 29. Variation of PID gains with horizontal speed [m/s]

The closed-loop poles of the system with the PID controller are given in Table 8 at three distinct operating points. The root locus of the system at the horizontal speed of 23.5 m/s is also shown in Figure 30.

Table 8. Closed-loop pole characteristics of the system with PID controller

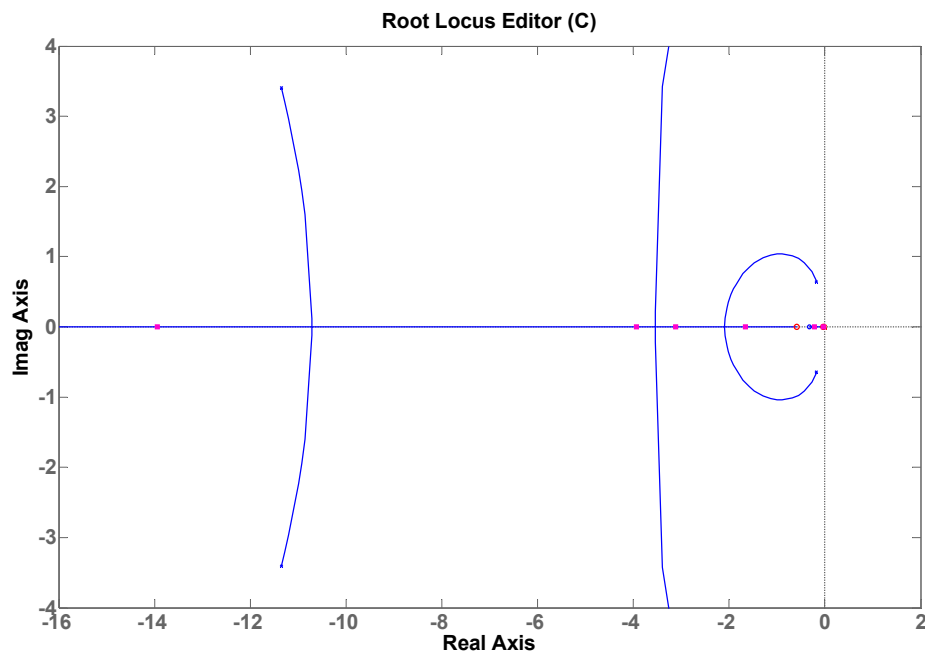|	Operating points		
	20 m/s	23.5 m/s	27 m/s
Closed-Loop Poles	-11.9 -4.48 -0.037 -0.164 $-1.53 \pm 1.09j$	-13.9 -3.94 -3.12 -1.65 -0.213 -0.0264	-16 -1.18 -0.252 -0.0209 $-4.34 \pm 1.67j$

Figure 30. Root-locus of the system with PID controller

As the controller gains at three different operating points are found, the benefits of gain scheduling technique can be investigated and the performance of a controller designed at another operating point can be observed hereafter.

For this purpose, the PID controller gains tuned at the operating points of 20 m/s and 27 m/s are used for the linearized plant at the operating point of 27 m/s. The response of the system for a step input of 15 m is plotted and given in Figure 31.

Furthermore, the reverse application is also simulated for the linearized plant at the operating point 20 m/s. In this case, the PID controller gains tuned at the operating points of 20 m/s and 27 m/s are used for the linearized plant at the operating point of 20 m/s. The response of the system for a step input of 15 m is plotted and given in Figure 32.
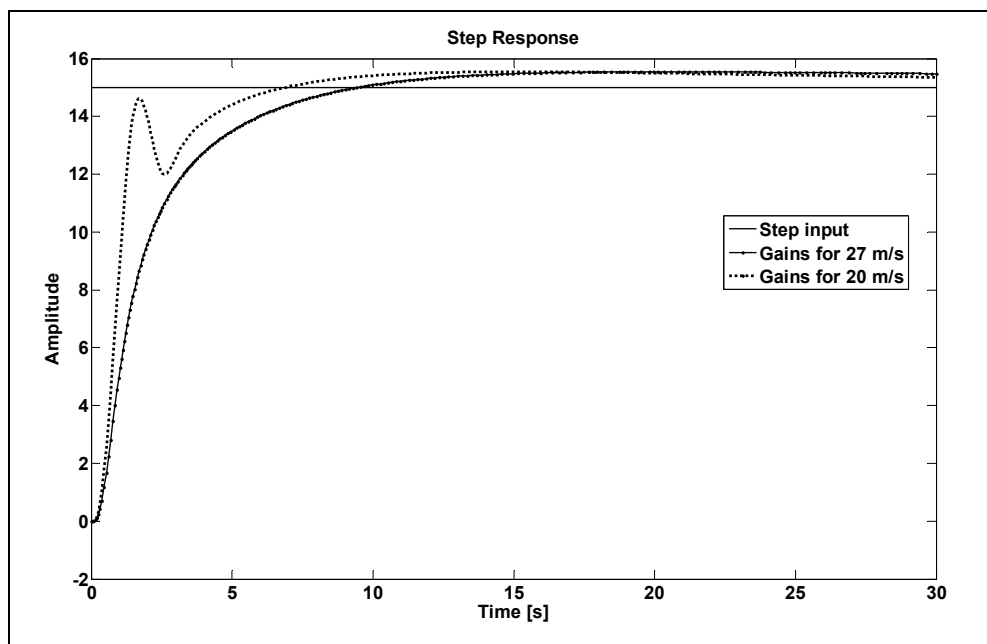

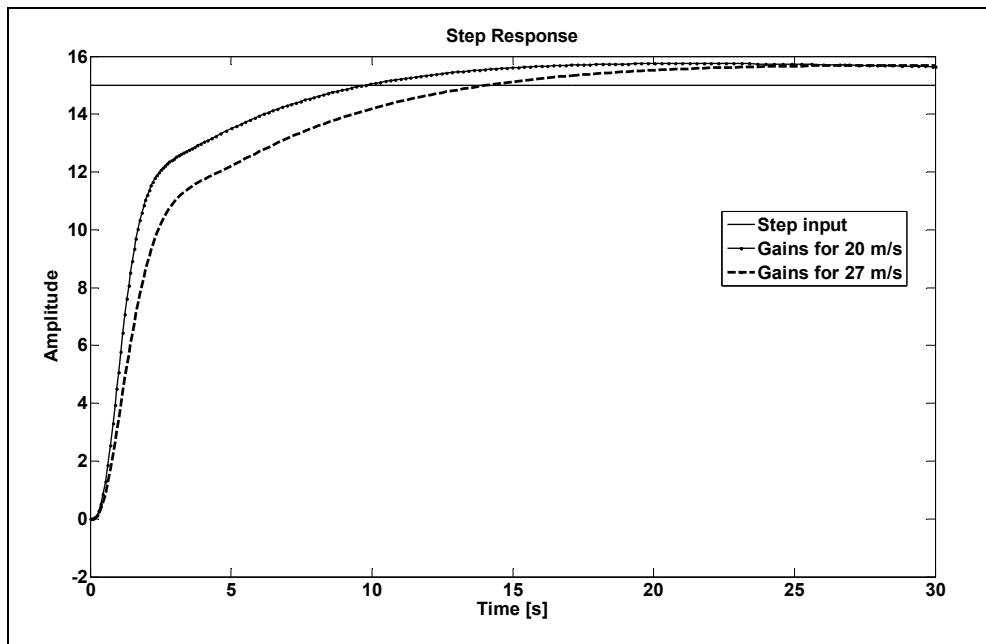**Figure 31. Response of the linearized plant at 27 m/s**

90

Figure 32. Response of the linearized plant at 20 m/s

As it can be seen from the system responses, using the controller gain values of another linearized plant degrades the performance of the controller and produces a worse response (oscillations and/or slower response). This fact reveals that by using gain scheduling technique in this application, a better performance is obtained over the entire speed envelope of the UAV.

4.3 CONCLUDING REMARKS

In this chapter, the altitude hold mode autopilot used in this application is explained. Then, the type of the controller is determined and a gain scheduling technique is applied in the design of the controller to achieve better performance compared with a single controller. The operating points are set and the longitudinal transfer functions of the UAV relating the altitude to elevator deflection are established at these points. After defining the requirements to achieve an

acceptable response, the gains of the controller are tuned by using the Simulink Response Optimization Toolbox of MATLAB® Simulink®. Finally, the benefits achieved by applying gain scheduling technique in this study are demonstrated via simulations. As the controller system is designed in this chapter, the next task is the verification this design by flight tests.

CHAPTER 5

HARDWARE IMPLEMENTATION

In this chapter, the hardware installed on the UAV and the hardware used on the ground are presented. As seen from the general hardware architecture of the system in Figure 33, the equipment used in this thesis study can be grouped in two separate sets; the "equipment implemented and used onboard the UAV" and the "equipment located on the ground station".
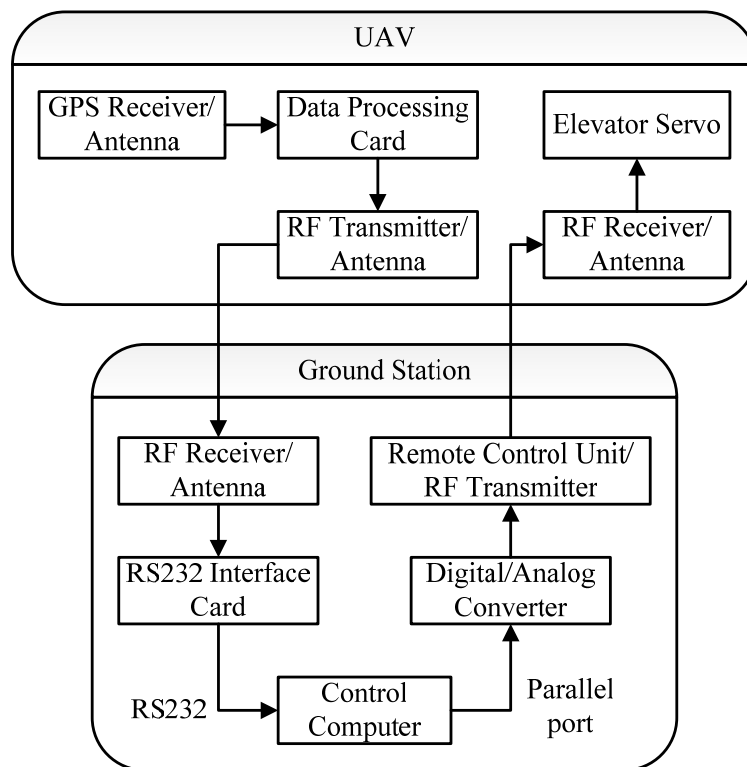
Figure 33. Schematic representation of the UAV platform

5.1 UAV EQUIPMENT

The main purpose of the equipment on the UAV is to determine its exact location (longitude, latitude, and altitude), to process and transmit this information, along with several helpful data, to the ground unit. To accomplish this, a system consisting of a GPS receiver, a GPS antenna, a data processing card, an RF transmitter & antenna, and a battery are installed on the RC airplane. A picture showing the equipment implemented on the RC airplane is given in Figure 34.
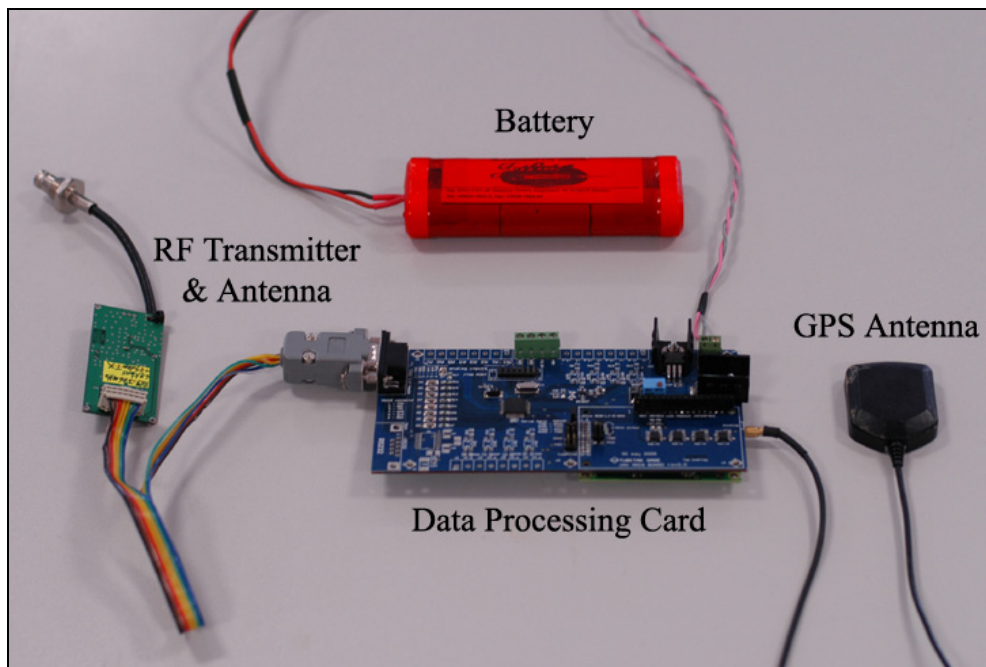
Figure 34. Equipment implemented on the RC airplane

5.1.1 GPS RECEIVER

An RCB-LJ type GPS receiver board [24] from U-BLOX is selected and used for the study. The RCB-LJ is an ultra-low power GPS receiver board. It fulfills the

requirements for cost efficiency, speed and straightforward plug-in system integration.
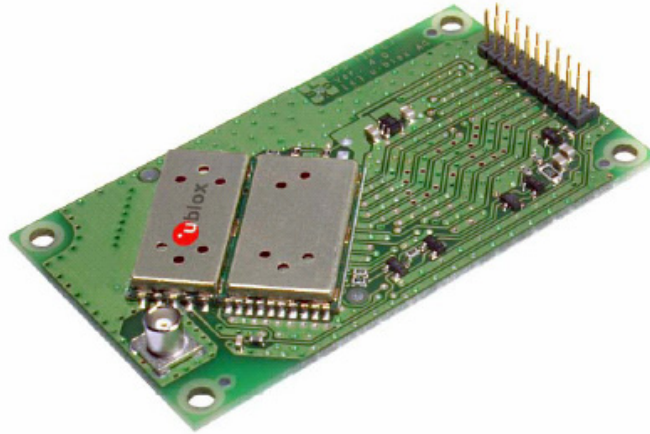
Figure 35. RCB-LJ GPS receiver board [24]

Its positioning engine provides an excellent navigation accuracy and dynamic performance even in areas with limited sky view. It can operate even at low signal levels without loss in accuracy. Some general benefits of this receiver board are [24];

- High acquisition and tracking sensitivity
- Ultra-low power consumption
- Excellent GPS performance
- Active antenna support

The technical and mechanical specifications of the RCB-LJ GPS receiver board are given in Table 9 [24].

Table 9. Specifications of the RCB-LJ GPS receiver board

Receiver type	16 channel
Maximum update rate	4 Hz
Accuracy	Position 2.5 m CEP / 5.0 m SEP
Start-up times	Hot start <3.5 s Cold start 34 s
Signal reacquisition	<1 s
Dynamics	≤ 4 g
Power supply	3.15 - 5.25 V
Power consumption	175 mW @ 3.3 V 265 mW @ 5.0 V
Operating temperature	-40°C - 85°C
Size	71 x 41 x 11 mm
Mass	17 grams

In Table 9, CEP (circular error probability) is the radius of a horizontal circle centered at the antenna's true position containing 50 % of the fixes, and SEP (spherical error probability) is the radius of the sphere centered at the true position containing 50 % of the fixes.

The RCB-LJ receiver board can support up to 4 Hz position update rate. However, a position update at 1 Hz is considered to be appropriate in this study due to fact that the cruise speed of our flying platform is relatively low (~30 m/s). Furthermore, the use of higher update rates increases the load on the RF communication module which is not preferred at this stage of the study and left as an improvement in future works.

The acquired GPS data is in United States National Marine Electronics Association (NMEA) format. The NMEA is a special data format which is

standardized by the National Marine Electronics Association to ensure that the relayed GPS data is portable. Seven data sets/sentences are widely used with GPS modules to relay GPS information. Descriptions of these data sets are given in Table 10 [25].

Table 10. NMEA data set descriptions

Data set	Description
GPRMC	Information on time, latitude, longitude, height, system status, speed, course, and date
GPVTG	Information on course and speed
GPGGA	Information on time, latitude, longitude, quality of the system, number of satellites used, and the height
GPGSA	Information on the measuring mode (2D or 3D), number of satellites used to determine the position, and the accuracy of the measurements (DOP: Dilution of Precision)
GPGSV	Information on the number of satellites in view, their identification, their elevation and azimuth, and the signal-to-noise ratio
GPGLL	Information on latitude, longitude, time, and health
GPZDA	Information on UTC time, date, and local time

Following is a sample NMEA output message taken on 10th February 2005 at METU campus.

$GPRMC,130751.00,A,3953.33701,N,03246.79232,E,0.005,156.17,100205,A*6C
$GPVTG,156.17,T,,M,0.005,N,0.009,K,A*35
$GPGGA,130751.00,3953.33701,N,03246.79232,E,1,5,1.98,942.2,M,38.7,M,,*6D
$GPGSA,A,3,03,16,22,18,21,,,,,,,,3.37,1.98,2.73*0D

$GPGSV,2,1,07,03,56,303,33,16,31,220,36,14,,,35,22,81,169,50*4C

$GPGSV,2,2,07,18,60,054,44,21,34,071,40,15,,,43*75

$GPGLL,3953.33701,N,03246.79232,E,130751.00,A,A*6C

$GPZDA,130751.00,10,02,2005,00,00*63

Three of these sample data sets given above (GPVTG, GPGGA, and GPGSA) are described in Table 11 through Table 13 respectively [25].

Table 11. Description of sample data set GPVTG

Field	Description
156.17	Course: 156.17° (T) with regard to the horizontal plane
T	Angular course data relative to the map
,,	Course (M) with regard to the horizontal plane
M	Angular course data relative to magnetic north
0.005	Horizontal speed (N)
N	Speed in knots
0.009	Horizontal speed (km/h)
K	Speed in km/h
A	-
*	Separator for the checksum
35	Checksum for verifying the entire data set

Table 12. Description of sample data set GPGGA

Field	Description
130751.00	UTC positional time: 13h 07m 51.0 s
3953.33701	Latitude: 39° 53.33701 m
N	North (N=north, S=south)
03246.79232	Longitude: 32° 46.79232 m

Table 12. Description of sample data set GPGGA (continued)

Field	Description
E	East (E=east, W=west)
1	GPS quality details (0=no GPS, 1=GPS, 2=DGPS)
5	Number of satellites used in calculation
1.98	Horizontal Dilution of Precision (HDOP)
942.2	Geoid height
M	Unit of height (M=meter)
38.7	Height differential between an ellipsoid and geoid
M	Unit of height (M=meter)
,,	Age of the DGPS data (in this case no DGPS is used)
*	Separator for the checksum
6D	Checksum for verifying the entire data set

Table 13. Description of sample data set GPGSA

Field	Description
A	Calculating mode (A=automatic selection between 2D/3D mode, M=manual selection between 2D/3D mode)
3	Calculating mode (1=none, 2=2D, 3=3D)
03	ID number of the satellites used to calculate position
16	ID number of the satellites used to calculate position
22	ID number of the satellites used to calculate position
18	ID number of the satellites used to calculate position
21	ID number of the satellites used to calculate position
,,,,,,,,	Dummy for additional ID numbers(currently not used)

Table 13. Description of sample data set GPGSA (continued)

Field	Description
3.37	Position Dilution of Precision (PDOP)
1.98	Horizontal Dilution of Precision (HDOP)
2.73	Vertical Dilution of Precision (VDOP)
*	Separator for the checksum
0D	Checksum for verifying the entire data set

In order to understand PDOP, HDOP and VDOP parameters in Table 13, the definition of DOP is needed. The accuracy of the position obtained by a GPS depends on the pseudo-range (incorrect distance of the satellite from the GPS receiver due to the unsynchronized receiver clock) measurements and the geometrical configuration of the satellites used in the position calculation [25]. This effect is expressed by the dilution of precision value. Hence, PDOP is the positional DOP (position in 3D), HDOP is the horizontal DOP (position on a plane), and VDOP is the vertical DOP (position on a vertical plane, height). These parameters are useful in analyzing the accuracy of the measurements.

5.1.2 GPS ANTENNA

The ANN type active GPS antenna [26] from U-BLOX is selected and used for the study. It is an easy to use, compact size, and high performance active antenna with integrated low-noise amplifier and it is ideal for U-BLOX GPS receivers.

Figure 36. ANN active GPS antenna [26]

General specifications of the ANN active GPS antenna are given in Table 14 [26].

Table 14. Specifications of the ANN active GPS antenna [26]

DC voltage	3 - 5 V
DC current	Max. 22 mA
Operating temperature	-40°C - 85°C
Size	48 x 40 x 13 mm
Mass	≤ 105 grams
Cable	5m coaxial cable
Mounting	Magnetic base

5.1.3 DATA PROCESSING CARD

The exact location (longitude, latitude, and altitude) of the airplane acquired by the GPS receiver is processed and sent to RF transmitter by the data processing card

which is designed at TÜBİTAK-SAGE. A Texas Instruments processor MSP430F149 is used as the microcontroller in the data processing card. The processor receives the GPS data as NMEA sentences and sends it to the RF transmitter as serial data packets at 1 Hz. The processor has two Universal Asynchronous Receiver/Transmitter (UART) communications which is advantageous for GPS data and RF communications. It has a 16 bit structure and works at 8 MHz.
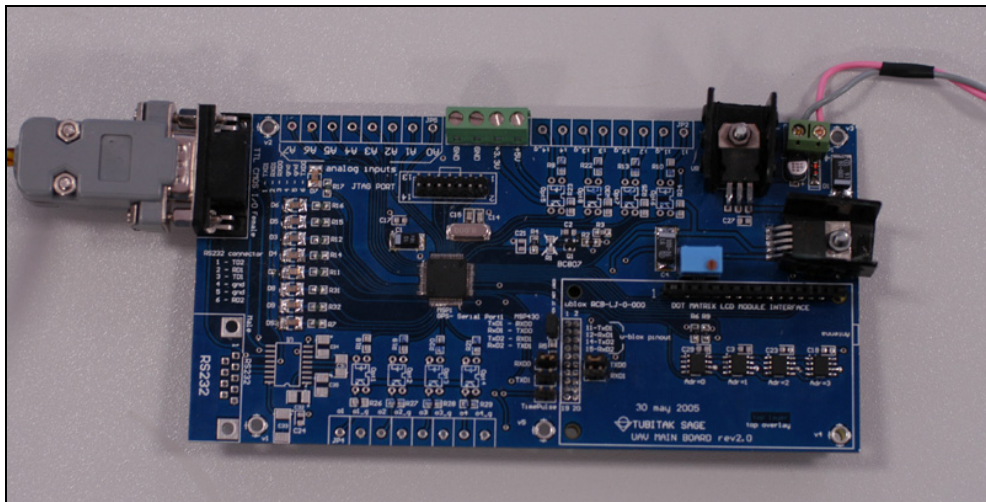

Figure 37. Data processing card

5.1.4 RF TRANSMITTER AND ANTENNA

The RF transmitter sends the GPS data to the RF receiver on the ground station which can be located at a maximum distance of 3 km away from the transmitter. The RF transmitter and its antenna which are shown in Figure 38 are particularly designed and produced for this thesis study by UDEA Electronics. The output power of the transmitter is 500 mW and its working frequency is 866 MHz.
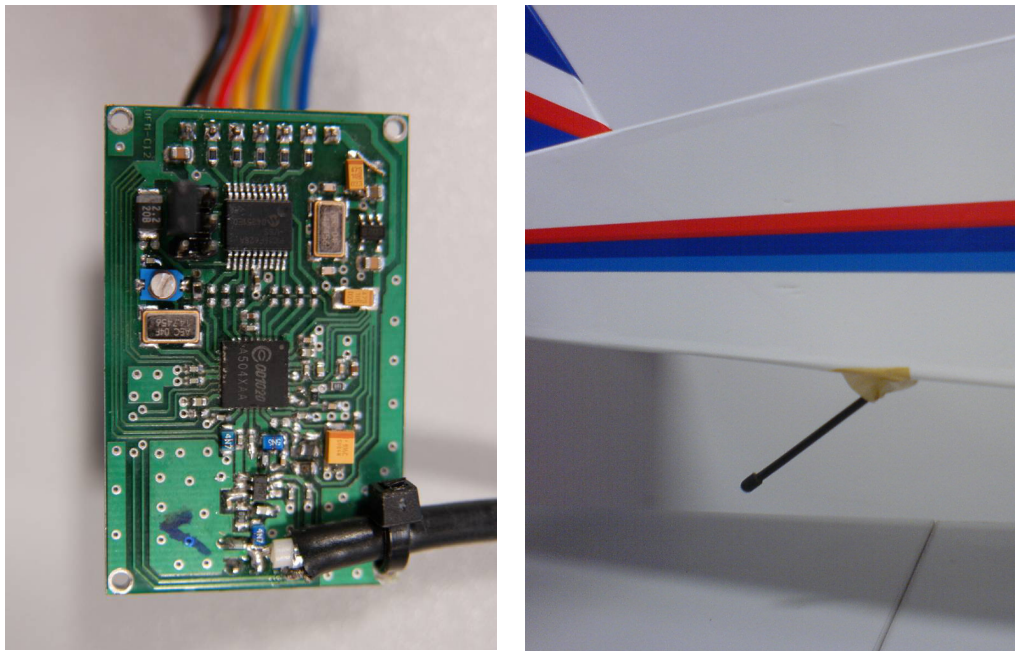
Figure 38. RF transmitter and antenna

5.2 GROUND STATION EQUIPMENT

The equipment located on the ground are used for receiving the information sent by the RC airplane, processing this information, generating, and sending the necessary control commands to the RC airplane. The ground unit consists of the following equipment; an RF receiver & antenna, an RS232 interface card, a control computer, a Digital Analog Converter (DAC), an RC airplane remote control unit, and a battery (same as the one used on the UAV). This configuration is shown in Figure 39.
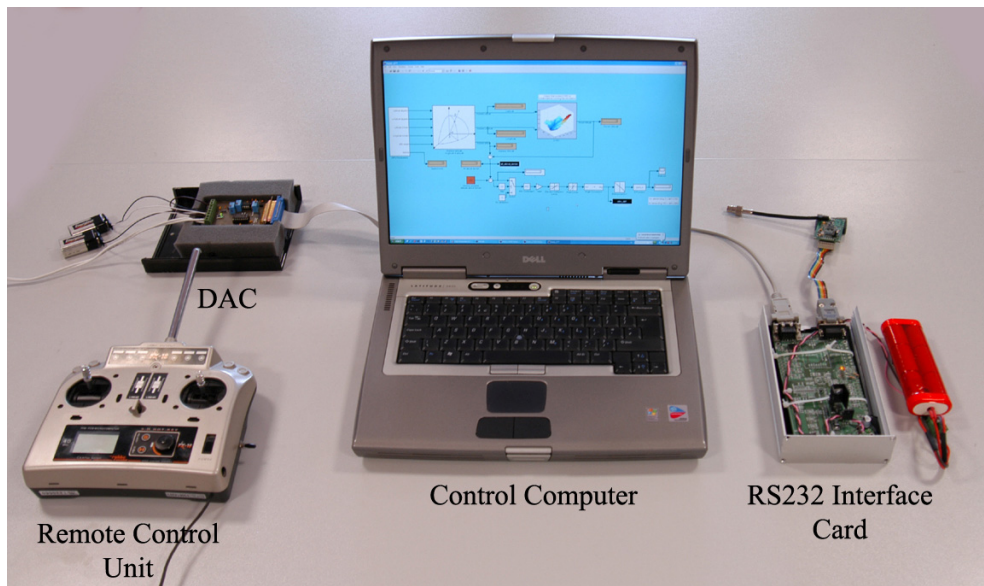
Figure 39. Ground station

5.2.1 RF RECEIVER AND ANTENNA

The RF receiver receives the GPS data from the RC airplane sent by the onboard RF transmitter. The receiver, shown in Figure 40, has the same producer and characteristics with the transmitter given in Section 5.1.4. It is connected to the RS232 interface card through UART.
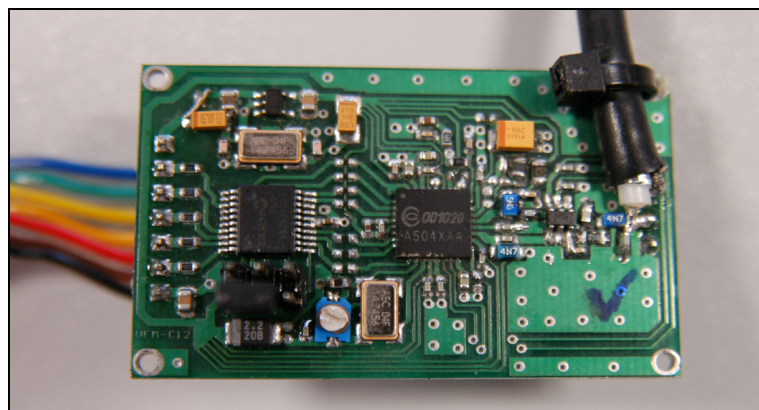

Figure 40. RF receiver

104

5.2.2 RS232 INTERFACE CARD

The GPS data acquired by the RF receiver is processed and fed to the computer by the RS232 interface card which is connected to the control computer via its RS232 serial port. The card is designed at TÜBİTAK-SAGE, and the processor used in the card is the same with the one used in the data processing card.
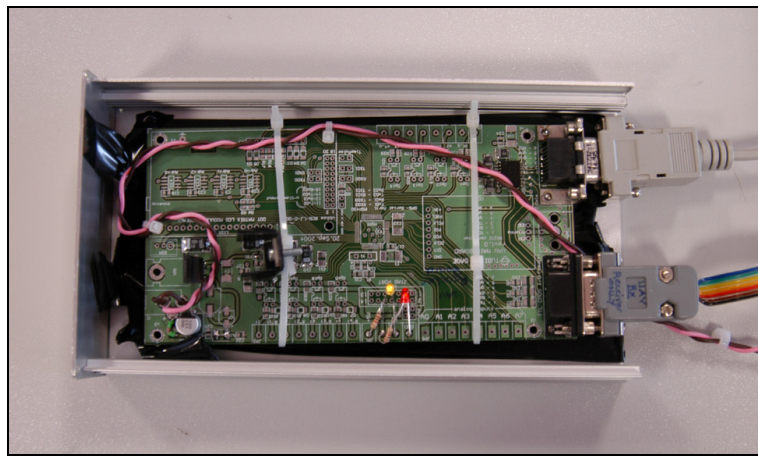
Figure 41. RS232 interface card

5.2.3 CONTROL COMPUTER

The control computer works in MATLAB® Simulink® environment. The GPS data received via the RS232 serial port of the computer is processed by using MATLAB® libraries. Knowing the location (longitude and latitude) of the airplane; the corresponding terrain elevation with respect to the mean sea level is obtained from the DTED of the flight region which is stored as a look-up table in MATLAB® Simulink®. According to the desired flight AGL altitude of the RC airplane, the control variable (elevator deflection angle) is generated by the controller and sent to the DAC via the parallel port of the computer as a digital value.

5.2.4 DIGITAL ANALOG CONVERTER

The digital analog converter, shown in Figure 42, is used to convert the digital information from the computer to an analog information (voltage). It is connected to the control computer via its parallel port and to the remote control unit of the RC airplane via the potentiometer which controls the elevator deflection angle. The DAC has an 8-bit structure. Since the original potentiometer works within 0-5 Volt range, the DAC is designed such that the digital value of 0 corresponds to 0 Volt and the digital value of 255 corresponds to 5 Volts. Two 9 Volt batteries are used to supply power to the DAC.
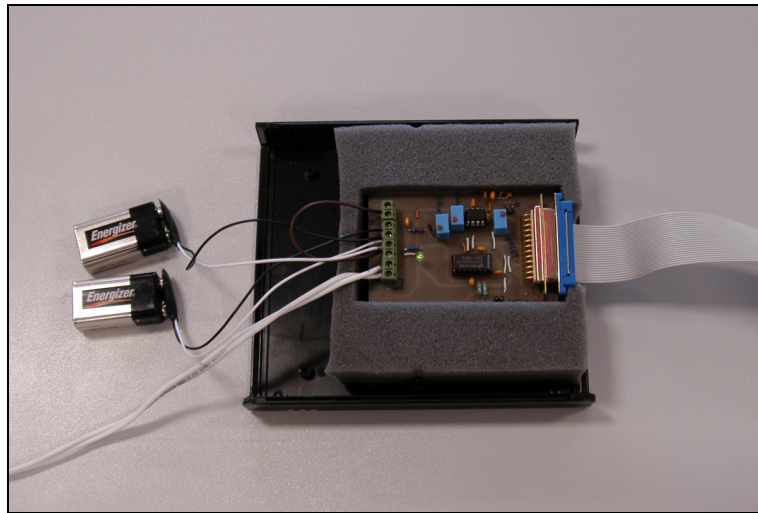

Figure 42. Digital analog converter

5.2.5 RC AIRPLANE REMOTE CONTROL UNIT

In accordance with the operational concepts, all takeoff / landing scenarios and the lateral motion of the RC airplane are controlled manually by the remote control unit of the airplane. Whereas, the longitudinal motion can be controlled either by

the user (manually) or by the control computer via the controller (automatically). This optional control is provided by changing the input of the potentiometer of the remote control unit, which controls the elevator deflection, with a switch that enables either the manual control or automatic control. This configuration has the advantage of increasing the safety of flight tests where a human pilot can obtain control authority immediately after an emergency situation occurs. The controller generates the control input continuously even in manual flight and as soon as the automatic flight mode is turned on. The generated deflections are sent to the elevator servo of the RC airplane. The working frequency of the remote control unit is 40.665 MHz. The remote control unit and the implemented switch are shown in Figure 43.
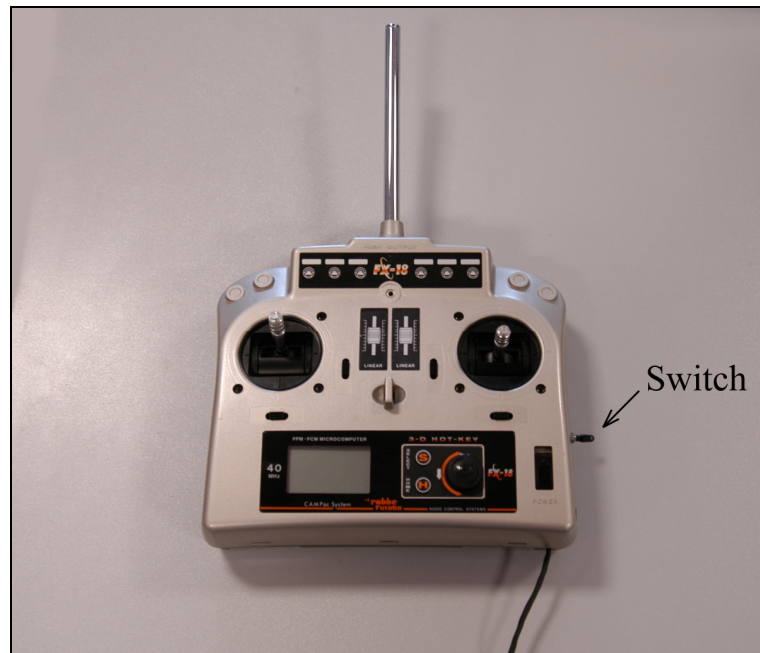
Figure 43. RC airplane remote control unit

5.3 CONCLUDING REMARKS

The complementary equipment for the UAV platform other than the airframe (presented in Chapter 3) are given in this chapter. Test platform is investigated under two separate groups which are the UAV and its ground station. The main equipment on the flying platform and the ground station are defined in details. Their usage purposes and technical specifications are also presented.

CHAPTER 6

FLIGHT TESTS

The final objective of this thesis study is to design and flight test a prototype autopilot platform for controlling the longitudinal motion of an UAV. In this chapter, the results of the flight tests performed with the developed platform and the designed controller are presented.

The main purpose of this study is to fly the UAV at a desired altitude above the terrain within a band using the autopilot platform developed. However, before flight testing the UAV directly at this autopilot mode (in which the reference input is varying as the terrain altitude is also varying during flight), it is desired to flight test it with a constant reference input to see how developed system acts under this condition. Hence, two autopilot modes are used and tested in this study. One is the mean sea level (MSL) altitude hold mode, whereas the other is the above ground level (AGL) altitude hold mode.

In order to ensure a longitudinal motion, the flight path (in the horizontal plane) of the UAV is tried to be kept as linear as possible during the tests. To provide this, the UAV is trimmed manually after its takeoff to avoid any rolling or yawing motion in its uncontrolled flight. However, due to weather conditions such as wind and thermal effects, some oscillations are observed deviating from linear flight conditions in some of the tests. These undesired disturbances also seem to affect the pitching motion of the UAV during the flight tests.

The position, altitude, and accuracy prediction data acquired from the GPS receiver together with the elevator deflections generated by the controller are

recorded as the developed model is initiated in Simulink® environment. However, in order to observe the pre-states, three seconds of controller activation delay is inserted into the Simulink® model.

6.1 MSL ALTITUDE HOLD MODE

Total of four test results are presented in this section. In these tests, it is desired that the MSL altitude hold autopilot will hold the UAV at a fixed MSL altitude within ±10 m. For each test, the variation of UAV speed, UAV altitude with the desired flying altitude limits, and the elevator deflections are plotted as a function of time.

As mentioned before, flight path in the horizontal plane is tried to be kept linear during the phases when the autopilot is active and controlling the pitching motion. A sample test result given in Figure 44 shows that this is achieved to some extent.
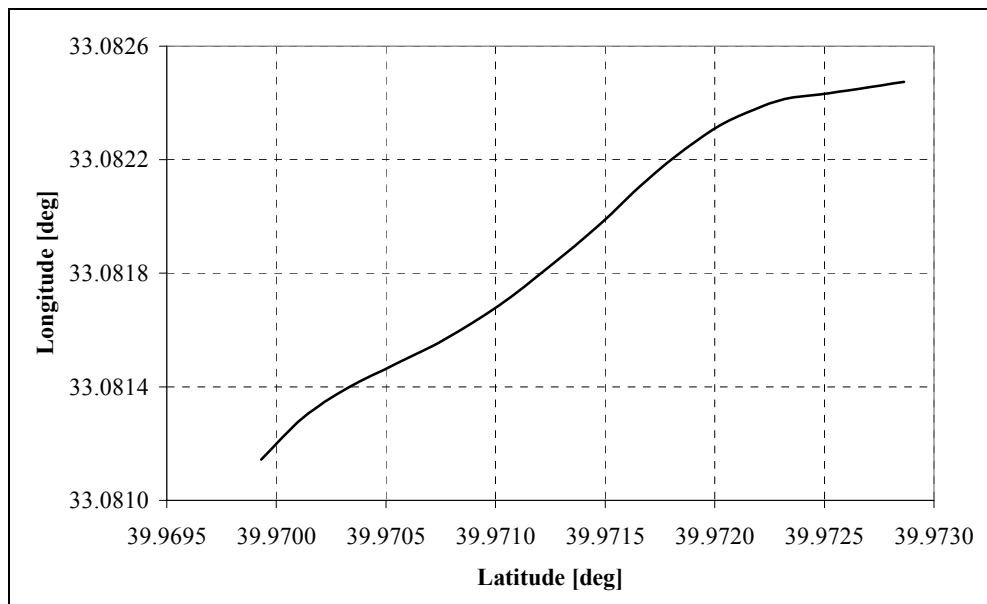

Figure 44. Horizontal trajectory in MSL altitude hold mode

6.1.1 MSL MODE FLIGHT TEST 1

In the MSL altitude hold mode flight test 1, the desired flight altitude is selected as 1300 m with respect to the MSL. Hence, the desired flying altitude band is 1300±10 m. The variations of the horizontal speed, altitude, and elevator deflection of the UAV with time are given in Figure 45 and Figure 46.

Figure 45. Variation of horizontal speed in MSL mode test 1

As the altitude variation of the UAV given in Figure 46 is examined, it is observed that the UAV ascends and exceeds the allowable altitude limits between 12 s < t < 13 s. It can also be seen that, the controller senses this undesired situation and immediately generates the required elevator deflection (at t=13 seconds) to descend the UAV. Note that the elevator deflection δ_e is taken as positive when the trailing edge is down as expressed before in Chapter 4. The controller increases the control command (elevator deflection) until a decrease in altitude is observed, and as the UAV starts to descend, it decreases the control command gradually.

Accordingly, the UAV is positioned within the altitude limits. Note that a small, constant, nonzero residual value for the elevator deflection exists after the UAV returns inside the desired band of altitude even the actuating error signal is zero. This is due to the unreset integral control action of the PID controller. The contribution of the integral control to the output signal (elevator deflection) at any moment is the area under the actuating error signal (required altitude change) versus time curve up to that moment. This value of the integral causes the output signal to have a nonzero value even if the error signal becomes and remains zero. Although this can be prevented by resetting the controller, it is not implemented in this study because of short periods of test flights.
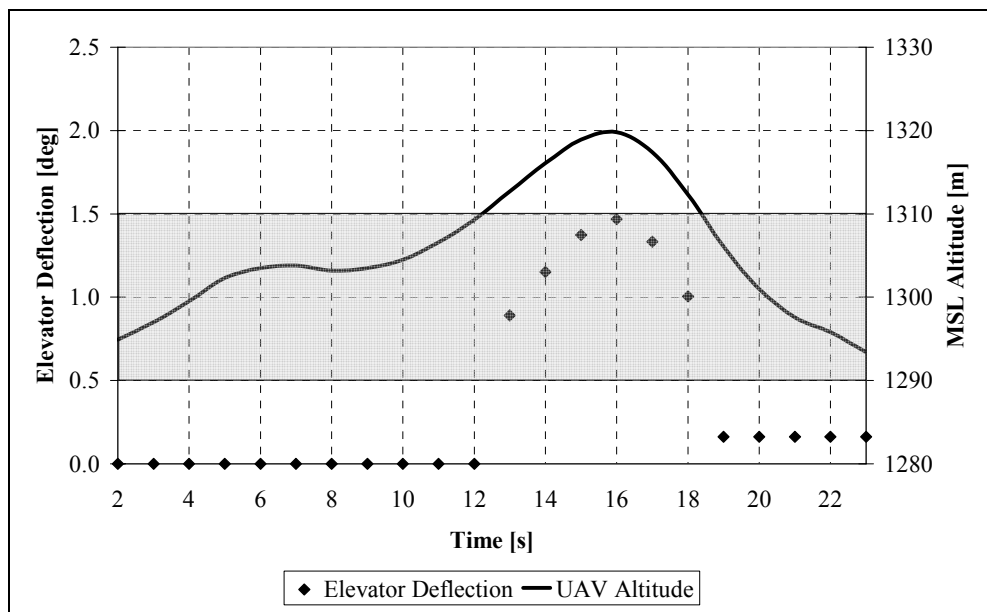
Figure 46. Variation of elevator deflection and altitude in MSL mode test 1

6.1.2 MSL MODE FLIGHT TEST 2

In the MSL altitude hold mode flight test 2, the desired flight altitude is selected as 1250 m with respect to the MSL. Hence, the desired flying altitude band is

112

1250±10 m. The variations of the horizontal speed, altitude, and elevator deflection of the UAV with time are given in Figure 47 and Figure 48.
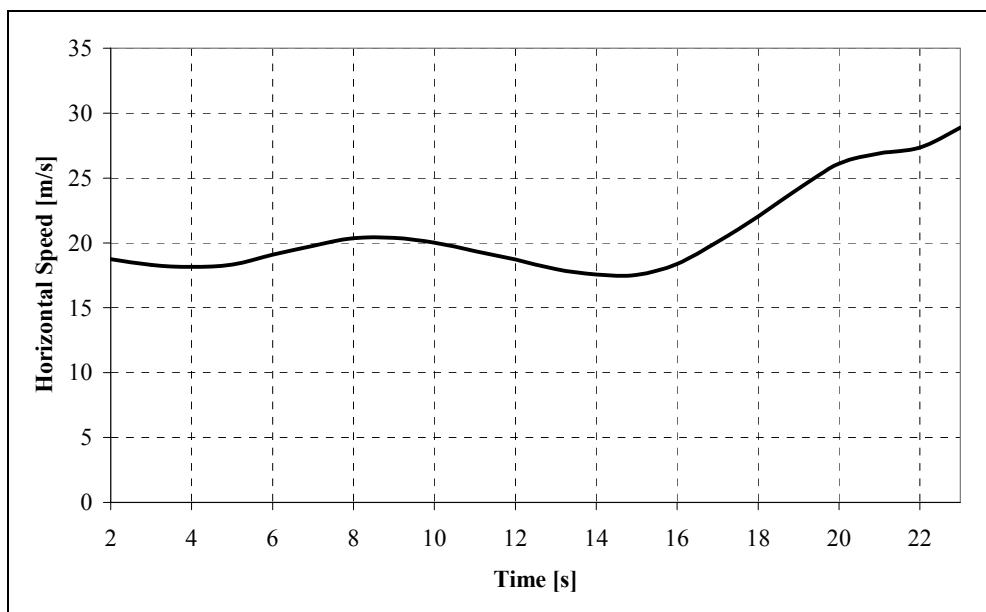

Figure 47. Variation of horizontal speed in MSL mode test 2
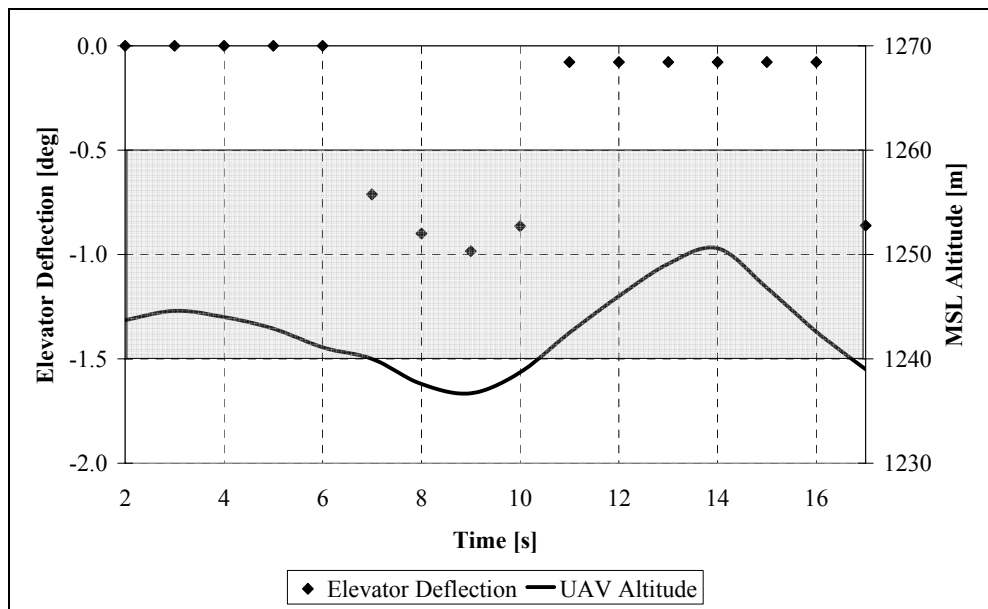
Figure 48. Variation of elevator deflection and altitude in MSL mode test 2

As the altitude variation of the UAV given in Figure 46 is examined, it is observed that the UAV descends and falls below the allowable altitude limits at t=7 seconds. The controller generates the required elevator deflection to ascend the UAV at the same instant. Hence, the UAV is positioned within the altitude limits after about four seconds. Same descent is also observed at t=17 seconds which is accompanied by an immediate elevator deflection.

6.1.3 MSL MODE FLIGHT TEST 3

In the MSL altitude hold mode flight test 3, the desired flight altitude is selected as 1300 m with respect to the MSL. Hence, the desired flying altitude band is 1300±10 m. The variations of the horizontal speed, altitude, and elevator deflection of the UAV with time are given in Figure 49 and Figure 50.
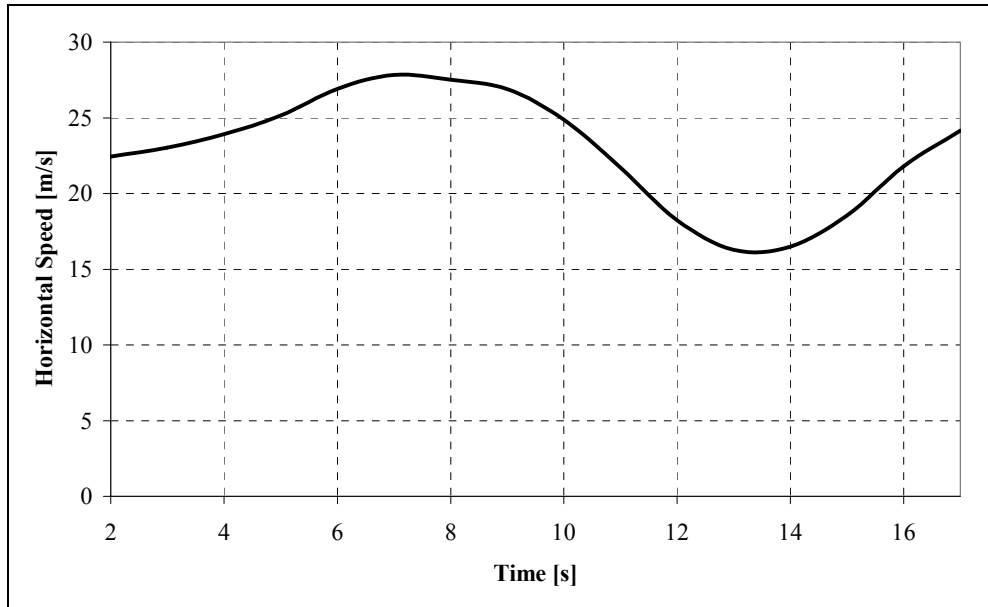

**Figure 49. Variation of horizontal speed in MSL mode test 3**

114
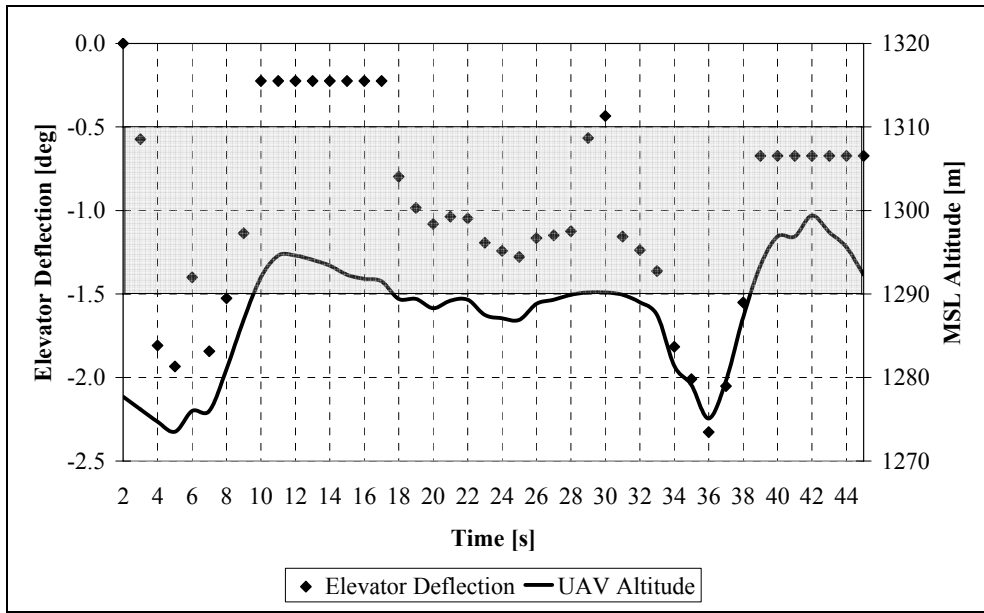
Figure 50. Variation of elevator deflection and altitude in MSL mode test 3

It is noteworthy that, this test has the longest duration among the MSL altitude hold mode tests. However, in this flight test, some problems with keeping the UAV at the design speeds are faced. The speed of the UAV is relatively low (<20 m/s) and almost half of the test is flied at low velocities. The main reason behind this situation is believed to be the windy condition with variable speeds under which this test is conducted. The wind speed is measured to be as high as 7 m/s during several tests which in turn slows or accelerates the UAV without demand. These adverse conditions have a negative effect on the controller performance in terms of its recovery time. In this particular flight test, the controller is switched on when the UAV flight altitude is below the limits, hence, it immediately generates the control command to return the vehicle within the limits. As the UAV descends and fall below the limits at t=18 seconds, the controller becomes active again. However it requires more time and a larger elevator deflection to ascend the vehicle because of the weather conditions. The effects of the unreset integral control action of the PID controller become more apparent especially during the last seven seconds of the flight test. This is expected intuitively since the period of the test is relatively long.

115

6.1.4 MSL MODE FLIGHT TEST 4

In the MSL altitude hold mode flight test 4, the desired flight altitude is selected as 1260 m with respect to the MSL. Hence, the desired flying altitude band is 1260±10 m. The variations of the horizontal speed, altitude, and elevator deflection of the UAV with time are given in Figure 51 and Figure 52.
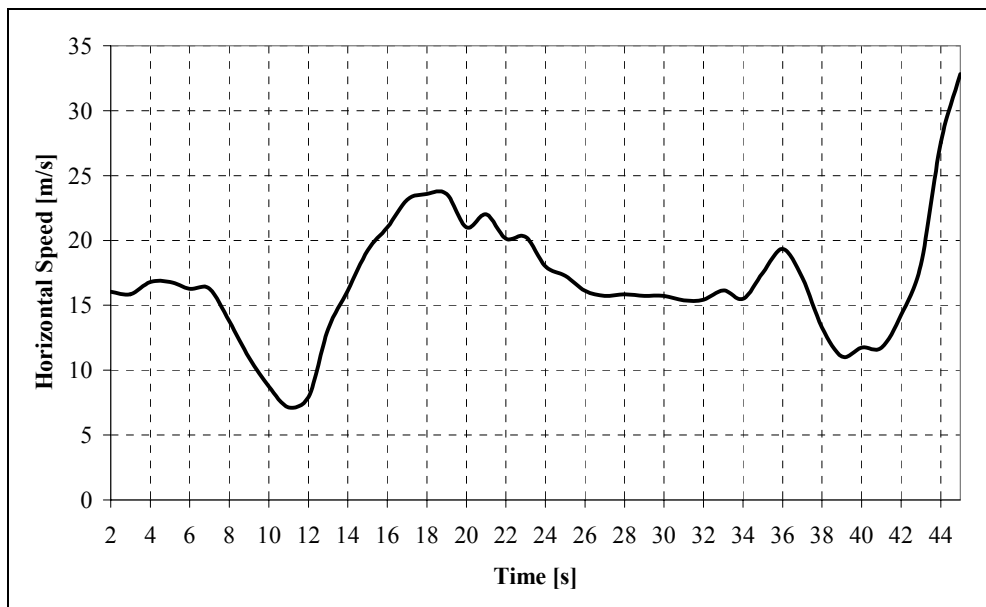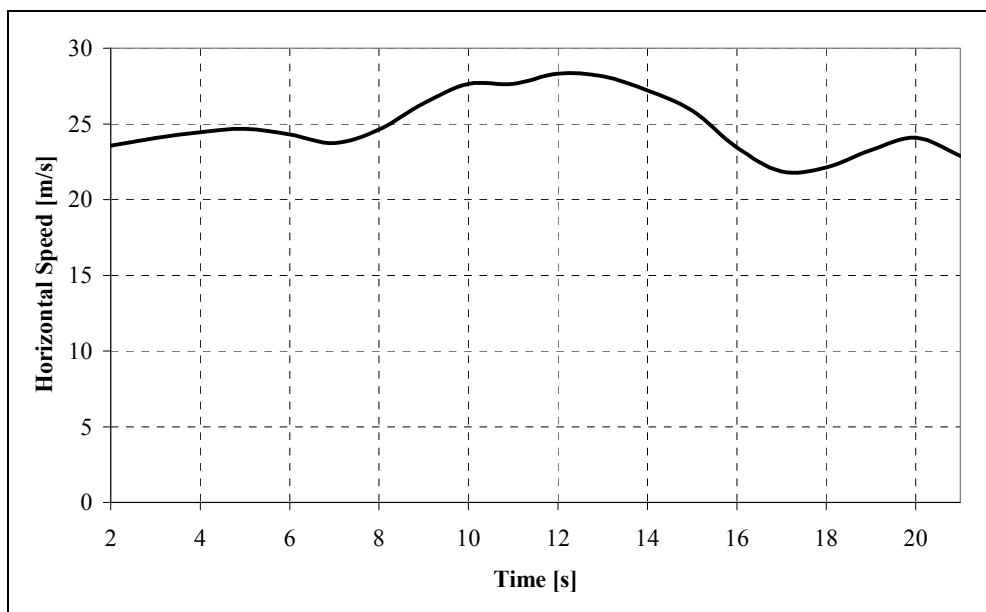

**Figure 51. Variation of horizontal speed in MSL mode test 4**

In this flight test, the controller is switched on when the UAV flight altitude is above the allowable altitude limits. Accordingly, the controller immediately starts to generate the control commands to return the vehicle back to the desired altitude limits, and it takes about seven seconds to accomplish this. In Figure 52, it is worth notice that a positive elevator deflection is generated at the initial period of the test to decrease the altitude of the vehicle. However, as the vehicle falls below the allowable altitude limits at the final period of the test, a negative elevator

deflection is generated by the controller which also overcomes the contribution of the integral control in the system.
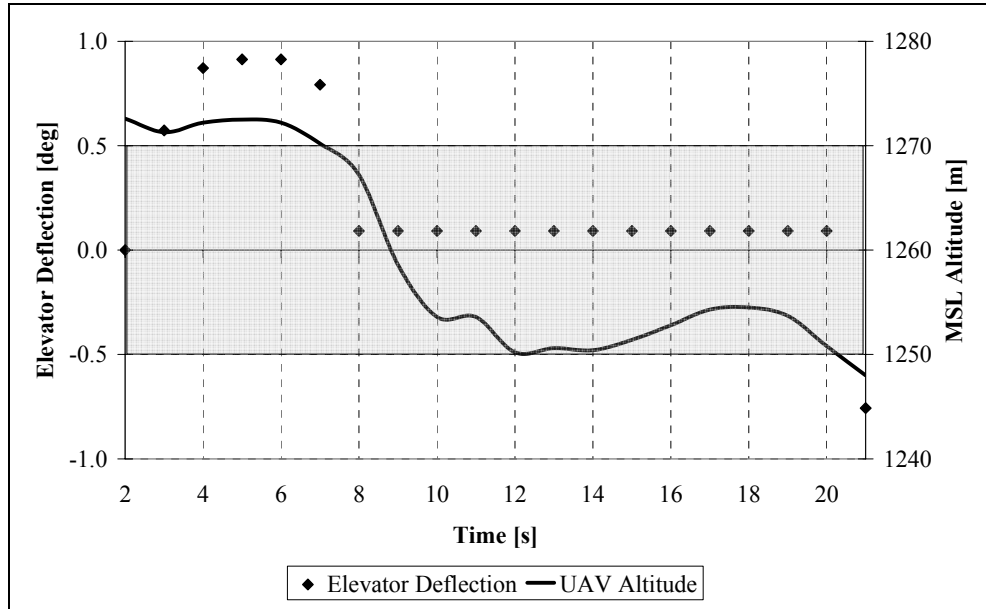
Figure 52. Variation of elevator deflection and altitude in MSL mode test 4

6.2 AGL ALTITUDE HOLD MODE

Total of three test results are presented in this section. In these tests, it is desired that the AGL altitude hold autopilot will hold the UAV at a fixed AGL altitude within ±10 m. For each test, the variation of UAV speed, UAV altitude with the desired flying altitude limits and the elevator deflections with time are plotted and presented.

The flight path of the UAV in the horizontal plane is tried to be kept linear during the phases when the autopilot is active and controlling the pitching motion. A sample test result given in Figure 53 shows that this is achieved to some extent.
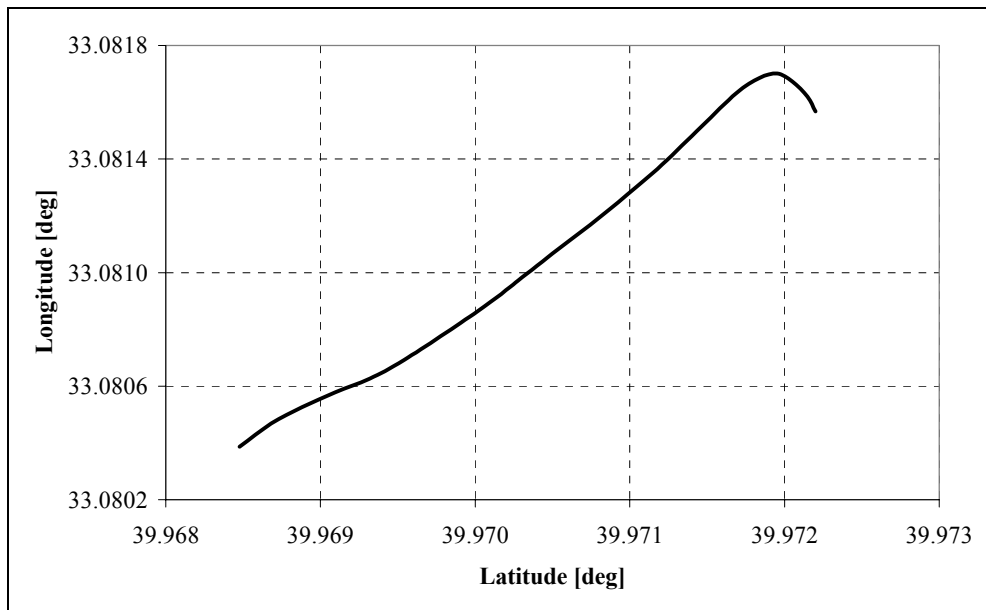
Figure 53. Horizontal trajectory in AGL altitude hold mode

6.2.1 AGL MODE FLIGHT TEST 1

In the AGL altitude hold mode flight test 1, the desired flight altitude is selected as 100 m with respect to the terrain. Hence, the desired flying altitude band is 100±10 m. The variations of the horizontal speed, altitude, and elevator deflection of the UAV with time are given in Figure 54 through Figure 56.

Test results show that, the controller takes an action to lower the altitude of the UAV as soon as it is activated (Figure 56). But the UAV continuously kept loosing its altitude until a moment when the elevator deflection is locally maximized, and the vehicle started to ascend from that moment. However, this increase in AGL altitude was not adequate to position the UAV within the desired altitude limits mainly because of the sudden speed drop of the vehicle as it can be seen from Figure 54. Since the vehicle's MSL altitude remains the same during this speed drop phase, only reason of this circumstance seems to be an opposing wind which in turn affects the performance of the controller in an adverse manner.

118

Figure 54. Variation of horizontal speed in AGL mode test 1

Figure 55. Variation of altitude in AGL mode test 1

119
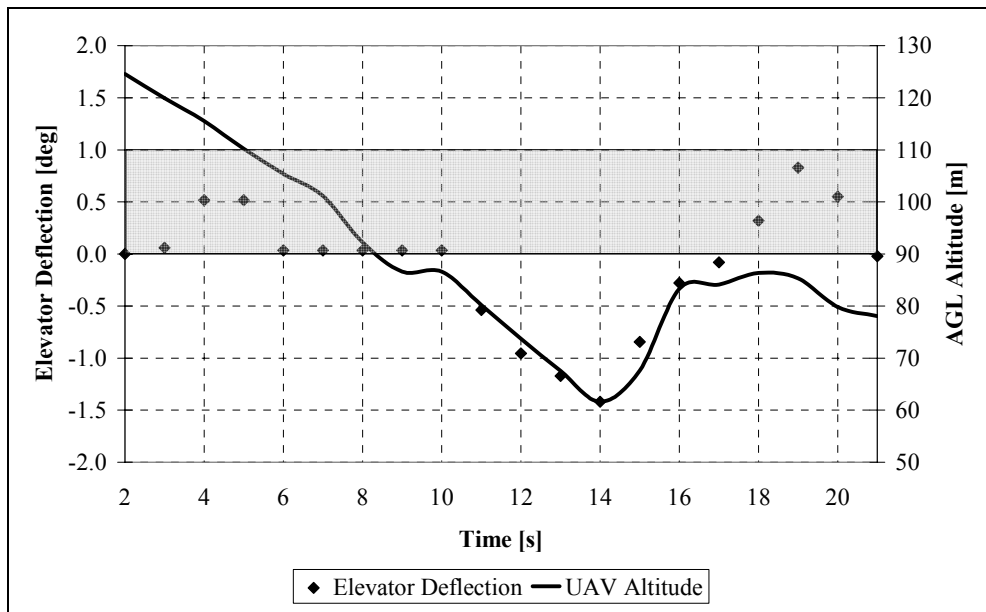
Figure 56. Variation of elevator deflection and altitude in AGL mode test 1

6.2.2 AGL MODE FLIGHT TEST 2

In the AGL altitude hold mode flight test 2, the desired flight altitude is selected as 100 m with respect to the terrain. Hence, the desired flying altitude band is 100±10 m. The variations of the horizontal speed, altitude, and elevator deflection of the UAV with time are given in Figure 57 through Figure 59.

As the AGL altitude variation of the UAV given in Figure 59 is examined, it is observed that the UAV descends and fall below the allowable altitude limits between 7 s < t < 8 s. It can also be seen from the same figure that, the controller generates the required elevator deflection (at t=8 seconds) to ascend the vehicle. Accordingly, the UAV is returned to the desired altitude limits within five seconds.
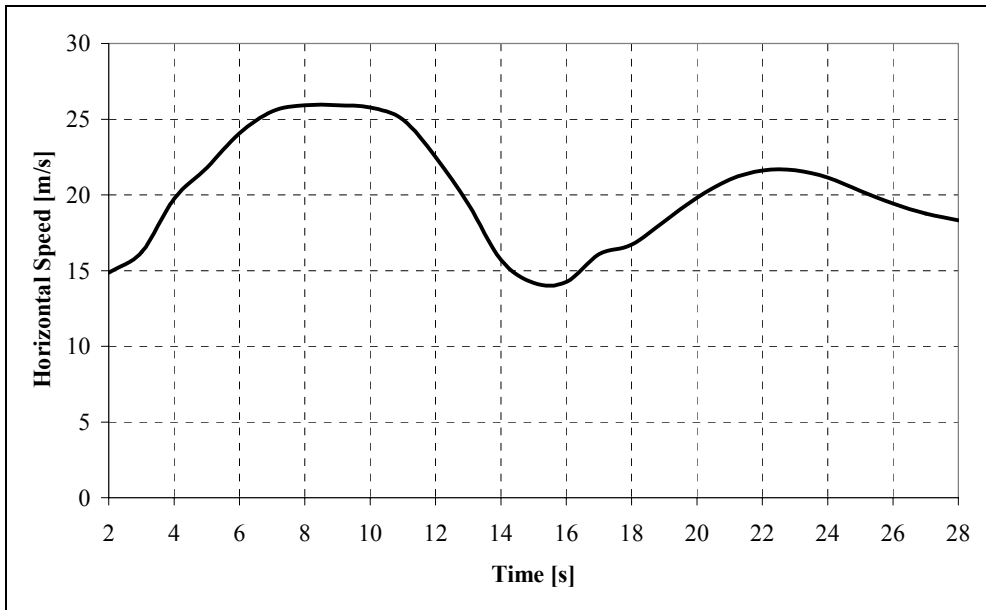
Figure 57. Variation of horizontal speed in AGL mode test 2
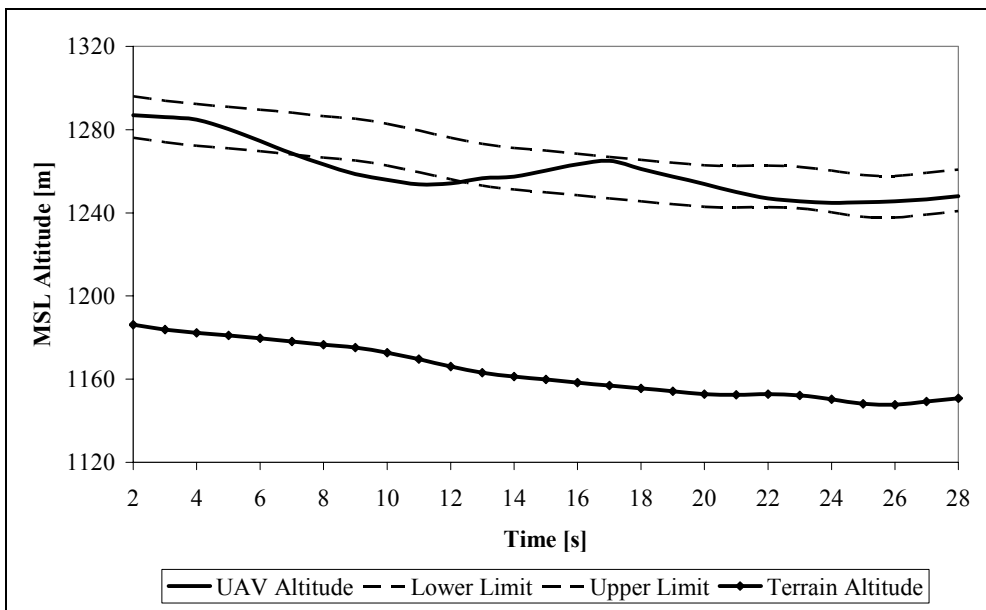
Figure 58. Variation of altitude in AGL mode test 2
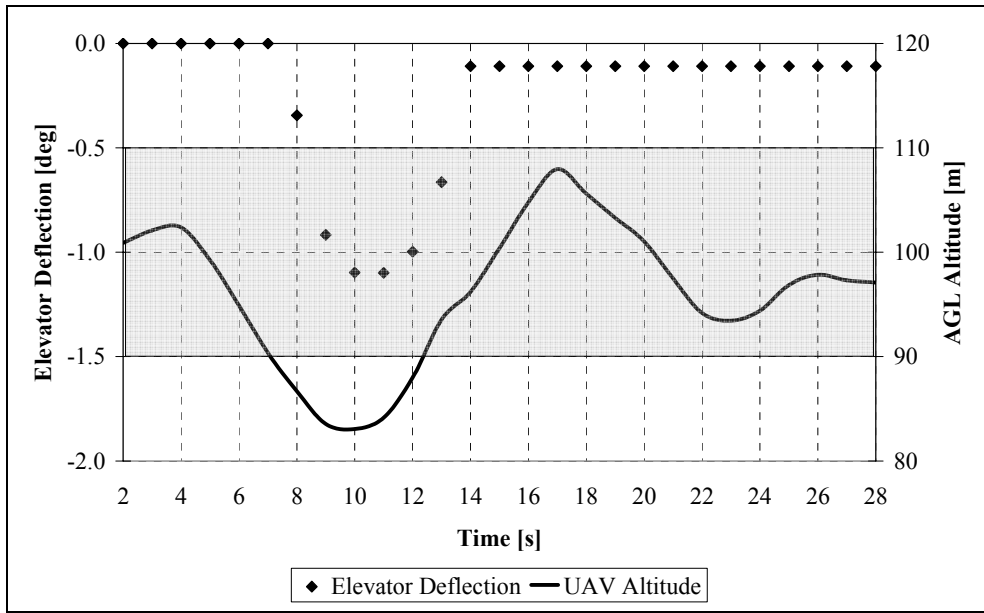
Figure 59. Variation of elevator deflection and altitude in AGL mode test 2

6.2.3 AGL MODE FLIGHT TEST 3

In the AGL altitude hold mode flight test 3, the desired flight altitude is selected as 100 m with respect to the terrain. Hence, the desired flying altitude band is 100±10 m. The variations of the horizontal speed, altitude, and elevator deflection of the UAV with time are given in Figure 60 through Figure 62.

This is the longest AGL altitude hold mode flight test presented in this study and probably the one that best demonstrates the working principle and performance of the controller. From Figure 62, the UAV is observed to diverge from the desired altitude limits at three distinct times; namely at t=7 seconds, t=18 seconds, and t=28 seconds. Examining the figure, the action of the controller at these diverging points can be clearly seen. Immediately after the UAV falls outside of the desired AGL altitude band, the controller generates an elevator deflection and returns back the UAV to the allowable altitude limits.
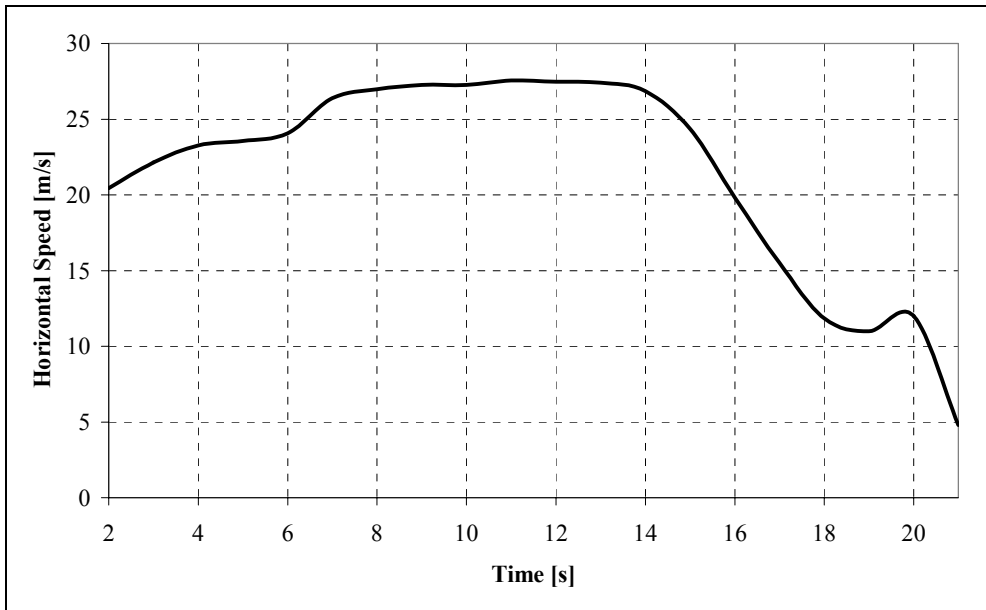
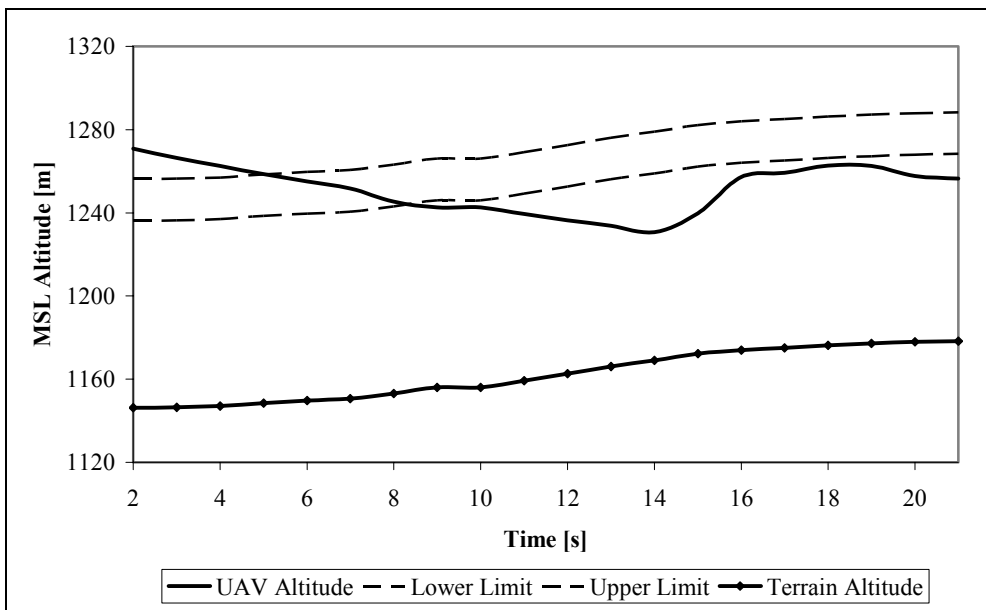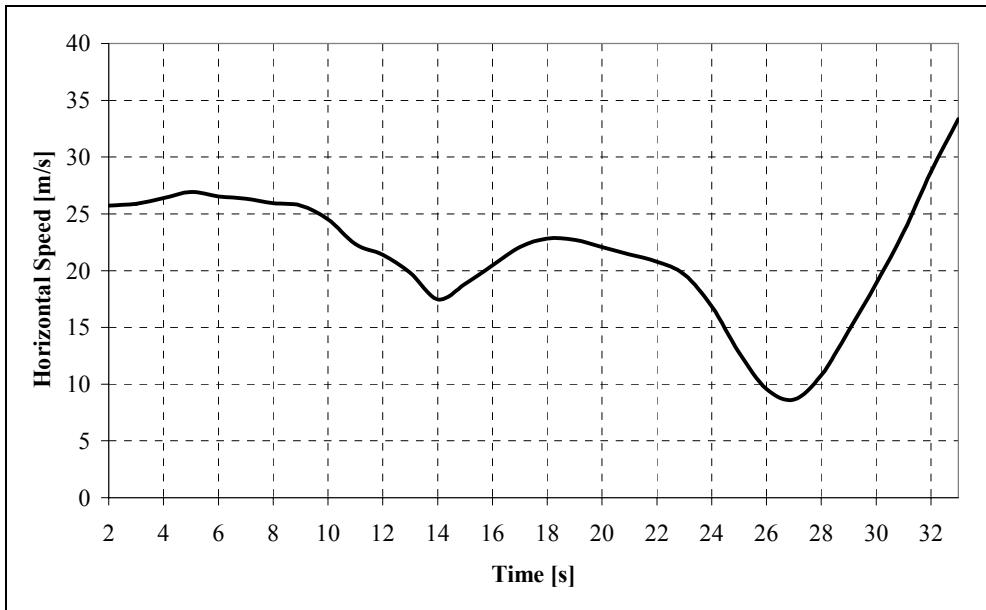**Figure 60. Variation of horizontal speed in AGL mode test 3**
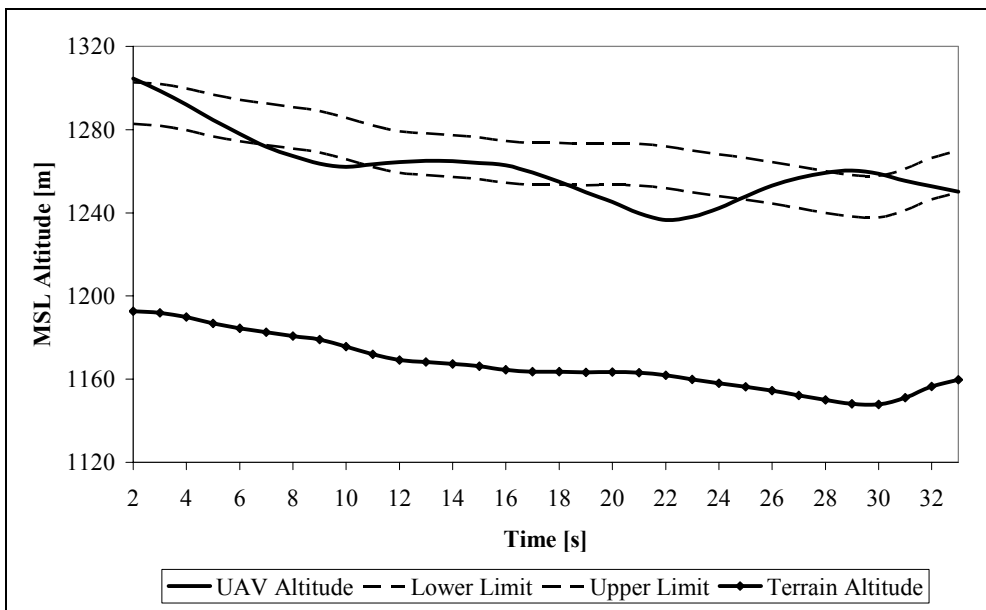
Figure 61. Variation of altitude in AGL mode test 3

123
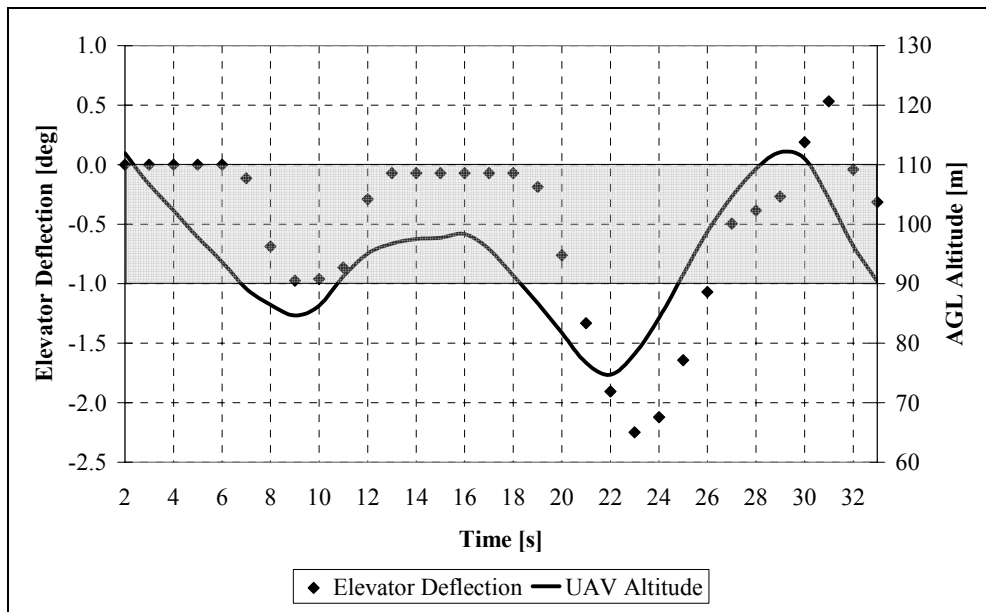
Figure 62. Variation of elevator deflection and altitude in AGL mode test 3

These total of seven tests are considered to be sufficient to understand to some extent the designed controller performance of the UAV prototype in real flight operations. It is possible to perform more tests to better understand the performance, however the limited time of the study and hostile weather conditions have an adverse effect on performing more flight tests.

6.3 GPS ACCURACY

The position data acquired by a GPS receiver has some errors within. The degree of this error or the accuracy of the position data can be observed by the inspection of several data (other than the position) acquired by the GPS. Hence, the reliability of the GPS data is investigated before dealing with the test results. A consistent and accurate position (latitude, longitude and altitude) data is required since the performance of the controller will be evaluated based on these data. For example, a test carried out with a few number of visible satellites decreases the position and altitude accuracy, which may cause some deviations in the reference input

124

(altitude) even if there is no change in the real altitude of the UAV. In addition to the number of visible satellites, the accuracy of the position obtained by a GPS depends on the geometrical configuration of the satellites used in the position calculation which is expressed by the PDOP (position dilution of precision) value. Data of the PDOP values and the number of satellites observed during the flight tests are given in Table 15 and Table 16.

Table 15. PDOP values during flight tests

Autopilot Mode	Test No	PDOP Value		
		Minimum	Maximum	Average
MSL altitude hold mode	1	1.92	3.57	2.11
	2	1.38	2.98	1.82
	3	2.05	4.84	2.68
	4	1.92	2.97	2.04
AGL altitude hold mode	1	1.73	3.12	2.10
	2	1.67	4.36	2.78
	3	1.51	6.99	3.44

Table 16. Number of visible satellites during flight tests

Autopilot Mode	Test No	Number of Visible Satellites		
		Minimum	Maximum	Average
MSL altitude hold mode	1	7	10	10
	2	7	11	9
	3	4	7	6
	4	5	8	8
AGL altitude hold mode	1	5	9	7
	2	5	9	6
	3	5	9	6

Figure 63 and Figure 64 are given to demonstrate the variation of PDOP value and the number of visible satellites during several flight tests.
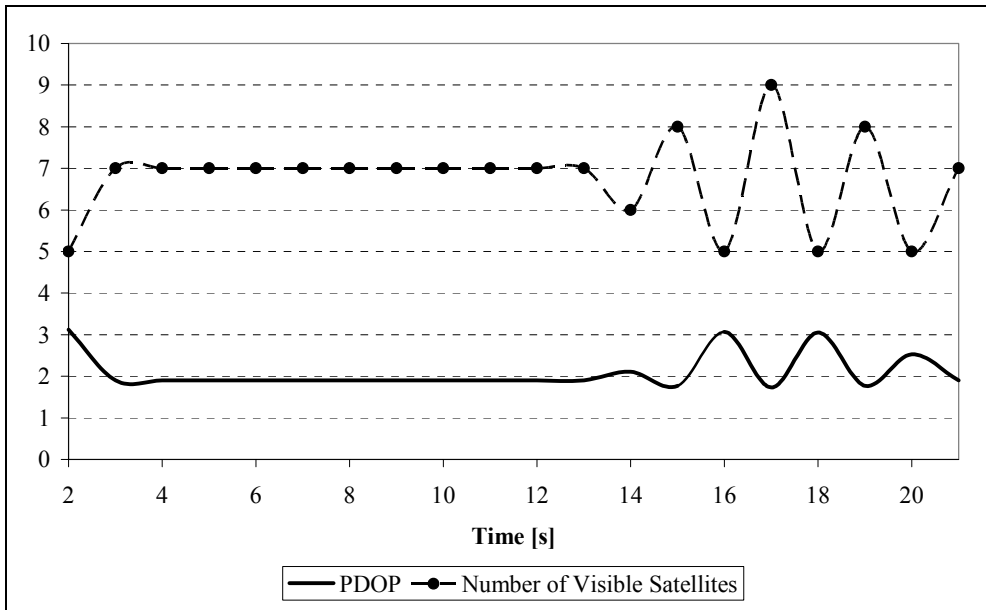
Figure 63. PDOP and number of visible satellites in AGL mode test 1
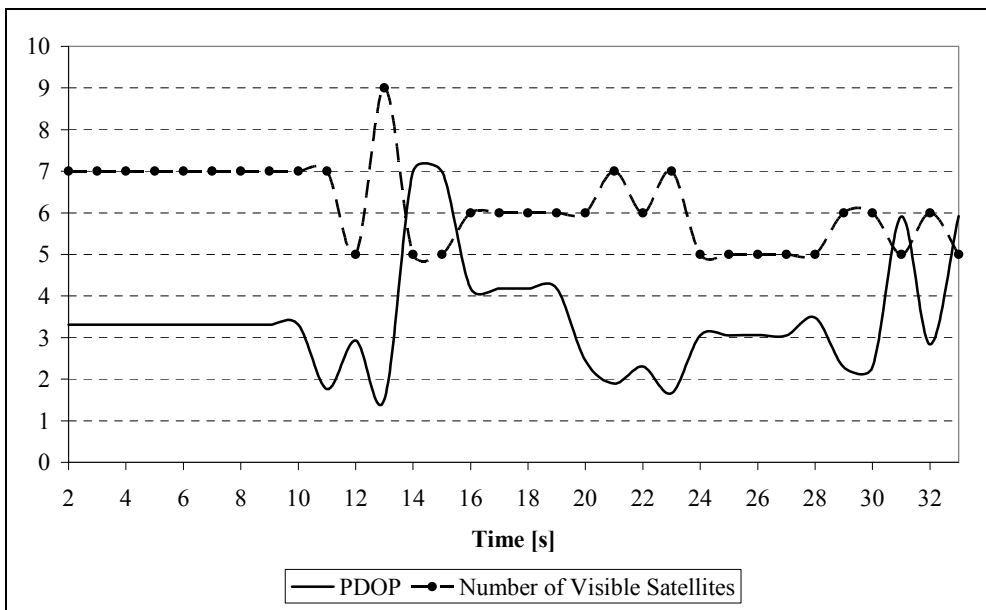
Figure 64. PDOP and number of visible satellites in AGL mode test 3

The PDOP has the best value of 1 while higher numbers being worse. A low number of PDOP (2) is good, whereas a high number (>7) is considered to be bad [25]. Reviewing Table 15, it can be stated that the accuracy of the GPS position can be considered as good for our application. This opinion can be supported by reviewing Table 16 and recalling that minimum of four GPS satellites is needed to determine a position in three dimensional space [25].

6.4 CONCLUDING REMARKS

As it is the general case, testing is the final phase in verifying newly developed systems. Thus, the UAV platform developed in this study is flight tested together with the designed controller and the results are presented in this chapter. The flight tests are carried out for two distinct autonomous flight modes. In the first set of tests, the UAV is tested to fly at a constant MSL altitude, whereas in the second set the autopilot mode is switched and the vehicle is tried to be kept at constant altitude from the underlying terrain.

Presented time histories are the horizontal speed, altitude, and elevator deflections of the UAV recorded during these tests. Furthermore, the basic GPS accuracy data acquired during the tests are given to comment on the reliability of the GPS position information upon which the developed controller system is built on.

As the controller is designed at three operating points corresponding to three flying speeds, a special attention should be given to the UAV horizontal speed data obtained from the tests. Inspecting the speed variations of the UAV with time, it is observed that in some tests (MSL altitude hold mode test 1, 2, 4 and AGL altitude hold mode test 3) there are slight violations of the allowable speed band ($20 - 27$ m/s) especially in the lower limit. However, the UAV remains outside of this speed band for very short period in these tests, and this situation does not seem to have severe effects on the performance of the controller.

Adverse weather conditions (wind, thermal effects, e.g.) and trim problems may have affected the overall performance of the UAV, since any loss of accuracy in trim process may result in a slowly ascending or descending motion even under uncontrolled (manual or automatic) flight.

Due to the unavailability of controlled test environment, test results are not compared with the simulation results. However, as the test results are examined, it is observed that the controller is acting exactly the way it should. No control input is calculated when the UAV is inside the predetermined MSL or AGL altitude band. However, when it diverges from the desired altitude limits, the controller calculates and sends the generated elevator deflections immediately to the vehicle. Thus, the UAV is positioned again within the desired altitude limits (Figure 65). Also the change in the vehicle altitude shortly after the elevator is deflected proved that the elevator deflection angles are measured accurately before the tests.
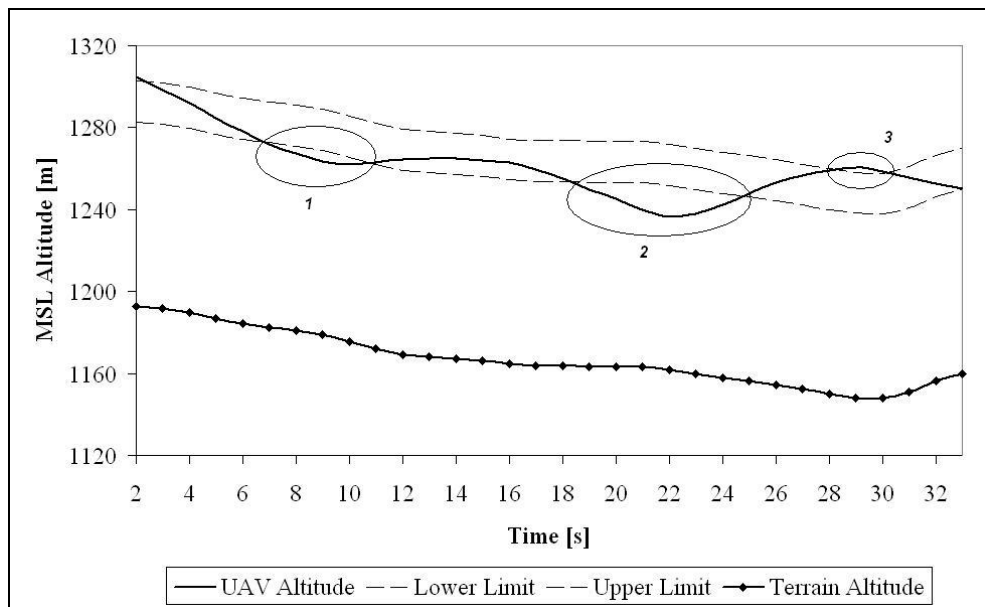
Figure 65. Performance analysis of the controller

CHAPTER 7

SUMMARY AND CONCLUSION

7.1 SUMMARY

As the UAVs can be used in both military and civil applications, and they are more advantageous when compared with the manned aerial vehicles, the interest and researches in UAV applications have increased dramatically in recent years. Many research centers and universities are investigating on small UAVs to test the newly developed algorithms and avionics prior to an advanced UAV system design. Basically, first step in these applications is to establish a flying platform resembling a small UAV. Some use scale aircraft models and some use their own designs for building the airframe of the small UAV. Upon this airframe, the avionics and equipment are implemented which enable data communication with a ground station and the navigation control of the vehicle. This control can be provided either by an onboard autopilot or by an autopilot running on a computer located at the ground.

Motivated by similar considerations, a flying test platform resembling a small UAV is developed in this thesis study. A suitable model RC airplane is selected and equipped with a GPS receiver and RF communication modules by which the GPS information (position, speed, heading, etc.) is transmitted to a ground computer. Moreover, to test basic control algorithms on this UAV prototype, an altitude hold autopilot (which is widely used in aviation) is designed and flight tested in this study. With this autopilot, air vehicle's flight at a fixed altitude with respect to the ground is provided using the DTED of the underlying terrain. The

autopilot generates the required control commands for the elevator position to hold the UAV within a predefined altitude band and when the UAV is within the band, it generates no corrective action.

Prior to the autopilot design process, the longitudinal equations of motion and the longitudinal transfer functions of an airplane in perturbed state flight are generated. Then, a relationship between the elevator deflection and altitude is defined and the corresponding transfer function is derived. Finally, the aerodynamic parameters of the RC airplane are obtained by using the aerodynamic parameter estimation program USAF DIGITAL DATCOM. Note that, throughout the study only the longitudinal motion of the UAV is considered and any lateral motion is neglected.

Following the ground tests which ensure the reliable operation of the equipment implemented both on the airplane and on the ground, flight tests are performed with the instrumented UAV prototype. These flight tests are performed under two different autopilot modes, namely the MSL altitude hold mode, and the AGL altitude hold mode. After the takeoff, the UAV is trimmed manually from the ground to avoid any rolling, pitching, or yawing motion during the uncontrolled phase. When this trimming is completed, the controller working in MATLAB® environment is activated. The controller receives the GPS position data from the UAV, calculates and sends the required control variable (elevator deflection) back to the vehicle to provide a flight at the desired altitude. Several GPS data, necessary to measure and demonstrate the performance of the controller, are recorded during these tests and presented in this study.

7.2 CONCLUSION

This study is devoted to the understanding of small UAV applications and the technologies used to develop a flying platform which enables data communication

between itself and a ground station. Moreover, theoretical knowledge in dynamic modeling a flying vehicle and implementing an autopilot is applied to a real problem in the study.

GPS receiver and the communication modules worked properly during both in ground and flight tests, and proved to be reliable in almost every condition. Investigation of the test results showed that the GPS position data is relatively good and reliable for this study. In cases where the flight velocities are higher and more accuracy in the position is required, either a high performance antenna should be used or the number of visible satellites should be checked prior to the flight. Furthermore, using a DGPS can also solve this problem.

DTED is proven to be reliable after some ground tests are performed near the test area located at TÜBİTAK-SAGE. The maximum error between the terrain altitude obtained from the DTED and the GPS altitude of the UAV resting on the ground is around 5 meters, which is relatively good considering the accuracies of the GPS altitude data and DTED.

Although some assumptions are made during the mathematical modeling phase, test results show that it is appropriate to test similar control algorithms with this airframe. However, it should not be forgotten that this is an approximate model, and should be verified with additional flight tests.

Last and the most critical phase of this study is the flight testing of the developed systems and the designed autopilot. At first glance although the testing seems to be straightforward, when testing procedure begins, it does not take long time to realize how complicated the testing phase could be.

Minimum of one hour is needed to setup the UAV prototype and the ground station. Furthermore, during the flight tests considerable amount of time is required for the trimming process of the airplane which in turn provides the

longitudinal motion. However, wind speed and direction variations are difficult to predict, and these together with the thermal effects cause some undesired responses in many flight tests. Hence, weather conditions have a great influence on the number of successful flight tests. Many tests are repeated or aborted due to adverse weather conditions.

Another problem arises from the weak structure of the RC airplane. Several delays (at least one week each) are encountered because of the failure of several mechanical parts of the RC airplane. It is obvious that the testing period would be relatively short if the airplane had a tough airframe.

Flight test results are given as plots showing the variation of speed, altitude (with the desired flying altitude limits), and elevator deflection of the UAV with time. From the test results, it can be seen that the autopilot can hold the UAV at a desired MSL or AGL altitude within a band by generating elevator deflections. Although the test results are not compared with the simulation results due to unavailability of a controlled flight environment, the results presented in Chapter 6 showed that the autopilot acts effectively against any terrain and UAV altitude variations, and immediately tries to hold the UAV within the desired flight altitude limits.

7.3 FUTURE WORK

The platform developed in this study enables many future applications to be tested with this UAV prototype. New control algorithms and avionics can be easily tested with this platform. Since the autopilot is running in MATLAB® Simulink® environment in a ground computer, trying new control algorithms, such as full autonomous control and waypoint navigation on this platform is a straightforward application. Note that the algorithms can also be changed during the flight tests by switching to manual control.

The UAV can also be equipped with an onboard computer which receives data from the onboard sensors (IMU, GPS, Pitot tube etc.), and generates the required control surface deflections. Thus, a control computer on the ground will no longer be needed for autonomous control mode. This application will make a great contribution towards the development of an advanced UAV system. Note that, a remote control mode will still be needed to override the onboard computer commands in case an emergency situation occurs.

In this study, only the longitudinal dynamics of the UAV is analyzed, and the equations of motion are derived for 3 DOF motion. However, to increase the capabilities of the controller, hence to provide full autonomous control, the lateral dynamics and the coupling effects should also be analyzed in future studies.

For autonomous control applications during cruise phase of small UAV flight missions, GPS and INS based navigation is used to measure airplane states accurately. Since this type of navigation is not accurate enough for take off and landing phases, airborne altimeters such as laser or radar altimeters are required to provide the required accuracy for full autonomy. Hence, these systems can be implemented on this platform in the future to handle the control during take off and landing phases.

The GPS receiver board can support up to 4 Hz position update rate. However, due to fact that the cruise speed of our flying platform is relatively low (~30 m/s), a position update at 1 Hz is considered to be appropriate for the study. In the future this update rate can be increased to have a better understanding of the system.

Although there is an integral control action on the system, resetting the controller is not carried out in this study as the controller acts for relatively short periods. However, this will cause severe effects on the controller performance as the

duration of the autonomous control mode increases. Therefore, the controller should be reset in future applications, especially in long periodical ones.

It is seen in this study that the operating points (horizontal speed) selected for the gain scheduling technique did not exactly meet the flight speeds observed during the tests. The effect of speed on controller performance should be investigated carefully by performing more tests in future works.

REFERENCES

[1]   *Aerospace America*, AIAA, Vol. 43, No. 9, September 2005.

[2]   General Atomics Aeronautical Systems, *Predator*, http://www.uav.com/products/predator.html, 2005.

[3]   Abusleme, A., Cipriano, A. and Guarini, M., *A Low-Cost Altitude Control System for the Kadet Senior Radio-Controlled Airplane*, IEEE Transactions on Education, Vol. 46, No. 1, February 2003, pp. 50-60.

[4]   Kaminer, I., Yakimenko, O., Dobrokhodov, V., Lim, B., *Development and Flight Testing of GNC Algorithms Using a Rapid Flight Test Prototyping System*, AIAA 2002-4653, August 2002.

[5]   Liang, F., *Rapid Development of UAV Autopilot Using MATLAB$^®$/ Simulink$^®$*, AIAA 2002-4976, August 2002.

[6]   Lee, S., Lee, T., Park, S., Kee, C., *Flight Test Results of UAV Automatic Control Using a Single-Antenna GPS Receiver*, AIAA 2003-5593, August 2003.

[7]   Nilsson, C., Hall, C., Heinzen, S., Chokani, N., *GPS Auto-Navigation Design For Unmanned Air Vehicles*, AIAA 2002-0389, January 2002.

[8]   Roskam, J., *Airplane Flight Dynamics and Automatic Flight Controls Part I*, Design, Analysis and Research Corporation, Kansas, 1995.

[9]   Phillips, W.F., *Mechanics of Flight*, John Wiley & Sons, Inc., New Jersey, 2004.

[10]   Özgören, M.K., *Topological Analysis of Six-Joint Serial Manipulators and Their Inverse Kinematic Solutions*, Journal of Mechanism and Machine Theory, Vol. 37, 2002, pp. 511-547.

[11]   Özgören, M.K., *Some Remarks on Rotation Sequences and Associated Angular Velocities*, Journal of Mechanism and Machine Theory, Vol. 29, No. 7, 1994, pp. 933-940.

[12]   Özgören, M.K., *Kinematic Analysis of a Manipulator With Its Position and Velocity Related Singular Configurations*, Journal of Mechanism and Machine Theory, Vol. 34, 1999, pp. 1075-1101.

[13]   Schmidt, L.V., *Introduction to Aircraft Flight Dynamics*, American Institute of Aeronautics and Astronautics Inc., Virginia, 1998.

[14]   Blakelock, J.H., *Automatic Control of Aircraft and Missiles, 2nd Ed.*, John Wiley & Sons, Inc., 1991.

[15]   Roskam, J., *Airplane Flight Dynamics and Automatic Flight Controls Part II*, Design, Analysis and Research Corporation, Kansas, 1995.

[16]   *The USAF Stability and Control Digital DATCOM Volume I, Users Manual*, McDonnell Douglas Astronautics Company, Missouri, 1979.

[17]   Anderson, J.D., *Introduction to Flight, 3rd Ed.*, McGraw-Hill Book Company, 1989.

[18]   Applebaum, E., *Fuzzy Gain Scheduling for Flutter Suppression in Unmanned Aerial Vehicles*, IEEE 22nd International Conference of the North American , July 2003, pp. 323-328.

[19] Zhao, Z., *Fuzzy Gain Scheduling of PID Controllers*, IEEE Transactions on Systems, Man and Cybernetics, Vol. 23, No. 5, 1993, pp. 1392-1398.

[20] Oosterom, M., Schram, G., Babuska, R., Verbruggen, H.B., *Automated Procedure for Gain Scheduled Flight Control Law Design*, AIAA Guidance, Navigation, and Control Conference and Exhibit, Denver, 2000.

[21] Rugh, W.J., *Analytical Framework for Gain Scheduling*, IEEE Control Systems Magazine, Vol. 11, No. 1, January 1991, pp. 79-84.

[22] Etkin, B., Reid, L.D., *Dynamics of Flight*, *3rd Ed.*, John Wiley & Sons, Inc., Toronto, 1994.

[23] *Simulink$^{®}$ Response Optimization User's Guide Version 3*, The MathWorks, Inc., 3 Apple Hill Drive Natick, MA, March 2006.

[24] U-BLOX, *RCB-LJ GPS Receiver Board Data Sheet, Doc. No: GPS.G3-PS3-03019-C*, http://www.u-blox.com, 2005.

[25] U-BLOX, *GPS Basics, Introduction to the System Application Overview, Doc. No: GPS-X-02007*, http://www.u-blox.com, 2005.

[26] U-BLOX, *ANN Active GPS Antenna Data Sheet, Doc. No: GPS-X-02021-A*, http://www.u-blox.com, 2005.

[27] *Sayısal Harita ve Coğrafi Bilgi Sistemi Kurs Notları*, General Mapping Command of Turkey, Ankara, 2003.

APPENDIX A

DIGITAL TERRAIN ELEVATION DATA

DTED is a uniform matrix of terrain elevation values which provides basic quantitative data for systems and applications that require terrain elevation, slope, and surface roughness information. DTED has been developed by NIMA for military applications.

There are three types of DTED are available which are Level 0, Level 1, and Level 2. The accuracy of the terrain elevation increases as the level of DTED increases. Hence, Level 2 has the most accurate and reliable elevation values.

DTED Level 0 is derived from DTED Level 1 to support a federal agency requirement, and it is available to public at no charge through the internet. The elevation post spacing of Level 0 is 30 arc seconds (nominally one kilometer). It allows a gross representation of the Earth's surface for general modeling activities. However, such reduced resolution data is not intended and should not be used for automated flight guidance or other precision activities.

DTED Level 1 is the basic medium resolution elevation data source for all military activities and systems that require landform, slope, elevation, and gross terrain roughness in a digital format. Its post spacing is 3 arc seconds (approximately 100 m). The information content is approximately equivalent to the contour information represented on a 1:250,000 scale map.

DTED Level 2 is the basic high resolution elevation data source for all military activities and systems that require landform, slope, elevation, and terrain roughness in a digital format. Its post spacing is 1 arc second (approximately 30 m). The information content is equivalent to the contour information represented on a 1:25,000 scale map.

The specifications of the DTED provided by the General Mapping Command of Turkey are given in Table 17 [27].

Table 17. Specifications of DTED [27]

DTED Type	DTED Level 1	DTED Level 2
Map Scale	1/250,000	1/25,000
Horizontal Datum	WGS84	WGS84
Vertical Datum	MSL	MSL
Post Spacing	3" x 3"	1" x 1"
Map Coverage	1° x 1°	7.5' x 7.5'
Unit File Size	3 MB	0.5 MB
Resolution/Accuracy	±50 m horizontal ±30 m altitude	±26 m horizontal ±20 m altitude
Confidentiality	Unclassified	Classified

DTED Level 2 used in this study which covers the test area located at TÜBİTAK-SAGE is shown in Figure 66.
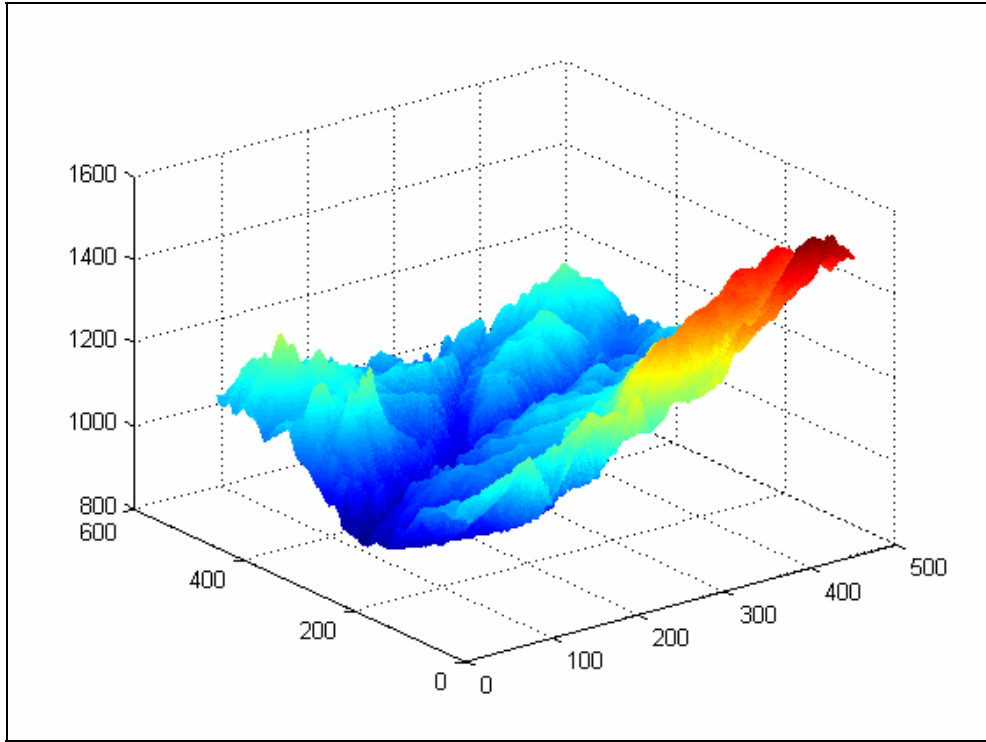
Figure 66. DTED Level 2 map covering TÜBİTAK-SAGE

APPENDIX B

MODELING THE RC AIRPLANE

This appendix gives general information on how the input file for USAF DIGITAL DATCOM [16] is generated for the Super Frontier Senior RC model airplane. DIGITAL DATCOM employs the namelist input technique for introducing the input data to the program. Each namelist variables and the generated inputs for the RC airplane are given below. The resulting input file is given at the end of this Appendix.

Namelist FLTCON defines the flight conditions. Program has a standard atmosphere model and by providing the Mach number(s) and altitude(s) as inputs, it accurately calculates the Reynolds number.

Table 18. Namelist FLTCON

VARIABLE	DEFINITION	UNIT
NMACH	Number of Mach numbers or velocities to be run, maximum of 20	-
MACH	Values of free stream Mach number	-
NALPHA	Number of angles of attack to be run, maximum of 20	-
ALSCHD	Values of angles of attack, tabulated in ascending order	DEG
NALT	Number of atmospheric conditions to be run, maximum of 20	-
ALT	Values of geometric altitudes	L

Hence, the namelist FLTCON generated for the Super Frontier Senior RC airplane is;

$FLTCON NMACH=5.,MACH(1)=0.04,0.05,0.06,0.07,0.08,NALPHA=20.,
  ALSCHD(1)=-20.,-15.,-10.,-8.,-6.,-4.,-3.,-2.,-1.,0.,1.,2.,3.,4.,6.,8.,10.,
  12.,16.,20.,NALT=5.,ALT(1)=1200.,1200.,1200.,1200.,1200.$

Reference area and lengths of the airplane are defined by the namelist OPTINS.

Table 19. Namelist OPTINS

VARIABLE	DEFINITION	UNIT	VALUE
ROUGHFC	Surface roughness factor, equivalent sand roughness. Default to 0.16×10^{-3} inches, or 0.406×10^{-3} cm, if not input	L	-
SREF	Reference area. Value of theoretical wing area used by program if not input	A	0.7877
CBARR	Longitudinal reference length value of theoretical wing mean aerodynamic chord used by program if not input	L	0.385
BLREF	Lateral reference length value of wing span used by program if not input	L	2.046

Hence, the namelist OPTINS generated for the Super Frontier Senior RC airplane is;

$OPTINS SREF=0.7877,CBARR=0.385,BLREF=2.046$

The basic configuration synthesis parameters of the airplane, shown in Figure 67 [16], are defined by the namelist SYNTHS.

142
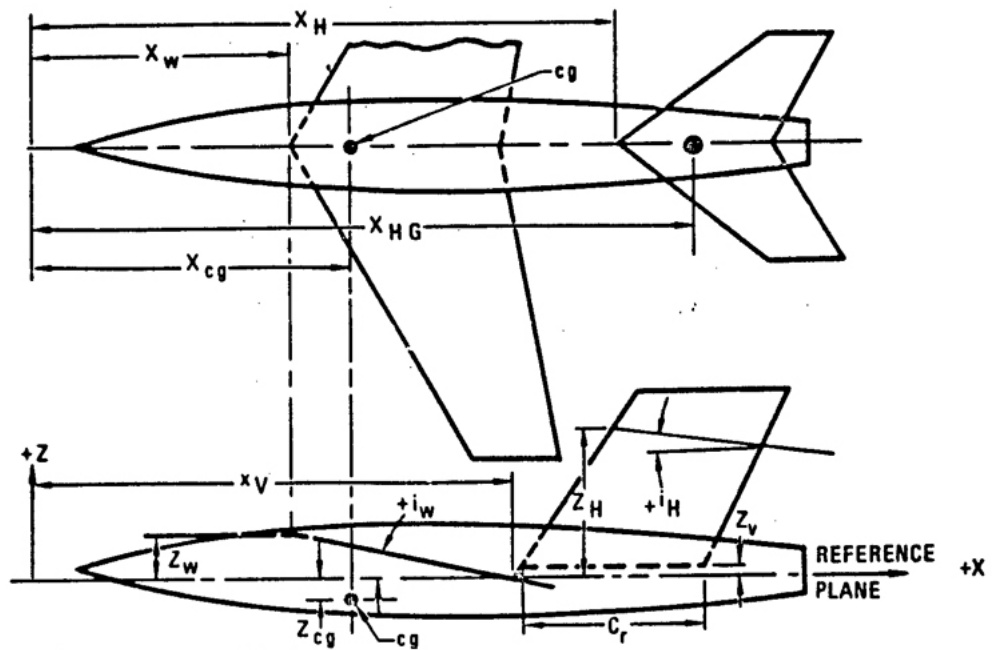
Figure 67. Parameters in namelist SYNTHS [16]

Table 20. Namelist SYNTHS

SYMBOL	VARIABLE	DEFINITION	UNIT	VALUE
x_{cg}	XCG	Longitudinal location of CG	L	0.4
z_{cg}	ZCG	Vertical location of CG relative to reference plane	L	0
x_w	XW	Longitudinal location of theoretical wing apex	L	0.35
z_w	ZW	Vertical location of theoretical wing apex relative to reference plane	L	0.1
i_w	ALIW	Wing root chord incidence angle measured from reference plane	DEG	0
x_H	XH	Longitudinal location of theoretical horizontal tail apex	L	1.28

143

Table 20. Namelist SYNTHS (continued)

SYMBOL	VARIABLE	DEFINITION	UNIT	VALUE
z_H	ZH	Vertical location of theoretical horizontal tail apex relative to reference plane	L	0.022
i_H	ALIH	Horizontal tail root chord incidence angle measured from reference plane	DEG	0
x_V	XV	Longitudinal location of theoretical vertical tail apex	L	1.16
z_V	ZV	Vertical location of theoretical vertical tail apex	L	0.032

Hence, the namelist SYNTHS generated for the Super Frontier Senior RC airplane is;

$SYNTHS XCG=0.4,ZCG=0.,XW=0.35,ZW=0.1,ALIW=0.,XH=1.28,
 ZH=0.022,ALIH=0.,XV=1.16,ZV=0.032$

The body configuration, shown in Figure 68 [16], is defined using the namelist BODY.
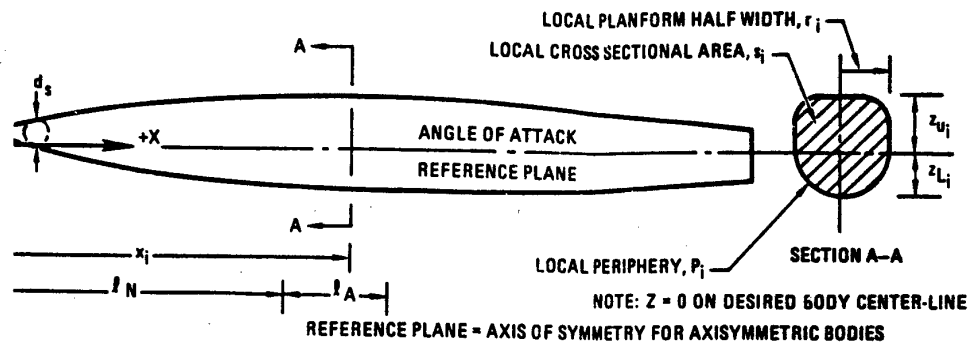
Figure 68. Parameters in namelist BODY [16]

Table 21. Namelist BODY

VARIABLE	DEFINITION	UNIT
NX	Number of longitudinal body stations at which data is specified, maximum of 20	-
X	Longitudinal distance measured from arbitrary location	L
R	Planform half width at station x_i	L
ZU	Z coordinate at upper body surface at station x_i (positive when above centerline)	L
ZL	Z coordinate at lower body surface at station x_i (negative when below centerline)	L

Hence, the namelist BODY generated for the Super Frontier Senior RC airplane is;

$BODY NX=9.,
  X(1)=0.0,0.15,0.24,0.3,0.355,0.736,0.888,1.166,1.515,
  R(1)=0.0,0.076,0.079,0.095,0.109,0.101,0.088,0.061,0.027,
  ZU(1)=0.,0.044,0.048,0.095,0.12,0.103,0.084,0.049,0.021,
  ZL(1)=0.,-0.087,-0.092,-0.095,-0.098,-0.09,-0.079,-0.059,-0.028$

The section aerodynamic characteristics of the wing, shown in Figure 69 [16], are defined using the namelist WGSCHR.
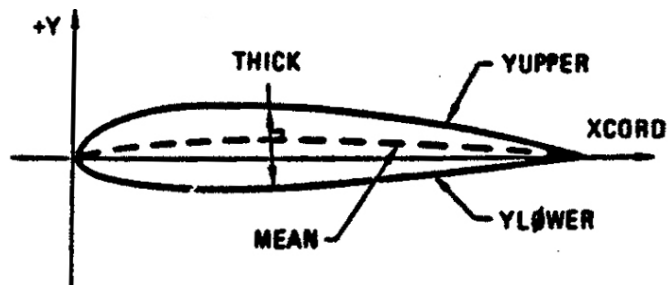
Figure 69. Parameters in namelists WGSCHR, HTSCHR, and VTSCHR [16]

Table 22. Namelist WGSCHR

SYMBOL	VARIABLE	DEFINITION
	TYPEIN	Type of airfoil section coordinates input for airfoil section module =1.0 upper and lower surface coordinates =2.0 mean line and thickness distribution
	NPTS	Number of section points input, maximum of 50
X_c/c	XCORD	Abscissas of input points, TYPEIN=1.0 or 2.0, XCORD(1)=0.0 and XCORD(NPTS)=1.0
Y_U/c	YUPPER	Ordinates of upper surface, TYPEIN=1.0 Fraction of chord, and requires YUPPER(1)=0.0 YUPPER(NPTS)=0.0
Y_L/c	YLOWER	Ordinates of lower surface, TYPEIN=1.0 Fraction of chord, and requires YUPPER(1)=0.0 YUPPER(NPTS)=0.0

Hence, the namelist WGSCHR generated for the Super Frontier Senior RC airplane is;

$WGSCHR TYPEIN=1.,NPTS=14.,
  XCORD(1)=0.,0.0571,0.10909,0.2447916,0.34545,0.441558,0.584415,
  0.6961,0.766233,0.8,0.9,0.95,.975,1.,
  YUPPER(1)=0.,0.0883,0.104,0.122,0.117,0.096,0.078,0.065,0.057,
  0.03,0.016,0.0068,0.,
  YLOWER(1)=0.,-0.0001,-0.0001,-0.0001,-0.0001,-0.0001,-0.0001,
  -0.0001,-0.0001,-0.0001,-0.0001,-0.0001,0.$

The planform geometry of the wing, shown in Figure 70 [16], is defined using the namelist WGPLNF.

146
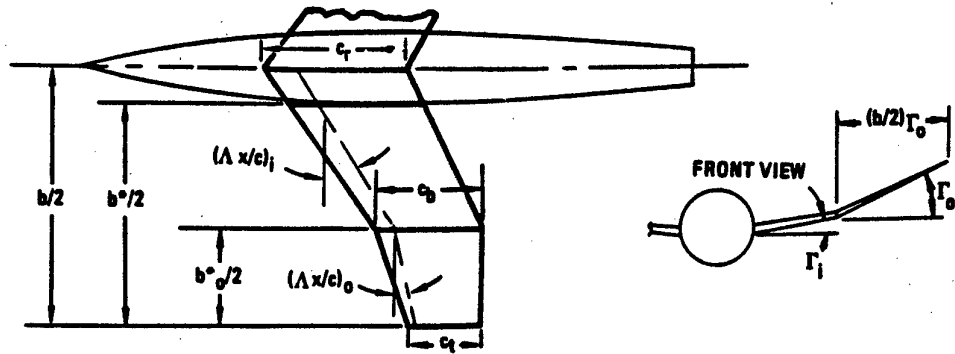
Figure 70. Parameters in namelist WGPLNF [16]

Table 23. Namelist WGPLNF

SYMBOL	VARIABLE	DEFINITION	UNIT	VALUE
c_t	CHRDTP	Tip chord	L	0.385
b*/2	SSPNE	Semi-span exposed panel	L	0.963
b/2	SSPN	Semi-span theoretical panel from theoretical root chord	L	1.023
c_r	CHRDR	Root chord	L	0.385
$(\Lambda_{x/c})_i$	SAVSI	Inboard panel sweep angle	DEG	0
x/c	CHSTAT	Reference chord station for inboard and outboard panel sweep angles, fraction of chord	-	0.25
Θ	TWISTA	Twist angle, negative leading edge rotated down (from exposed root to tip)	DEG	0
Γ_i	DHDADI	Dihedral angle of inboard panel	DEG	2.53
	TYPE	=1.0 straight tapered planform =2.0 double delta planform (aspect ratio ≤3) =3.0 cranked planform (aspect ratio >3)	-	1.0

Hence, the namelist WGPLNF generated for the Super Frontier Senior RC airplane is;

$WGPLNF CHRDTP=0.385,SSPNE=0.963,SSPN=1.023,CHRDR=0.385,
  SAVSI=0.,CHSTAT=0.25,TWISTA=0.,DHDADI=2.53,TYPE=1.$

The planform geometry of the horizontal tail, shown in Figure 71 [16], is defined using the namelist HTPLNF.
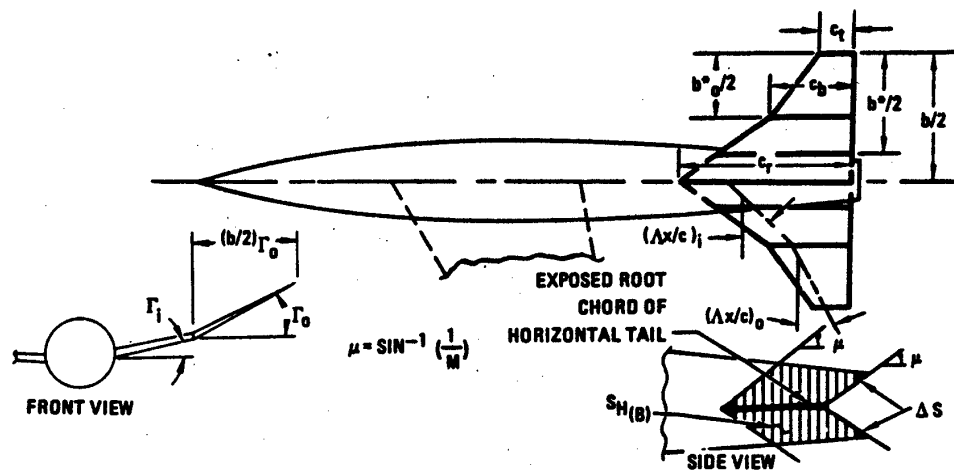
Figure 71. Parameters in namelist HTPLNF [16]

Table 24. Namelist HTPLNF

SYMBOL	VARIABLE	DEFINITION	UNIT	VALUE
c_t	CHRDTP	Tip chord	L	0.2
b*/2	SSPNE	Semi-span exposed panel	L	0.375*
b/2	SSPN	Semi-span theoretical panel from theoretical root chord	L	0.375
c_r	CHRDR	Root chord	L	0.325
$(\Lambda_{x/c})_i$	SAVSI	Inboard panel sweep angle	DEG	18.43

Table 24. Namelist HTPLNF (continued)

SYMBOL	VARIABLE	DEFINITION	UNIT	VALUE
x/c	CHSTAT	Reference chord station for inboard and outboard panel sweep angles, fraction of chord	-	0
Θ	TWISTA	Twist angle, negative leading edge rotated down (from exposed root to tip)	DEG	0
Γ_i	DHDADI	Dihedral angle of inboard panel	DEG	0
	TYPE	=1.0 straight tapered planform =2.0 double delta planform (aspect ratio $\leq$ 3) =3.0 cranked planform (aspect ratio > 3)	-	1.0

Hence, the namelist HTPLNF generated for the Super Frontier Senior RC airplane is;

$HTPLNF CHRDTP=0.2,SSPNE=0.375,SSPN=0.375,CHRDR=0.325,
 SAVSI=18.43,CHSTAT=0.,TWISTA=0.,DHDADI=0.,TYPE=1.$

The section aerodynamic characteristics of the horizontal tail, shown in Figure 69 [16], are defined using the namelist HTSCHR.

Table 25. Namelist HTSCHR

SYMBOL	VARIABLE	DEFINITION
	TYPEIN	Type of airfoil section coordinates input for airfoil section module =1.0 upper and lower surface coordinates =2.0 mean line and thickness distribution

Table 25. Namelist HTSCHR (continued)

SYMBOL	VARIABLE	DEFINITION
	NPTS	Number of section points input, maximum of 50
X_c/c	XCORD	Abscissas of input points, TYPEIN=1.0 or 2.0, XCORD(1)=0.0 and XCORD(NPTS)=1.0
Y_m/c	MEAN	Ordinates of mean line, TYPEIN=2.0 Fraction of chord, and requires MEAN(1)=0.0 MEAN(NPTS)=0.0
t_c/c	THICK	Thickness distribution, TYPEIN=2.0 Fraction of chord, and requires THICK(1)=0.0 THICK(NPTS)=0.0

Hence, the namelist HTSCHR generated for the Super Frontier Senior RC airplane is;

$HTSCHR TYPEIN=2.,NPTS=6.,XCORD(1)=0.,0.2,0.4,0.6,0.8,1.,
  MEAN(1)=0.,0.,0.,0.,0.,0.,THICK(1)=0.,0.04,0.04,0.04,0.04,0.$

The planform geometry of the vertical tail, shown in Figure 72 [16], is defined using the namelist VTPLNF.
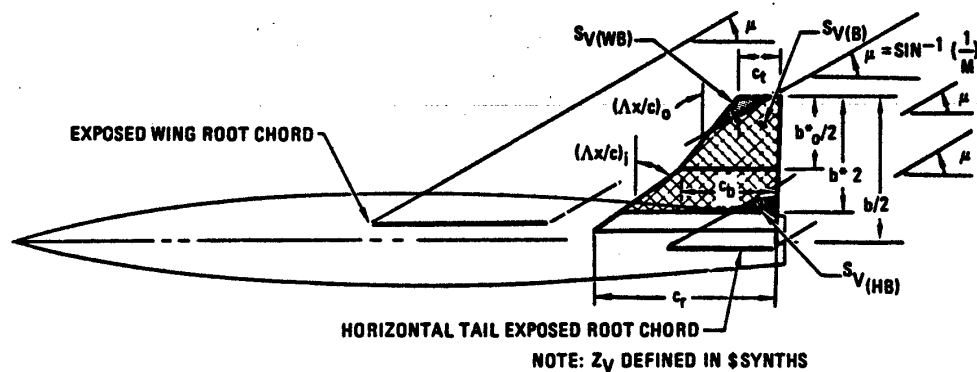
Figure 72. Parameters in namelist VTPLNF [16]

Table 26. Namelist VTPLNF

SYMBOL	VARIABLE	DEFINITION	UNIT	VALUE
c_t	CHRDTP	Tip chord	L	0.15
b*/2	SSPNE	Semi-span exposed panel	L	0.27
b/2	SSPN	Semi-span theoretical panel from theoretical root chord	L	0.29
c_r	CHRDR	Root chord	L	0.35
$(\Lambda_{x/c})_i$	SAVSI	Inboard panel sweep angle	DEG	36.53
x/c	CHSTAT	Reference chord station for inboard and outboard panel sweep angles, fraction of chord	-	0
	TYPE	=1.0 straight tapered planform =2.0 double delta planform (aspect ratio ≤ 3) =3.0 cranked planform (aspect ratio > 3)	-	1.0

Hence, the namelist VTPLNF generated for the Super Frontier Senior RC airplane is;

$VTPLNF CHRDTP=0.15,SSPNE=0.27,SSPN=0.29,
  CHRDR=0.35,SAVSI=36.53,CHSTAT=0.,TYPE=1.$

The section aerodynamic characteristics of the vertical tail, shown in Figure 69 [16], are defined using the namelist VTSCHR.

Table 27. Namelist VTSCHR

SYMBOL	VARIABLE	DEFINITION
	TYPEIN	Type of airfoil section coordinates input for airfoil section module =1.0 upper and lower surface coordinates =2.0 mean line and thickness distribution

Table 27. Namelist VTSCHR (continued)

SYMBOL	VARIABLE	DEFINITION
	NPTS	Number of section points input, maximum of 50
X_c/c	XCORD	Abscissas of input points, TYPEIN=1.0 or 2.0, XCORD(1)=0.0 and XCORD(NPTS)=1.0 required
Y_m/c	MEAN	Ordinates of mean line, TYPEIN=2.0 Fraction of chord, and requires MEAN(1)=0.0 MEAN(NPTS)=0.0
t_c/c	THICK	Thickness distribution, TYPEIN=2.0 Fraction of chord, and requires THICK(1)=0.0 THICK(NPTS)=0.0

Hence, the namelist VTSCHR generated for the Super Frontier Senior RC airplane is;

$VTSCHR TYPEIN=2.,NPTS=6.,XCORD(1)=0.,0.2,0.4,0.6,0.8,1.,
  MEAN(1)=0.,0.,0.,0.,0.,0.,THICK(1)=0.,0.04,0.04,0.04,0.04,0.$

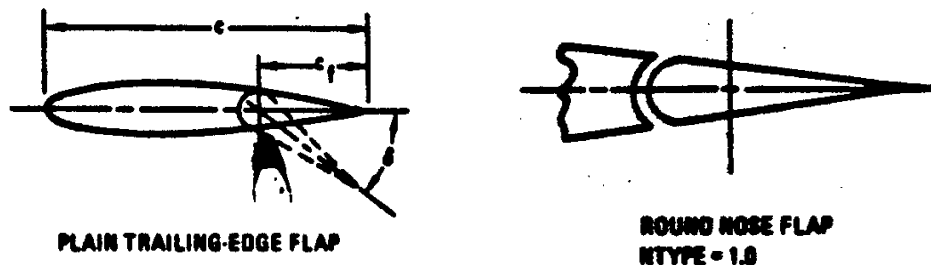The horizontal control surface (elevator), shown in Figure 73 [16], is defined using the namelist SYMFLP.

PLAIN TRAILING-EDGE FLAP

ROUND NOSE FLAP
NTYPE = 1.0

Figure 73. Parameters in namelist SYMFLP [16]

Table 28. Namelist SYMFLP

SYMBOL	VARIABLE	DEFINITION	UNIT	VALUE
-	FTYPE	=1.0 plain flaps =2.0 single slotted flaps =3.0 fowler flaps =4.0 double slotted flaps =5.0 split flaps =6.0 leading edge flaps =7.0 leading edge slats =8.0 Krueger	-	1.0
-	NDELTA	Number of flap or slat deflection angles, maximum of 9	-	9
δ_f	DELTA	Flap deflection angle measured steamwise	DEG	
$\tan(\emptyset_{TE}/2)$	PHETE	Tangent of airfoil trailing edge angle based on ordinates at 90 and 99 percent chord	-	0.0
$\tan(\emptyset_{TE}/2)$	PHETEP	Tangent of airfoil trailing edge angle based on ordinates at 95 and 99 percent chord	-	0.0
$C_{f,i}$	CHRDFI	Flap chord at inboard end of flap, measured parallel to longitudinal axis	L	0.08
$C_{f,o}$	CHRDFO	Flap chord at outboard end of flap, measured parallel to longitudinal axis	L	0.08
b_i	SPANFI	Span location of inboard end of flap, measured perpendicular to vertical plane of symmetry	L	0.0
b_o	SPANFO	Span location of outboard end of flap, measured perpendicular to vertical plane of symmetry		0.375
c_b	CB	Average chord of the balance	L	0.003
t_c	TC	Average thickness of the control at hinge line	L	0.009
-	NTYPE	=1.0 round nose flap =2.0 elliptic nose flap =3.0 sharp nose flap	-	1.0

153

Hence, the namelist SYMFLP generated for the Super Frontier Senior RC airplane is;

$SYMFLP FTYPE=1.,NDELTA=9.,DELTA(1)=-30.,-22.5,-15.,-7.5,0.,7.5,
15.,22.5,30.,PHETE=0.,PHETEP=0.,CHRDFI=0.08,CHRDFO=0.08,
SPANFI=0.,SPANFO=0.375,CB=0.003,TC=0.009,NTYPE=1.$

Propeller power effects, shown in Figure 74 [16], are defined using the namelist PROPWR.
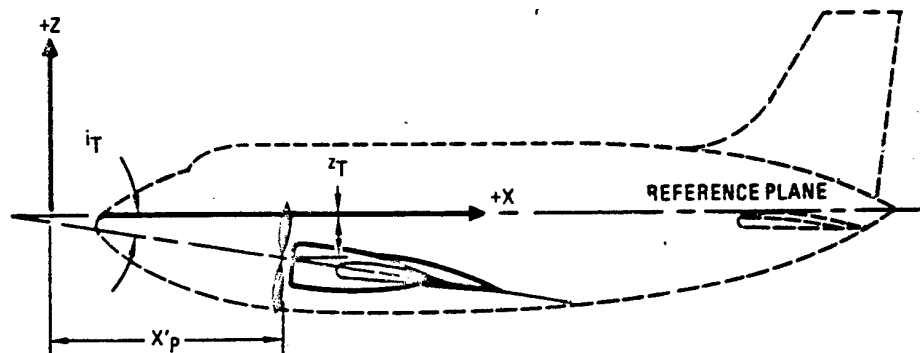
Figure 74. Parameters in namelist PROPWR [16]

Table 29. Namelist PROPWR

SYMBOL	VARIABLE	DEFINITION	UNIT	VALUE
i_T	AIETLP	Angle of incidence of engine thrust axis	DEG	0
n	NENGSP	Number of engines (1 or 2)	-	1
t_c	THSTCP	Thrust coefficient	-	0.213
x'_p	PHALOC	Axial location of propeller hub	L	0.03
Z_T	PHVLOC	Vertical location of propeller hub	L	0
R_p	PRPRAD	Propeller radius	L	0.22

154

Table 29. Namelist PROPWR (continued)

SYMBOL	VARIABLE	DEFINITION	UNIT	VALUE
$(b_p)_{0.3Rp}$	BWAPR3	Blade width at 0.3 propeller radius	L	0.03
$(b_p)_{0.6Rp}$	BWAPR6	Blade width at 0.6 propeller radius	L	0.033
$(b_p)_{0.9Rp}$	BWAPR9	Blade width at 0.9 propeller radius	L	0.021
N_B	NOPBPE	Number of propeller blades per engine	-	2
$(\beta)_{0.75Rp}$	BAPR75	Blade angle at 0.75 propeller radius	DEG	27
Y_p	YP	Lateral location of engine	L	0
	CROT	.TRUE. counter rotating propeller .FALSE. noncounter rotating propeller	-	.FALSE.

Hence, the namelist PROPWR generated for the Super Frontier Senior RC airplane is;

$PROPWR AIETLP=0.,NENGSP=1.,THSTCP=0.213,PHALOC=0.03,
 PHVLOC=0.,PRPRAD=0.22,BWAPR3=0.03,BWAPR6=0.033,
 BWAPR9=0.021,NOPBPE=2.,BAPR75=27.,YP=0.,CROT=.FALSE.$

Assembling all the namelists, the input file (for005.dat) for USAF DIGITAL DATCOM is given below.

CASEID APPROXIMATE VISTA F-16D
DIM M
 $FLTCON NMACH=5.,MACH(1)=0.04,0.05,0.06,0.07,0.08,NALPHA=20.,
 ALSCHD(1)=-20.,-15.,-10.,-8.,-6.,-4.,-3.,-2.,-1.,0.,1.,2.,3.,4.,6.,8.,10.,
 12.,16.,20.,NALT=5.,ALT(1)=1200.,1200.,1200.,1200.,1200.$
 $OPTINS SREF=0.7877,CBARR=0.385,BLREF=2.046$

$SYNTHS XCG=0.4,ZCG=0.,XW=0.35,ZW=0.1,ALIW=0.,XH=1.28,
  ZH=0.022,ALIH=0.,XV=1.16,ZV=0.032$
$BODY NX=9.,
  X(1)=0.0,0.15,0.24,0.3,0.355,0.736,0.888,1.166,1.515,
  R(1)=0.0,0.076,0.079,0.095,0.109,0.101,0.088,0.061,0.027,
  ZU(1)=0.,0.044,0.048,0.095,0.12,0.103,0.084,0.049,0.021,
  ZL(1)=0.,-0.087,-0.092,-0.095,-0.098,-0.09,-0.079,-0.059,-0.028$
$WGPLNF CHRDTP=0.385,SSPNE=0.963,SSPN=1.023,CHRDR=0.385,
  SAVSI=0.,CHSTAT=0.25,TWISTA=0.,DHDADI=2.53,TYPE=1.$
$WGSCHR TYPEIN=1.,NPTS=14.,
  XCORD(1)=0.,0.0571,0.10909,0.2447916,0.34545,0.441558,0.584415,
  0.6961,0.766233,0.8,0.9,0.95,.975,1.,
  YUPPER(1)=0.,0.0883,0.104,0.122,0.117,0.096,0.078,0.065,0.057,
  0.03,0.016,0.0068,0.,
  YLOWER(1)=0.,-0.0001,-0.0001,-0.0001,-0.0001,-0.0001,-0.0001,
  -0.0001,-0.0001,-0.0001,-0.0001,-0.0001,0.$
$HTPLNF CHRDTP=0.2,SSPNE=0.375,SSPN=0.375,CHRDR=0.325,
  SAVSI=18.43,CHSTAT=0.,TWISTA=0.,DHDADI=0.,TYPE=1.$
$HTSCHR TYPEIN=2.,NPTS=6.,
  XCORD(1)=0.,0.2,0.4,0.6,0.8,1.,
  MEAN(1)=0.,0.,0.,0.,0.,0.,
  THICK(1)=0.,0.04,0.04,0.04,0.04,0.$
$VTPLNF CHRDTP=0.15,SSPNE=0.27,SSPN=0.29,CHRDR=0.35,
  SAVSI=36.53, CHSTAT=0.,TYPE=1.$
$VTSCHR TYPEIN=2.,NPTS=6.,
  XCORD(1)=0.,0.2,0.4,0.6,0.8,1.,
  MEAN(1)=0.,0.,0.,0.,0.,0.,
  THICK(1)=0.,0.04,0.04,0.04,0.04,0.$
$SYMFLP FTYPE=1.,NDELTA=9.,DELTA(1)=-30.,-22.5,-15.,-7.5,0.,7.5,
  15.,22.5,30.,PHETE=0.,PHETEP=0.,CHRDFI=0.08,CHRDFO=0.08,
  SPANFI=0.,SPANFO=0.375,CB=0.003,TC=0.009,NTYPE=1.$

```
$PROPWR AIETLP=0.,NENGSP=1.,THSTCP=0.213,PHALOC=0.03,
  PHVLOC=0.,PRPRAD=0.22,BWAPR3=0.03,BWAPR6=0.033,
  BWAPR9=0.021,NOPBPE=2.,BAPR75=27.,YP=0.,CROT=.FALSE.$
DAMP
NEXT CASE
```

APPENDIX C

CESSNA 182 AIRPLANE CHARACTERISTICS

Roskam [8] presented geometric, mass, and flight condition data of several airplanes along with their stability and control derivatives. One of these airplanes is the Cessna 182 which is a small, single piston engine, general aviation airplane, and it has the most similar geometry with the airframe used in this study. Intuitively, the characteristics of the RC airplane and the Cessna 182 should be similar to some extent. Hence, the transfer function between the elevator deflection and the altitude of a Cessna 182 airplane, poles and zeros of this transfer function, and its root locus diagram are presented in this Appendix to better understand the stability characteristics of the RC airplane used in this study.
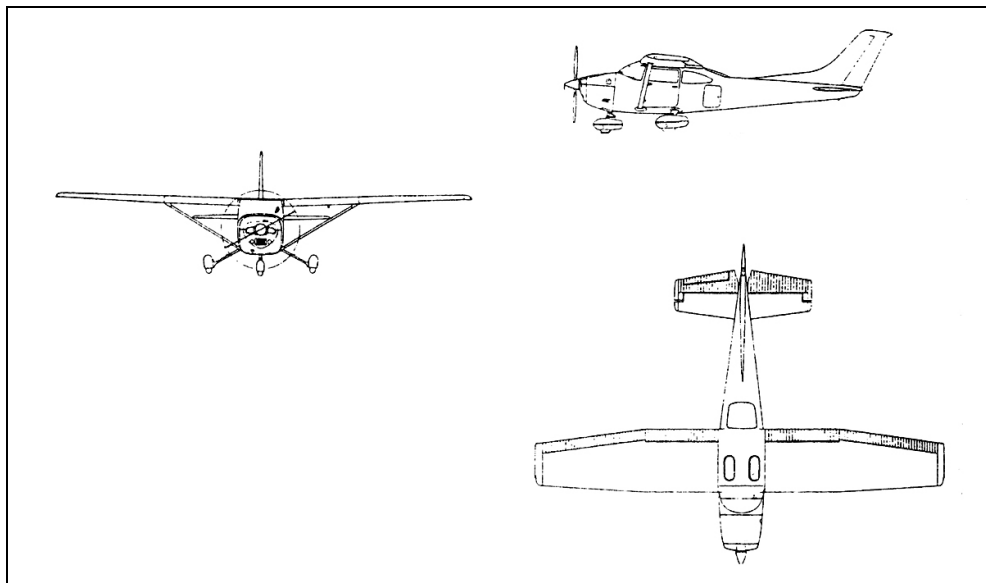

Figure 75. Cessna 182 views [8]

The transcription is between the elevator deflection and the altitude of a Cessna 182 airplane at a cruising velocity of 67 m/s and at an altitude of 1500 m is [8];

$$\frac{h(s)}{\delta_e(s)} = \frac{9878s^3 + 17908s^2 - 3402080s - 126280}{s(222s^4 + 1986s^3 + 6262s^2 + 330s + 181)}$$
(C.1)

or in normalized form

$$\frac{h(s)}{\delta_e(s)} = \frac{44.5(s^3 + 1.8s^2 - 344s - 12.8)}{s(s^4 + 8.9s^3 + 28.2s^2 + 1.5s + 0.8)}$$

$$= \frac{-698(-0.08s^3 - 0.14s^2 + 27s + 1)}{s(1.2s^4 + 11s^3 + 35s^2 + 1.8s + 1)}$$
(C.2)

The open-loop poles, zeros, and gains of the system as well as the damping ratios and undamped natural frequencies are given in Table 30.

Table 30. Plant properties of the Cessna 182 airplane

Gain	44.5
Velocity Error Coefficient, K_v(m/rad.s)	-698
Poles	0 -4.43 ± 2.86j -0.02 ± 0.17j
Damping Ratios	0.84 0.132
Undamped Natural Frequencies (rad/s)	5.27 0.17
Zeros	17.7 -19.4 -0.04

In order to explore the behavior of the closed loop altitude hold mode autopilot system of Cessna 182 with a Proportional Controller of gain K, its root locus plot drawn in MATLAB® is given in Figure 76. This root locus reveals that the system is stable for low K values and it becomes unstable after a certain K value.

The conditions on K for the system to be stable are determined with the SISO Design Tool of MATLAB® Simulink®. The analysis results showed that, K should be in the range 0<K<0.00036 rad/m for stability.

Reviewing the plant properties and root loci of the RC airplane presented in Chapter 4, it is possible to comment that it has similar stability characteristics with the Cessna 182 as it is expected.

Figure 76. Root locus of the altitude hold mode autopilot for Cessna 182